THE HIGH-FIELD GALVANOMAGNETIC PROPERTIES OF $AuAl_2$, $AuGa_2$, and $AuIn_2$

Thesis for the Degree of Ph. D.

MICHIGAN STATE UNIVERSITY

JOSEPH T. LONGO

1968

This is to certify that the

thesis entitled

THE HIGH-FIELD GALVANOMAGNETIC PROPERTIES OF $AuAl_2$, $AuGa_2$, and $AuIn_2$

presented by

Joseph T. Longo

has been accepted towards fulfillment of the requirements for

Ph.D. degree in physics

Major professor

Date Sept. 9, 1968

O-169

ABSTRACT

THE HIGH-FIELD GALVANOMAGNETIC PROPERTIES OF $AuAl_2$, $AuGa_2$, and $AuIn_2$

By

Joseph T. Longo

The Fermi surface topologies of AuX_2 (X = Al, Ga, In) are investigated using high-field galvanomagnetic measurements. The high-field galvanomagnetic properties of the nearly-free-electron (NFE) model of the Fermi surface of AuX_2 are also determined with the aid of the Harrison construction. The most important result is that the "open" fourth zone electron sheet has hole orbits for $\underline{B} \parallel \langle 111 \rangle$ in $AuAl_2$ and $AuGa_2$ in disagreement with the NFE model. New models are proposed for $AuAl_2$ and $AuGa_2$ which are in good agreement with experiment. Incomplete results for $AuIn_2$ indicate that its Fermi surface may be similar to that of $AuGa_2$.

THE HIGH-FIELD GALVANOMAGNETIC PROPERTIES OF $AuAl_2$, $AuGa_2$, and $AuIn_2$

By

Joseph T. Longo

A THESIS

Submitted to
Michigan State University
in partial fulfillment of the requirements
for the degree of

DOCTOR OF PHILOSOPHY

Department of Physics

1968

ACKNOWLEDGEMENTS

I wish to thank Professor Peter A. Schroeder for his advice, assistance, and encouragement during the course of this research. I am indebted to Professors P. A. Schroeder and F. J. Blatt for the support necessary for the completion of this work.

I am grateful to Professor D. J. Sellmyer of the Massachusetts Institute of Technology for the provision of his apparatus during runs at the Francis Bitter National Magnet Laboratory and for many informative discussions about interpretation of results. I sincerely appreciate the assistance I received from Andrew Davidson during these runs.

I am indebted to my wife, Marge, and Dr. Gordon J. Edwards for their constructive criticism of the rough draft of this thesis.

Financial support by the National Science Foundation is gratefully acknowledged.

TABLE OF CONTENTS

LIST OF TABLES

LIST OF FIGURES

Page

1. Introduction

The determination of a metal's high-field galvanomagnetic properties has played an important and well documented role in the understanding of its Fermi surface topology[1]. Until recently[2,3,4,5,6] measurements have been performed only on very pure metallic elements at liquid helium temperatures so that <u>all</u> carriers perform many cyclotron orbits before being scattered. This high-field condition, $\omega_c\tau >> 1$ for all carriers, is so rigorous that a metal crystal in a field of 20 kG must typically have an impurity content of less than 10 parts per million to satisfy it. With the advent of zone refining techniques[7], single crystals of non-transition elements meeting this requirement became available in the late 50's and were the object of extensive galvanomagnetic measurements. More recently, electron beam zone refining methods applied to the high melting point transition metals have been successful in increasing their relaxation time sufficiently to attain the high-field region in the laboratory[8,9], though the rare earth and transuranic elements are still only available with 39's purity and escape investigation.

From the above discussion it follows immediately that the high-field condition cannot be satisfied in disordered alloys. Consider a .1% concentration of element X in host

element Y; this is a 39's element Y and requires the use of a megagauss magnetic field. More concentrated alloys than this have been studied by the de Haas-van Alphen (dHvA) effect and by the use of magnetothermal oscillations. These methods have the less restrictive requirement that $\omega_c \tau >> 1$ for only a subset of all the carriers. This subset may be, e.g., the electron needles in zinc for which $m_c = .01\ m_e$[10], thus increasing ω_c accordingly over its value for free electrons. Dilute alloys of up to 1% impurity concentration are, in fact, now being extensively investigated[11] because one expects large relative changes in small low effective mass pieces of the Fermi surface upon adding an impurity of valence different from that of the host.

There is one class of metals, viz., metallic intermetallic compounds, which could in principle satisfy the high field condition. Consider a compound A_xB_y in which x and y are integers and the A and B types of atoms each have a unique set of basis vectors in the unit cell. In such a compound, the potential would be perfectly periodic and the relaxation time, τ, would approach ∞ as the temperature approached zero.

Thorsen and Berlincourt were the first to observe the dHvA effect in a metallic compound, InBi, in 1961[12]. Since then, Pearson and co-workers at the National Research

Council (NRC) in Ottawa, Canada, have observed dHvA oscillations in several binary metallic compounds and completed a study of $AuAl_2$, $AuGa_2$, and $AuIn_2$[13]. The significant part of this research to someone envisioning a high field galvanomagnetic study of a metallic compound was that the residual resistance ratios, RRR = $\rho(295^oK)$ / $\rho(4.2^oK)$, of some of the samples approached 160. This is roughly equivalent to an impurity content of 60 parts per million (cf. page 59). In a field of 50 kG, one could expect that enough carriers would be in the high field region to give useful topological information. On this basis Sellmyer and Schroeder undertook a successful study of AuSn[2,3] in 1965. Later galvanomagnetic studies of metallic compounds included ZrB_2[4], ordered Cu-Zn[5], and AuX_2[6] (X = Al, Ga, In). Work is underway on AuSn[14] and $AuSb_2$[15]. Table I indicates the experimental progress to date.

The face centered cubic fluorite compounds, AuX_2 are of considerable interest, because changes in the electronic structure from one compound to the other should be explainable in terms of the differing electronic cores at the X sites. An energy band calculation has not been carried out for these compounds, but one can speculate on relative changes with the aid of the "Phillips cancellation theory"[16]. If $|\psi_k\rangle$ is the state vector of a conduction band electron, then

Table I. List of Compounds.

Compound	RRR(highest)	B(highest)	publications
AuSn	160	150 kG	2, 3, 14
ZrB_2	110	12.7 kG	4
Cu-Zn	418	150 kG	5
$AuAl_2$	550	150 kG	6
$AuGa_2$	904	150 kG	6
$AuIn_2$	75	150 kG	6
$AuSb_2$	500	150 kG	15

$$\left[\frac{p^2}{2m} + V\right] |\psi_k\rangle = E_k |\psi_k\rangle$$

where V is the periodic potential of the lattice. Orthogonalize $|\psi_k\rangle$ to the core states $|nk\rangle$ by letting

$$|\psi_k\rangle = |X_k\rangle - \sum_n |nk\rangle \langle nk|k\rangle .$$

Here $|X_k\rangle$ is some smoothly varying function which is a solution of

$$\left[\frac{p^2}{2m} + V + V_R\right] |X_k\rangle = E_K \; |X_k\rangle$$

where V_R is a non-local repulsive potential which can be shown to better cancel V as the core states become a more complete set of basis functions in which to expand $|\psi_k\rangle$. If $V + V_R \approx 0$, then $|X_k\rangle \approx e^{i\underline{k}\cdot\underline{r}}$ unless $\underline{k}$ is near a Brillouin zone boundary at which the periodic $V + V_R$ mixes plane wave states to produce an energy gap. This is the basis of the nearly free electron (NFE) or one orthoganalized plane wave (1-OPW) Fermi surface model.

Since the heavy elements have the largest number of core states, one expects that $V + V_R$ and therefore the energy gap should be a decreasing function of the row number of the periodic table. Table II, reproduced from Sellmyer's thesis[3], gives actual examples of this effect; the energy gaps separating the valence and conduction bands in semiconductors are listed. In a metal energy gaps at the Brillouin zone boundaries separate the conduction bands. These gaps should also decrease with increasing Z in a given column so that large Z elements should be more

Table II. List of semiconductors and metals. (After Sellmyer, ref. 3)

Position*	Material	Energy Gap (eV)**	Crystal Structure
(2,4)	C(diamond)	6	diamond
(3,4)	Si	1.12	diamond
(4,4)	Ge	0.75	diamond
(5,4)	Sn(grey)	0.08	diamond
(5,4)	Sn(white)	metallic	tetragonal
(6,4)	Pb	metallic	f.c.c.
(3,5)	InP	1.30	zincblende
(4,5)	InAs	0.33	zincblende
(5,5)	InSb	0.17	zincblende
(6,5)	InBi	metallic	tetragonal
(3,4)	Mg_2Si	0.77	fluorite
(4,4)	Mg_2Ge	0.55	fluorite
(5,4)	Mg_2Sn	0.25	fluorite
(6,4)	Mg_2Pb	metallic	fluorite

* Position, (i,j), means i^{th} row, j^{th} column in periodic table. For compounds, (i,j) refers only to the position of the second listed element in the compound.

** Most of the energy gaps are taken from W. D. Lawson and S. Nielson, Preparation of Single Crystals, (Butterworths Scientific Publications, London, 1958), pp. 241, 242.

NFE-like than the smaller Z elements. In the limit $V + V_R = 0$, a metal would become free-electron like (i.e. magnetic breakdown would occur with unit probability at every zone boundary). Several effects distort this simple picture. Relativistic corrections are important for elements with $Z>55$[17]. Tin can be a metal or a semiconductor depending on its crystal structure; thus structure changes in the columns of the periodic table present complications. Also, energy gaps due to spin-orbit coupling increase with Z. Finally, if there is mixing of the high-energy core and conduction band states, this formalism fails by assumption; the noble and transition metals are in this category. Understandably then, exceptions to the rule occur: Na is the most free electron like of the bcc alkalis, but Be is less NFE-like than Mg. It is difficult to compare the elements Ca and Mg because of differing crystal structures; the same is true of Al, Ga, and In. A comparison of the fluorite compounds, AuX_2, would avoid this difficulty. Since the troublesome Au atom is common to all three, it may be that distortion from NFE behavior is primarily due to Au and secondly to the core states at the X sites. We conclude that $AuAl_2$ should be the least and $AuIn_2$ the most NFE-like.

The first experimental evidence bearing on this hypothesis came from dHvA measurements[13]. The extremal cross section of necks in the third zone had the behavior predicted above; however, the "waist" areas suggested that

$AuAl_2$ was the most NFE-like and $AuIn_2$ the least. Results on the octahedron in the second zone showed the same deviation from prediction; the $AuAl_2$ extremal areas were closer to the NFE values than those of $AuIn_2$, while the existence of this surface in $AuGa_2$ had not been decisively determined. The only comparison possible for the multiply connected surface in the fourth zone was the extremal area of the <100> directed necks. $AuGa_2$ and $AuAl_2$ both had values in close agreement with the NFE model. These results, published in the early stages of a magnetoresistance study of $AuGa_2$, provided the incentive for this comparison of the Fermi surface topologies of all three compounds and the 1-OPW model through a determination of their galvanomagnetic properties.

2. Theory of High-Field Galvanomagnetism in AuX_2

Kohler realized in 1949 that high-field magnetoresistance and Hall effect data contain important information concerning the shape of the Fermi surfaces of metals [18]; but the remarkable anisotropy to be found in magnetoresistance as a function of crystal orientation, discovered in 1938 [19], remained a mystery for 18 years. Lifshitz, Azbel, and Kaganov demonstrated in 1956 that, if all carriers completed many cyclotron orbits before being scattered, the variation of the field dependence was independent of collision processes and determined solely by geometric features of the Fermi surface. [20] In 1964 Coleman, Funes, Plaskett, and Tapp (CFPT) performed the first calculation of the absolute value of the magnetoresistance in several symmetry planes for a simple open Fermi surface using a single-relaxation-time approximation. [21] Their work on the noble metals contained the assumption that the Fermi surface consisted of a sphere pierced by narrow cylinders along <111> directions. They were successful because they applied a simplified geometrical theory to this geometrically simple model.

The 1-OPW or NFE model of a Fermi surface is geometrically simple to construct when done in the manner of Harrison [22], and prompted an attempt on our part to extend the single-relaxation-time treatment to cover the more complicated NFE surfaces. In the section, we develop the

theory and calculate the magnetoresistance from a NFE-like model of AuX_2.

For readers suspicious of a constant-relaxation time treatment, we have included a table listing those galvanomagnetic properties which do not depend on this assumption in section four.

Conductivity in High Magnetic Fields

The Boltzmann transport equation describing the motion of a system of particles in phase space is:

$$\frac{\partial f}{\partial t} + \dot{\underline{r}}\cdot\nabla_r f + \dot{\underline{p}}\cdot\nabla_p f = \left(\frac{\partial f}{\partial t}\right)_{\text{coll.}} \qquad (1)$$

f is the statistical distribution function which specifies the probability of finding a particle of the system with its position and momentum in the interval between $\underline{r}$ and $\underline{r} + d\underline{r}$ in real space and between $\underline{p}$ and $\underline{p} + d\underline{p}$ in momentum space. In an isothermal metal $\nabla_r f$ may be safely set equal to zero; we wish to consider dc effects only so that $\partial f/\partial t = 0$. Finally we note that the scattering term must vanish in equilibrium when $f = f_o$, the Fermi-Dirac distribution, and return the system to equilibrium when a deviation is introduced. The simplest possible form which satisfies these requirements is

$$\left(\frac{\partial f}{\partial t}\right)_{\text{coll.}} = -\frac{f - f_o}{\tau(\epsilon)} \qquad (2)$$

and the Boltzmann equation then reduces to

$$\dot{\underline{p}}\cdot\nabla_p f = -\frac{f - f_o}{\tau(\epsilon)} \tag{3}$$

The equations of motion of an electron in a magnetic field are

$$\dot{\underline{p}} = -|e|\underline{v} \times \underline{B}\ , \quad \underline{v} = \nabla_p \epsilon \tag{4}$$

In cartesian coordinates

$$\dot{p}_x = -|e|Bv_y\ , \quad \dot{p}_y = -|e|Bv_x$$
$$\dot{p}_z = 0\ , \quad \dot{\epsilon} = \nabla_p \epsilon\cdot\dot{\underline{p}} = 0$$

if $\underline{B} \parallel \hat{z}$. The electron moves on a curve of constant energy and constant p_z which suggests a change to variables ϵ, p_z, and a third variable μ describing the motion tangent to the trajectory. We define

$$d\mu = \frac{-\ dp_t}{\underline{v} \times \hat{z}} = |e|Bdt. \tag{5}$$

Clearly, $\dot{\mu}$ divided by a mass is a cyclotron frequency.

In the presence of a small electric field in addition to the large magnetic field, we have

$$\dot{\epsilon} = \nabla_p \epsilon\cdot\dot{\underline{p}} = -|e|\underline{v}\cdot\underline{\xi}$$

$$\dot{p}_z = -|e|\xi_z \tag{6}$$
$$\dot{\mu} = \frac{1}{v_\perp}\frac{dp_t}{dt} = |e|B\left(1 - \frac{\xi t}{Bv}\right)$$

In terms of these variables, the Boltzmann equation is

$$\dot{\epsilon}\frac{\partial f}{\partial \epsilon} + \dot{p}_z\frac{\partial f}{\partial p_z} + \dot{\mu}\frac{\partial f}{\partial \mu} = -\frac{f - f_o}{\tau(\epsilon)} . \tag{7}$$

We seek solutions linear in the electric field (Ohm's law region) and thus set

$$f = f_o + |e|\tau\underline{\xi}\cdot\underline{\psi}\,\frac{\partial f_o}{\partial \epsilon} \tag{8}$$

where $\underline{\psi}$ is to be independent of $\underline{\xi}$, $\underline{\psi} = \underline{\psi}(\epsilon, p_z, \mu)$. Keeping only terms linear in $\underline{\xi}$, we have

$$-|e|\underline{v}\cdot\underline{\xi}\,\frac{\partial f_o}{\partial \epsilon} + |e|B|e|\tau\underline{\xi}\cdot\frac{\partial \psi}{\partial \mu}\frac{\partial f_o}{\partial \epsilon} = -|e|\underline{\xi}\cdot\underline{\psi}\,\frac{\partial f_o}{\partial \epsilon}$$

Note that this is equivalent to neglecting $\underline{\xi}$ in the equations for $\dot{p}_z$ and $\dot{\mu}$. Since the electric field is arbitrary,

$$\frac{\partial \psi}{\partial \mu} + \alpha\underline{\psi} = \alpha\underline{v} \; ; \; \alpha m = \frac{m}{|e|B\tau} = \frac{1}{\omega_c\tau} \tag{9}$$

The solution of this equation is

$$\underline{\psi}(\mu) = \alpha e^{-\alpha\mu}\int_{-\infty}^{\mu} e^{\alpha\mu'}\,\underline{v}(\mu')d\mu' \tag{10}$$

Because

$$\alpha e^{-\alpha\mu} \int_{-\infty}^{\mu} e^{\alpha\mu'} \, d\mu' = 1 \, ,$$

$\underline{\psi}$ is a weighted velocity average of $\underline{v}$ along the orbit for a distance of about $1/\alpha$ in the direction from which the electron has come.

The electric current density is

$$\underline{J} = - \frac{2|e|}{(2\pi\hbar)^3} \int_{B.Z.} \underline{v} \, f \, dV_p = \bar{\sigma} \cdot \underline{\xi}$$

integrated over the Fermi surface inside each partially filled Brillouin zone. The approximation $\partial f_o/\partial\epsilon = -\delta(\epsilon - \mu)$ will be excellent for low temperatures. Now $dV_p = d\epsilon d\mu dp_z$ allows us to write

$$\bar{\sigma} = \frac{2e^2\tau}{(2\pi\hbar)^3} \iint_{B.Z.} \underline{v} \, \underline{\psi} \, d\mu dp_z . \tag{11}$$

This expression can be readily evaluated for free electrons and for field directions perpendicular and parallel to the axis of a cylindrical Fermi surface.

Free Electrons - Closed Orbits

From figure 1,

$$d\mu' = - \frac{dp_t}{v_\perp} = m d\theta'$$

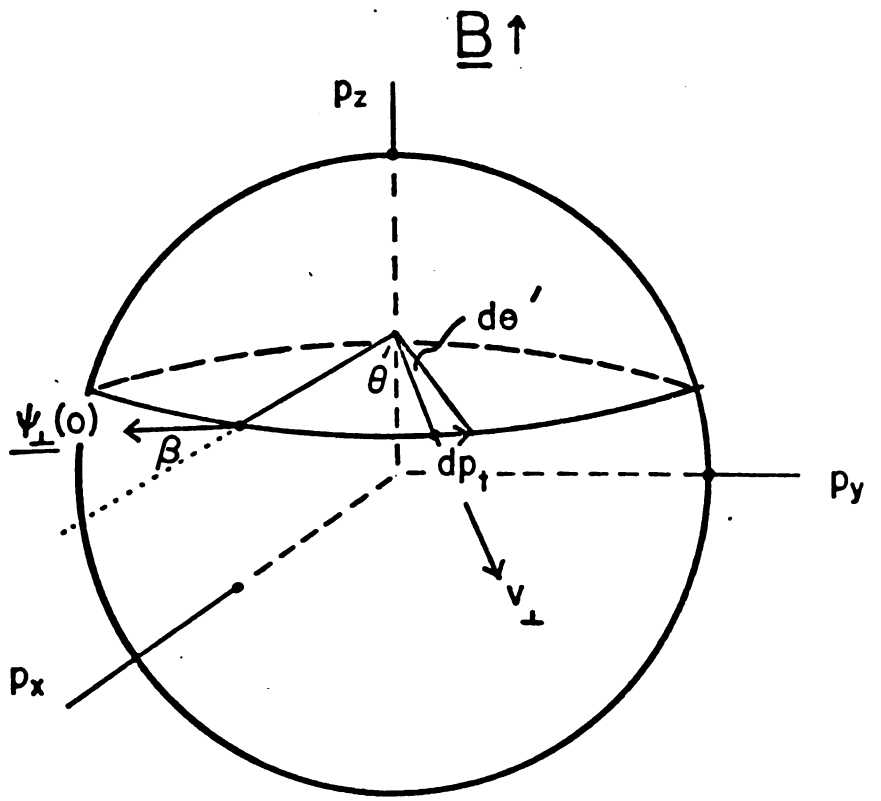

Figure 1 A spherical Fermi surface

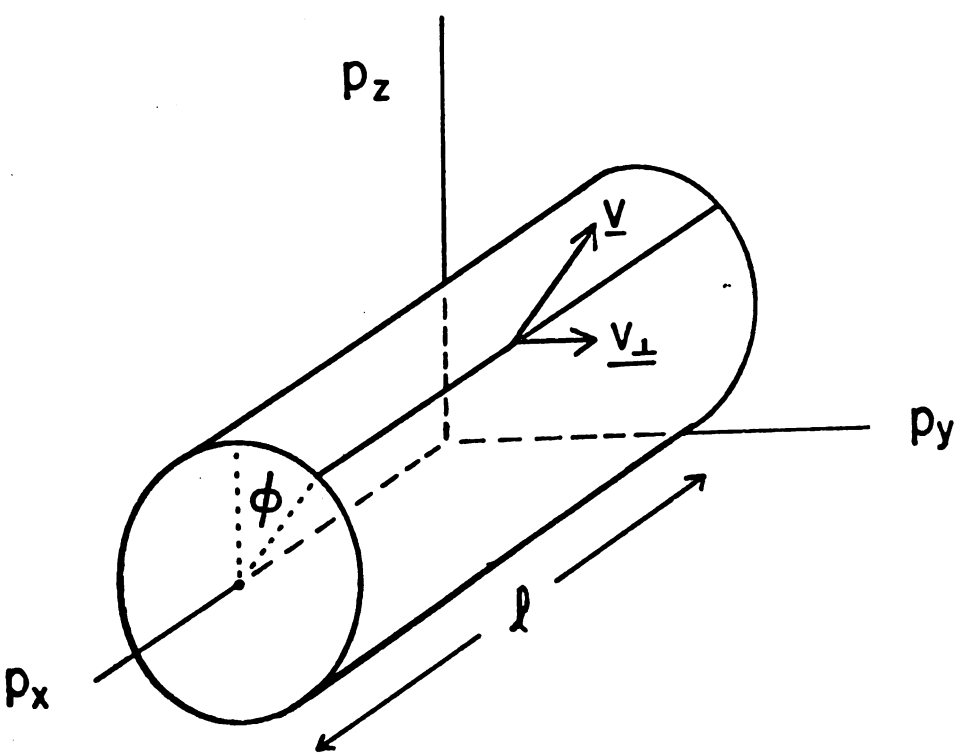

Figure 2 A cylindrical Fermi surface

$$v_x = v_\perp \cos(\mu'/m) \ , \quad v_y = v_\perp \sin\,(\mu'/m).$$

Then

$$\psi_x = v_\perp \cos\beta \cdot \cos(\mu/m - \beta)$$

from equation 10. Here $0 \le \beta \le \pi/2$ and $\cot\beta = \alpha m$. β is the Hall angle. Integrating,

$$\int_{B.Z.} v_y\ \psi_x\ d\mu = m\pi v_\perp^2 \cdot \cos\beta \cdot \sin\beta$$

$$\sigma_{yx} = (n_e e^2 \tau/\Omega m)\cos\beta \cdot \sin\beta$$

n_e is the number of electrons in a primitive cell and Ω is the cell's volume. The final result is

$$\bar{\sigma} = (n_e e^2 \tau/\Omega m)\begin{pmatrix} \cos^2\beta & -\cos\beta\ \sin\beta & 0 \\ \cos\beta\ \sin\beta & \cos^2\beta & 0 \\ 0 & 0 & 1 \end{pmatrix} \qquad (12)$$

Note that a metal with equal numbers of free electrons and free holes has vanishing off diagonal elements since $v_y = -v_\perp \sin(\mu'/m)$ for the holes. We will later prove this result for any carriers in the high field limit $\alpha m \ll 1$.

A Cylindrical Surface - Open Orbits

Consider the case of $\underline{B} \,||\, \hat{z}$ in figure 2.

$$\psi_x = 0, \quad \psi_y = v_y, \quad \psi_z = v_z.$$

from equation 10.

$$\mu_o = \ell/v_y \ , \quad p^2 = p_z{}^2 + p_y{}^2 \ ;$$

ℓ is the momentum length separating Bragg reflection planes. Then,

$$\int_0^{\mu_o} v_y \psi_y d\mu = \mu_o v_y^2 = \frac{\ell}{m} (p^2 - p_z{}^2)^{1/2},$$

$$\sigma_{yy} = \frac{n_e^o e^2 \tau}{2\Omega m} .$$

In a similar manner we obtain the other elements of the conductivity tensor.

$$\bar{\sigma} = \frac{n_e^o e^2 \tau}{2\Omega m} \begin{pmatrix} 0 & 0 & 0 \\ 0 & 1 & 0 \\ 0 & 0 & 1 \end{pmatrix} \tag{13}$$

Open and Closed Orbits

A zero'th order model of an "open" Fermi surface might consist of allotting n_h^c "free holes" to a first zone closed surface, n_e^o electrons to a second zone cylinder, and n_e^c free electrons to a third zone closed sheet. The conductivity tensor for such a model is

$$\bar{\sigma} = \frac{e^2\tau}{m\Omega}\begin{pmatrix} (n_e^c+n_h^c)\cos^2\beta & (n_h^c-n_e^c)\cos\beta\sin\beta & 0 \\ (n_e^c-n_h^c)\cos\beta\sin\beta & n_e^o/2 + (n_e^c+n_h^c)\cos^2\beta & 0 \\ 0 & 0 & n_e^c+n_h^c+n_e^o/2 \end{pmatrix} \quad (14)$$

For experimental simplicity we measure the resistivity tensor in the high-field limit, $\beta = \pi/2$. The transverse and longitudinal parts are:

$$\bar{\rho}_{tr} = \frac{m}{e^2\tau\left[n_e^o/2(n_e^c+n_h^c)+(n_e^c-n_h^c)^2\right]}\begin{pmatrix} n_e^o/2\alpha^2m^2 & (n_h^c-n_e^c)/\alpha m \\ (n_e^c-n_h^c)/\alpha m & n_e^c+n_h^c \end{pmatrix}$$

$$\rho_{zz} = \frac{m}{e^2\tau\left[n_e^c+n_h^c+n_e^o/2\right]}$$

ρ_{xz} and ρ_{yz} vanish for this model. At $\underline{B} = 0$ ($\beta=0$),

$$\bar{\rho} = \frac{m}{e^2\tau}\begin{pmatrix} 1/(n_e^c+n_h^c) & 0 & 0 \\ 0 & 1/(n_e^o/2 + n_e^c+n_h^c) & 0 \\ 0 & 0 & 1/(n_e^o/2 + n_e^c+n_h^c) \end{pmatrix}$$

The longitudinal magnetoresistance, $(\rho_{zz}(B)-\rho_{zz}(0))/\rho_{zz}(0)$, vanishes, but the transverse magnetoresistance does not:

$$\frac{\Delta\rho}{\rho} = \left[\rho_{xx}(B)-\rho_{xx}(0)\right] / \rho_{xx}(0)$$
$$= \frac{(n_e^o/2)(n_e^c+n_h^c)(\omega_c\tau)^2}{(n_e^o/2)(n_e^c+n_h^c) + (n_e^c-n_h^c)^2} - 1 > 0$$

Three possibilities are listed in Table III. The first case is realized in copper, silver, and gold with $n_h^c = 0$. CFPT's careful analysis of the noble metal topology showed that $\Delta\rho/\rho = A\xi(\omega_c\tau)^2 - 1$ for $\underline{B}$ in a symmetry plane. A is a constant which includes the number of conduction electrons, approximately n_e^c, and a measure of the cylinder area normal to $\underline{B}$. ξ measures the effective width of the cylinder area parallel to $\underline{B}$ -- the other three <111> cylinders cause some of the orbits to close back upon themselves. Nevertheless our simple model should estimate the largest $A\xi$. From CFPT one can easily calculate that the maximum $n_e^o = 1/5$. Thus the maximum $n_e^o / 2n_e^c = .125$ which is in rough agreement with their largest $A = .23$.

Cases II and III may be common occurences in metals with a large number of valence electrons per primitive cell, but the burden of calculation is now truly monumental since one cannot assume, in the manner of CFPT, that

$$\rho_{xx} \approx \frac{\sigma_{yy}(\text{open})}{\sigma_{xx}(\text{closed})\sigma_{yy}(\text{open}) - \sigma_{xy}(\text{closed})\sigma_{yx}(\text{closed})}$$

All Closed Orbits

$$\frac{\rho_{xy}}{\rho_{xx}} = \frac{\rho_{zz}}{\rho_{xy}} = \frac{n_h^c - n_e^c}{n_h^c + n_e^c} \cdot \omega_c\tau \tag{16}$$

and

$$\frac{\rho_{xx}}{\rho_{zz}} = \frac{\rho_{yy}}{\rho_{zz}} = \left(\frac{n_h^c + n_e^c}{n_h^c - n_e^c}\right)^2 \tag{17}$$

Table III. Dependence of $\Delta\rho/\rho$ on the number of electrons on open orbits.

	Case I $\frac{n_e^o}{2} \ll \frac{(n_e^c-n_h^c)^2}{n_e^c+n_h^c}$	Case II $\frac{n_e^o}{2} \approx \frac{(n_e^c-n_h^c)^2}{n_e^c+n_h^c}$	Case III $\frac{n_e^o}{2} \gg \frac{(n_e^c-n_h^c)^2}{n_e^c+n_h^c}$
$\frac{\Delta\rho}{\rho}$	$\frac{n_e^o(n_e^c+n_h^c)(\omega_c\tau)^2}{2(n_e^c-n_h^c)^2} - 1$	$\frac{(\omega_c\tau)^2}{2} - 1$	$(\omega_c\tau)^2 - 1$

allow us to make estimates of $n_e^c+n_h^c$ and $\omega_c\tau$ from the experimentally measurable ρ_{xx}, ρ_{xy}, ρ_{zz}, and $n_h^c-n_e^c$.

Real Fermi Surfaces

For a more complicated Fermi surface we can simplify $\underline{\psi}$ for closed and open periodic orbits:

$$\underline{\psi}(\mu) = \alpha e^{-\alpha\mu}\left\{ \int_{-\infty}^{0} e^{\alpha\mu'}\underline{v}(\mu')d\mu' + \int_{0}^{\mu} e^{\alpha\mu'}\underline{v}(\mu')d\mu' \right\} . \tag{18}$$

But

$$\int_{-\mu_o}^{0} e^{\alpha\mu'}\underline{v}(\mu')d\mu' + \int_{-2\mu_o}^{-\mu_o} e^{\alpha\mu'}\underline{v}(\mu')d\mu' + \ldots\ldots =$$

$$\int_{-\mu_o}^{0} e^{\alpha\mu'}\underline{v}(\mu')d\mu' + e^{-\alpha\mu_o}\int_{-\mu_o}^{0} e^{\alpha\mu'}\underline{v}(\mu')d\mu' + \ldots\ldots\ldots,$$

so that

$$\underline{\psi}(\mu) = \alpha e^{-\alpha\mu}\left\{\frac{1}{e^{\alpha\mu_o} - 1}\int_{0}^{\mu_o} e^{\alpha\mu'}\underline{v}(\mu')d\mu' + \int_{0}^{\mu} e^{\alpha\mu'}\underline{v}(\mu')d\mu'\right\}. \tag{19}$$

μ_o is the period of the orbit. In the high-field region, we can expand $\underline{\psi}$ in powers of α:

$$\underline{\psi}(\mu) = \underline{\psi}^{(0)} + \alpha\underline{\psi}^{(1)} + \alpha^2\underline{\psi}^{(2)} + \ldots\ldots\ldots\ldots \tag{20}$$

$$\underline{\psi}^{(0)} = \frac{1}{\mu_o}\int_{0}^{\mu_o} \underline{v}(\mu')d\mu' ; \tag{21}$$

$$\underline{\psi}^{(1)} = \frac{1}{\mu_o}\int_{0}^{\mu_o} \mu'\underline{v}(\mu')d\mu' - \frac{\mu}{\mu_o}\int_{0}^{\mu_o} \underline{v}(\mu')d\mu' + \int_{0}^{\mu} \underline{v}(\mu')d\mu' \tag{22}$$

$$\underline{\psi}^{(2)} = \frac{\mu^2}{2\mu_o}\int_0^{\mu_o} \underline{v}(\mu')d\mu' - \frac{\mu}{\mu_o}\int_0^{\mu_o} \mu'\underline{v}(\mu')d\mu' + \frac{1}{2\mu_o}\int_0^{\mu_o} \mu'^2\underline{v}(\mu')d\mu'$$

$$- \mu\int_0^{\mu} \underline{v}(\mu')d\mu' + \int_0^{\mu} \mu'\underline{v}(\mu')d\mu' \ . \tag{23}$$

Only $\underline{\psi}_\perp^{(0)}$ is trivial;

$$\underline{\psi}_\perp^{(0)} = \frac{1}{\mu_o}\int_0^{\mu_o} \hat{z} \times (\underline{v} \times \hat{z})\ d\mu' = (\hat{z} \times \Delta\underline{p})/\mu_o \tag{24}$$

$\Delta\underline{p}$ is the momentum change from the beginning to the end of the period.

Consider the case of all closed orbits. We use the notation $\langle\ '\rangle = \int_0^{\mu_o} d\mu'$ and $\langle\ '\rangle^{\mu} = \int_0^{\mu} d\mu'$. $i = x$ or y.

$$\psi_z^{(0)} = \langle v_z'\rangle/\mu_o$$

$$\psi_z^{(1)} = \langle\mu' v_z'\rangle/\mu_o - \mu\langle v_z'\rangle/\mu_o + \langle v_z'\rangle^{\mu}$$

$$\psi_i^{(0)} = \langle v_i'\rangle/\mu_o = 0$$

$$\psi_i^{(1)} = \langle\mu' v_i'\rangle/\mu_o + \langle v_i'\rangle^{\mu}$$

$$\psi_i^{(2)} = \mu\psi_i^{(1)} + \langle\mu'^2 v_i'\rangle/2\mu_o + \langle\mu' v_i'\rangle^{\mu}$$

To determine $\bar{\sigma}$ we must evaluate several integrals.

$$\int_0^{\mu_o} v_z\psi_z^{(0)}d\mu = \langle v_z'\rangle^2/\mu_o \tag{25}$$

$$\int_0^{\mu_o} v_i\psi_z^{(1)}d\mu = -\langle v_z'\rangle\langle\mu v_i\rangle/\mu_o + \langle v_i\langle v_z'\rangle^{\mu}\rangle \tag{26}$$

$$\int_0^{\mu_o} v_x \psi_y^{(1)} d\mu = \langle v_x \langle v_y' \rangle^{\mu} \rangle = \int_0^{\mu_o} dp_y \int_0^{\mu} -dp_x'$$

$$= -\text{Area(electrons)} + \text{Area(holes)} \tag{27}$$

$$\int_0^{\mu_o} v_i \psi_i^{(2)} d\mu = -\langle \mu v_i \rangle^2/\mu_o - \langle \mu v_i \langle v_i' \rangle^{\mu} \rangle + \langle v_i \langle \mu' v_i' \rangle^{\mu} \rangle \tag{28,29}$$

The demonstration that $\int_0^{\mu_o} v_i \psi_i^{(1)} d\mu = 0$ is unnecessary: the Onsager relations $\sigma_{kl}(B) \equiv \sigma_{lk}(-B)$ predict that diagonal elements can only be even in α and reduce the number of independent off-diagonal elements to three.

For orbits open in $\hat{x}$, the only changes are

$$\psi_y^{(0)} = \langle v_y' \rangle/\mu_o = -\Delta p_x/\mu_o$$

$$\psi_y^{(1)} = \langle \mu' v_y' \rangle/\mu_o - \mu \Delta p_x/\mu_o + \langle v_y' \rangle^{\mu}$$

Then,

$$\int_0^{\mu_o} v_z \psi_y^{(0)} d\mu = \Delta p_x \langle v_z \rangle/\mu_o \tag{30}$$

$$\int_0^{\mu_o} v_x \psi_y^{(0)} d\mu = 0$$

$$\int_0^{\mu_o} v_x \psi_y^{(1)} d\mu = -\Delta p_x \langle \mu v_x \rangle/\mu_o + \langle v_x \langle v_y' \rangle^{\mu} \rangle \tag{31}$$

$$\int_0^{\mu_o} v_y \psi_y^{(0)} d\mu = (\Delta p_x)^2/\mu_o \tag{32}$$

In the most general case, we cannot expect integrations over dp_z to cause the vanishing of any of the functions of p_z represented by these integrals. Thus the conductivity tensor has the form

$$\bar{\sigma} = \begin{pmatrix} a_{oc}\alpha^2 & a_{oc}\alpha & a_{oc}\alpha \\ a_{oc}\alpha & a_o + a_{oc}\alpha^2 & a_o + a_{oc}\alpha \\ a_{oc}\alpha & a_o + a_{oc}\alpha & a_{oc} \end{pmatrix} ; \tag{33}$$

a_o is a coefficient to be evaluated for open orbits only, a_{oc} for both open and closed orbits. Inversion of this tensor gives us the experimentally measured resistivity tensor. Normally each ρ_{ij} depends on all nine of the σ_{kl}, but for the case of no open orbits a simplification occurs:

$$\rho_{ij} = (-1)^{i+j} \text{ cofactor}(\sigma_{ij})/\text{determinant}(\bar{\sigma}) ;$$

Since $\text{determinant}(\bar{\sigma}) = O(\alpha^2) = -\sigma_{zz}\sigma_{xy}\sigma_{yx}$,

$$\bar{\rho} = \begin{pmatrix} \sim B^o & 1/\sigma_{xy} & \sim B^o \\ 1/\sigma_{yx} & \sim B^o & \sim B^o \\ \sim B^o & \sim B^o & \sim B^o \end{pmatrix}. \tag{34}$$

Of the nine elements, only ρ_{xy} and ρ_{yx} do not saturate in the high-field region. These terms have a simple form since

$$\sigma_{xy} = -\frac{2e^2\tau\alpha}{(2\pi\hbar)^3}\int_{B.Z.}\left[A_p(e) - A_p(h)\right] dp_z$$

$$-\frac{|e|(n_e - n_h)}{B\Omega} \tag{35}$$

Ω is the volume of the primitive cell, n_e and n_h are the number of occupied electron and hole states, respectively,

per primitive cell of the crystal. The prediction of $n_e - n_h$ for any metal is given by setting the "known" number of electrons in the conduction band equal to the number of states occupied in the various zones of momentum space,

$$n_V = 2F + n_e + (2J - n_h) \ . \tag{36}$$

n_V is the number of valence electrons per primitive cell in the crystal, F is the number of zones completely filled with electrons, $2J - n_h$ is the number of electrons in partially filled zones with hole surfaces. Notice that, if n_V is even, $n_e - n_h$ may vanish. This actually occurs for all even-valence non-magnetic metals whose Fermi surfaces have been investigated and leads to a completely different resistivity tensor because the determinant$(\bar{\sigma}) = O(\alpha^4)$. These "compensated" metals are primarily characterized by elements $\rho_{xx}, \rho_{yy} = O(B^2)$ in contrast to the odd-valence "uncompensated" metals.

For "singular" field directions[1] to be discussed in detail later, we must amend σ_{xy}:

$$\sigma_{xy} = \frac{-|e|(n_e - n_h \mp \Delta n)}{B\Omega} \tag{37}$$

Δn measures the number of carriers which have changed character on an open sheet. Thus a compensated metal can undergo "geometric discompensation" along certain high symmetry axes

(<0001> in Mg and Zn), or an uncompensated metal could become compensated (this is almost the case for Cu, $\underline{B}$ || <111>).

If there are open orbits on the Fermi surface, the determinant($\bar{\sigma}$) does not simplify although it is still of order α^2. The form of $\bar{\rho}$ is

$$\bar{\rho} \sim \begin{pmatrix} B^2 & B & B^o \\ B & B^o & B^o \\ B^o & B^o & B^o \end{pmatrix} \tag{38}$$

Thus ρ_{xx} goes as B^2 with a coefficient dependent in a complicated way on the shape of the orbits since

$$\rho_{xx} = \frac{\sigma_{yy}\sigma_{zz} - \sigma_{zy}\sigma_{yz}}{\left|\left[\sigma_{yy}\sigma_{zz} - \sigma_{zy}\sigma_{yz}\right]\sigma_{xx} + \sigma_{yz}\sigma_{xy}\sigma_{zx} + \sigma_{zy}\sigma_{xz}\sigma_{yx} - \sigma_{yy}\sigma_{zx}\sigma_{xz} - \sigma_{zz}\sigma_{xy}\sigma_{yx}\right|} \tag{39}$$

For certain symmetry directions, e.g. <211> and <110>, it may be possible for a surface to support two bands of non-intersecting open orbits with different average directions. In this case all the elements of ρ saturate.

Description of the NFE Model of the Fermi Surface of AuX_2

AuX_2 has the fluorite structure with the gold atoms lying on a face-centered cubic lattice and the X atoms occupying all the tetrahedral sites between the gold atoms

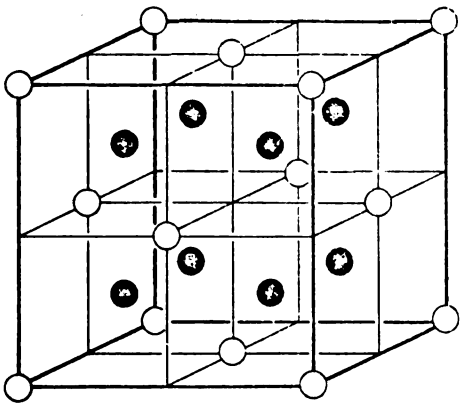

Figure 3 Crystal structure of the AuX_2 compounds. X is symbolized by the darkened spheres. (After Jan *et al.*, ref. 13)

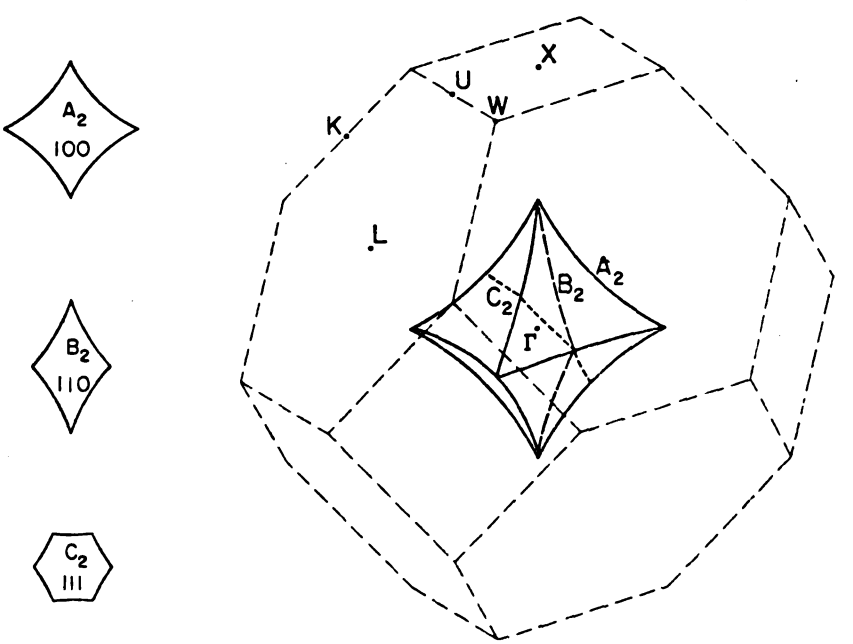

Figure 4 Holes in the second zone of the NFE model of AuX_2. (After Jan *et al.*, ref. 13)

(figure 3). This structure belongs to the space group Fm3m, so the Fermi surface will have full cubic symmetry. The NFE Fermi surface was first constructed by the NRC group[13] using the method of Harrison[22]. A free electron sphere whose volume equals the number of valence electrons times one-half the volume of each Brillouin zone is positioned about each body-centered cubic lattice point in momentum space. The occupied electronic states in the n'th zone are made up of all points located within n or more spheres. We can thus construct the Fermi surface for each zone in the repeated zone scheme without considering the placement of the zone boundaries. For our model seven nearly free electrons are assumed and one-half the volume of each Brillouin zone is $(1/2)(4)(2\pi\hbar/a)^3$. The factor 1/2 arises because each zone can accommodate two electrons per primitive cell of the real lattice; we choose $2\pi\hbar/a$ as a unit in momentum space to render the model independent of the lattice parameters which vary among the three compounds.

To facilitate a study of this surface a computer program was written which performs the Harrison construction calculations and plots the results with the aid of a 30" x-y plotter. A description of this program, which also plots Brillouin zone boundaries, is contained in Appendix A along with a program listing. The cross sections shown in figures 8-17 are from the computer plots.

The first zone is full. The surface in the second zone has the shape of an octahedron holding about .05 holes

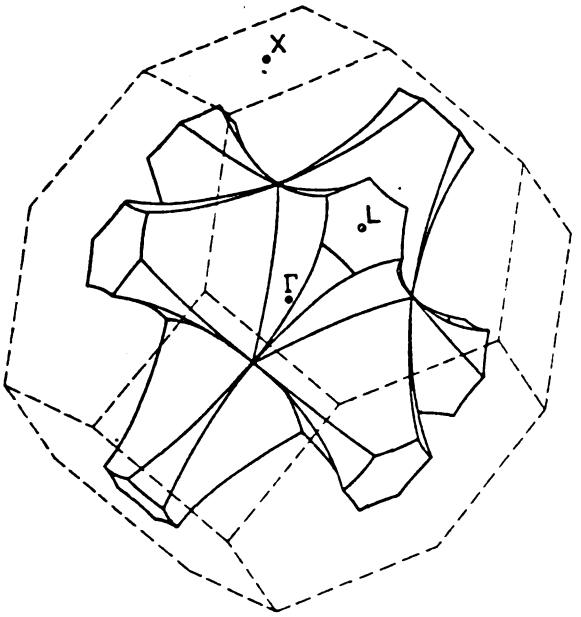

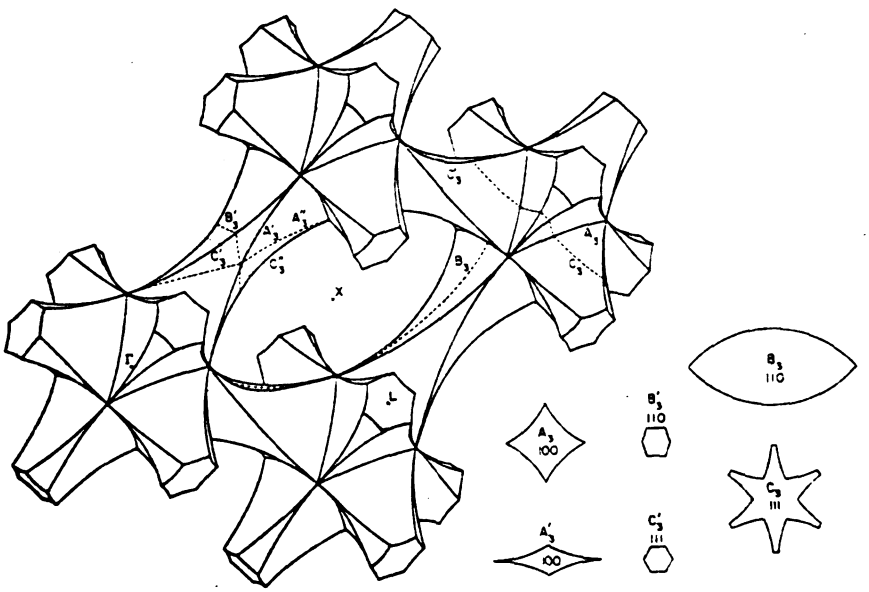

Figure 5 Holes in the third zone of the NFE model of AuX_2 in the reduced and repeated zone schemes. (After Jan *et al.*, ref. 13)

(figure 4). There is good experimental evidence concerning this surface in $AuAl_2$ and $AuIn_2$ from the dHvA experiment. The open surface in the third zone, containing .34 holes, makes contact with the hexagonal faces of the zone as do the noble metals (figure 5). dHvA data indicate that this contact area is reduced to about one-third of the NFE value in $AuGa_2$ and $AuIn_2$ and 1/15 of that value in $AuAl_2$; this will considerably reduce the width of the open orbit layers, particularly in $AuAl_2$. The open electron sheet in the fourth zone (figure 6) has "arms" along the directions <100>. dHvA evidence indicates that some of the $AuAl_2$ extremal areas on this surface have values in good agreement with NFE predictions. It holds 1.14 electrons. The surfaces in the fifth and sixth zones contain .20 and .05 electrons, respectively (figure 7). Recently experimental evidence from dHvA confirms the existence of a surface in the fifth zone. (See reference in Table XI)

The galvanomagnetic properties give no direct information on closed surfaces, but simply determine the number of full plus hole zones. A measurement of the Hall effect in AuX_2 for general field directions supporting no open orbits will give $n_e - n_h$; since closed and open surfaces contribute to n_e and n_h one suspects that all the surfaces must be considered in computing this quantity for any model. For the NFE model of AuX_2, $n_e - n_h = .05 + .20 + 1.14 - .34 - .05 = 1.0$. A close examination of equation 36 reveals, however,

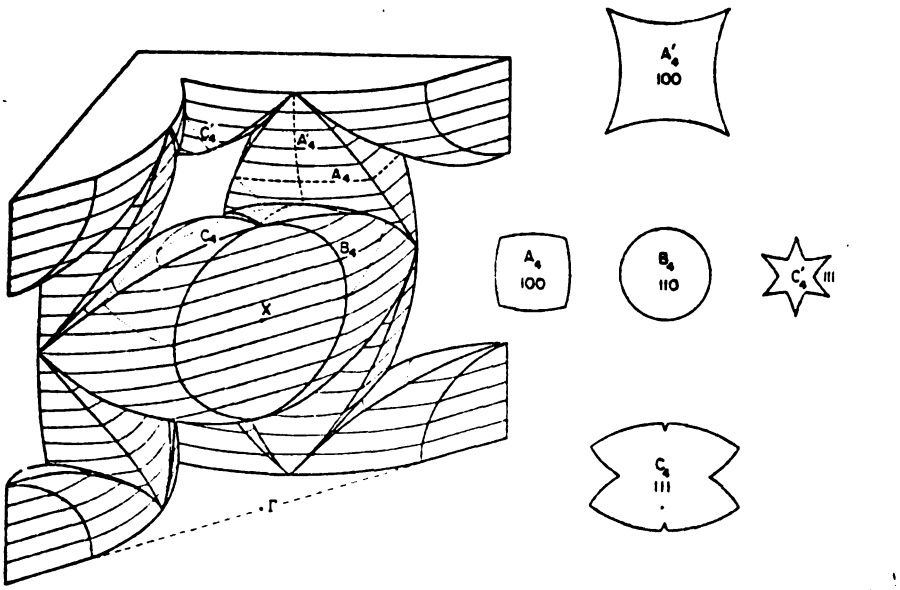

Figure 6 Section of the NFE surface in the fourth zone. (After Jan *et al.*, ref. 13)

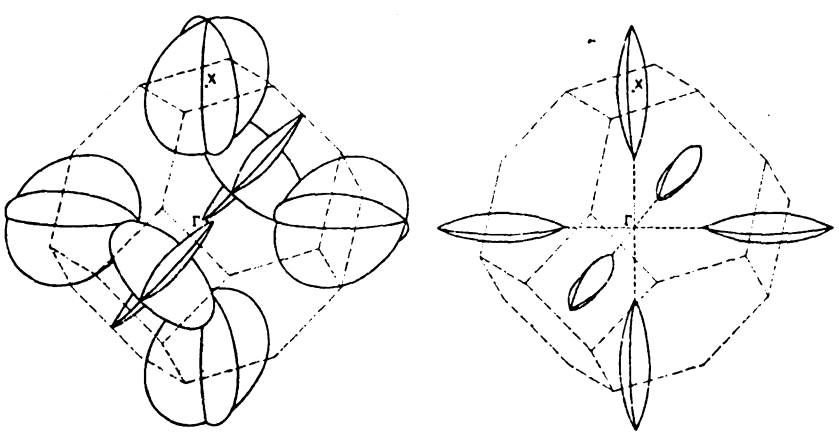

Figure 7 NFE surfaces in the fifth zone (left) and sixth zone (right). (After Jan *et al.*, ref. 13)

that any model having seven valence electrons and a combination of three full and hole zones also has $n_e - n_h = 1.0$.

In addition to the general field directions, there are two singular field directions in the NFE model, <100> and <111>. They are defined as axes of higher than two-fold symmetry which are at the center of a region of aperiodic open orbits. At the singular direction the open orbits intersect to form closed orbits of character opposite to that of the open surface. Figures 8 and 9 are cross sections of the Fermi surface for $\underline{B}$ ll <100> and <111> in the third and fourth zones. Clearly, there are closed hole orbits on the fourth zone electron sheet for $\underline{B}$ ll <100> and there are closed electron orbits on the third zone hole surface for $\underline{B}$ ll <111>. To calculate $n_e - n_h$ for $\underline{B}$ ll <100>, we must subtract from n_e those electrons which have changed character, n_e' , and add to n_h the new holes, n_h'. This is equivalent to subtracting the total volume occupied by n_e' and n_h' multiplied by $2\Omega/(2\pi\hbar)^3$; this volume is $A \cdot d$ where A is the cross-sectional area of a cell with $A \neq A(p_z)$ and d is the p_z width over which the orbits have changed character. $\Delta n = n_e' + n_h'$ is to be added to $n_e - n_h$ for electrons on a hole sheet and subtracted from it for holes on an electron surface. Then

$$\rho_{xy} = \frac{-B\Omega}{|e|\, n}\,, \quad n = n_e - n_h \mp \Delta n \tag{40}$$

The calculated values give $n_{111} = 1.035$ electrons per primitive cell and $n_{100} = 0.372$ holes per primitive cell.

Figure 8 Cross sections of the NFE surfaces in the third (clear) and fourth (shaded) zones at the p_z values given for $\underline{B}$ || <100>. Height of the unit cell = 2.0

Figure 9 Cross sections of the NFE surfaces in the third (clear) and fourth (shaded) zones at the p_z values given for $\underline{B}$ || <111>. Height of the unit cell = $(3)^{1/2}/3$ = .577 .

Figure 10 Cross section of fourth zone surface for $\underline{B}$ 29° from [100] in a (010) plane with orbits open in [010].

Figure 11 Cross section of fourth zone surface for $\underline{B}$ in {110} with orbits open in <110>.

Figure 12 Cross section of third and fourth zone surfaces for $\underline{B}$ in {111} with orbits open in <111>.

Figure 13 Cross section of fourth zone surface for $\underline{B}$ in {210} with orbits open in <210>

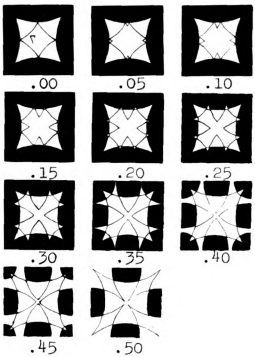

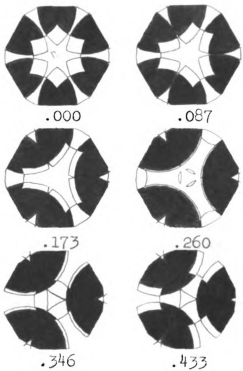

Fig. 9

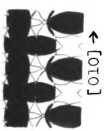

Fig. 10

Fig. 12

Fig. 11

Fig. 13

The
wal

di
be
(c
wi
su
th
o
u
c
c
r
c

These values differ significantly from the experimental values we will present later.

We now turn to the investigation of those field directions supporting open orbits. From figure 6 it can be seen that as the field is tilted away from [100] in a (010) plane, orbits which are open in the direction [010] will occur for some values of p_z on the fourth zone surface. A cross section for $\underline{B}$ 29° from [100] demonstrates this effect in figure 10. These periodically repeating orbits are called "primary" open because they make repeated use of the same [010] arm of the Fermi surface when they cross the zone boundary. Secondary periodic open orbits occur for some field directions in the (110) plane by repeated use of [100] and [010] arms to give a [110]-directed open orbit (figure 11). Fourth zone tertiary orbits open in the directions <111> and <210> have also been investigated (figures 12 and 13).

If $\underline{B}$ is applied in a direction close to the [100] axis in a non-symmetry plane (point a in figure 18), a plane perpendicular to $\underline{B}$ will intersect the Fermi surface to form alternating bands of closed electron and hole orbits which are separated by two-dimensional aperiodic open orbits as seen in figure 14. They are called two-dimensional since they are generated for a solid angle of field directions which is represented by an area on a stereogram, and they are called aperiodic since the direction cosines of $\underline{B}$ are incommensurable. As the angle between $\underline{B}$ and [100]

Figure 14 Cross section of fourth zone with B at point a in figure 18. Open orbits separated by closed electron and hole orbits, net direction is 10° from <100> in the {100} plane.

Figure 15 Cross section of fourth zone with B at point b in figure 18. Open orbits separated only by an occasional closed electron orbit; note how closed hole orbits have unfolded to form sections of open orbits or in one case pinched off the open orbit altogether; net direction is 18° from <100> in the {100} plane.

Figure 16 Cross section of fourth zone with B at point c in figure 18. Extended orbits on the fourth zone surface several degrees from the edge of the two-dimensional region.

Figure 17 Cross sections of the NFE surfaces in the third (clear) and fourth (shaded) zones at the p_z values given for B parallel to <110>.

Figure 14

Figure 15

Figure 16

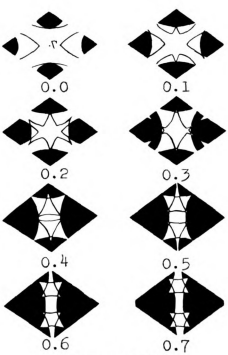

Figure 17

increases, the number of hole orbits gets progressively narrower and disappears; observe figure 15 and point b in figure 18. If the field now angles towards <111>, the number of open orbits begins to decrease, and finally all the open orbits coalesce to form closed orbits "extended" over several zones; refer to figure 16 and point c in figure 18. If the field moves toward <110> from point b, the open orbits persist even for $\underline{B}$ parallel to that axis. The cross sections for $\underline{B}$ ll <110> shown in figure 17 reveal only closed electron orbits for small values of p_z, closed hole orbits for intermediate values, and open orbits for the largest values of p_z. The presence of closed hole orbits for $\underline{B}$ ll <110> requires that <110> be surrounded by a two-dimensional region of open orbits in order that the closed hole orbits may be "unfolded" by an open orbit and then "refolded" into the electron orbits we observe for a general field direction. But the width, d, of the hole orbit layer cannot be determined on this model through the Hall voltage since the open orbits change ρ_{xy} into a very different form than it has in equation 40. For the field parallel to <211>, there are non-intersecting orbits open in directions <111> and <110>, but there are no hole orbits on the electron sheet. All of these results are summarized in figure 18a which is a stereogram of field directions. Shaded areas represent field directions giving rise to orbits open in a single direction and, therefore, to a B^2 dependence of the magnetoresistance. 115 field directions

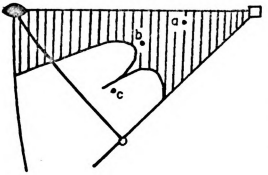

Figure 18a
Magnetoresistance stereogram for the NFE model in the fourth zone.

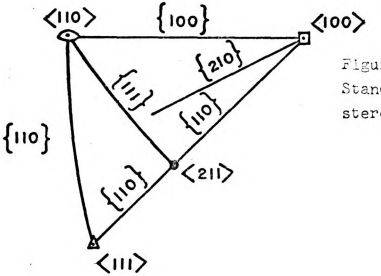

Figure 18b
Standard 100 stereogram.

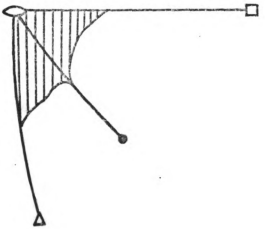

Figure 18c
Magnetoresistance stereogram for the NFE model in the third zone.

were

cone
elec
exte
thes
dis
pre
to
fig
exp
re
pe
ra
po

c
e
c
a

were sampled for open orbits by the computer.

A similar analysis has been carried out on the third zone hole surface. <111> is singular but the layer of electron orbits on the hole sheet is so narrow that the extent of the two-dimensional region is estimated at less than one degree. <100> is not singular. There is a two-dimensional region of open orbits surrounding <110> due to the presence of a layer of electron orbits when $\underline{B}$ is parallel to that direction. The complete results are summarized in figure 18c. If the necks are diminished in size, we can expect a decrease in the size of the two-dimensional regions and possibly the angular extent of the secondary periodic open orbits, <100> and <110>. The <111> primary open orbits will probably only be restricted in width parallel to B.

Lifshitz and Peschanskii have analyzed several types of Fermi surfaces which were derived from an analytic expression for $\epsilon(\underline{p})$. [23] For one surface which consisted of a three-dimensional grid of undulating cylinders whose axes are parallel to the directions <100>, <110>, and <111>, the <111> and <110> two-dimensional regions overlapped. Inside this overlap, layers of open trajectories with different average directions are formed; thus the magnetoresistance must saturate destroying the connectivity of the two-dimensional regions. These aperiodic open orbits must be intersecting rather than non-intersecting since all values of p_z will be sampled if repetition is not possible.

Bot
(ii
val
mob
si
B
su
pr
fo
A
wa
o
t
f
I
<
a

Both our NFE results (figure 18) and our experimental data (figure 35) show that their analysis is not of general validity. The reason for this is the artificiality of a model with three sets of open "arms". Such a model cannot give non-intersecting orbits in two directions for B ll <211> or <110>, a known feature of at least four Fermi surfaces[24,8] and our NFE model. Their model also cannot produce <100> directed orbits when B ll <110>, which occurs for the copper Fermi surface[25] and for our NFE model of AuX_2 also. Thus we see that their model is of limited value. Two interesting variations of their model do occur on the NFE model of AuX_2. The most obvious is the fact that the third zone has <111> directed arms while the fourth zone has <100> directed arms. The region of overlapping aperiodic open orbits is centered entirely about <110>. Our computer plots, however, indicate that the average direction of open orbits from both zones is the same. Secondly, the rather abrupt termination of the two-dimensional region about <110> as B moves away from <110> within the <110> - <111> - <211> spherical triangle is caused by the intersection of orbits open in different average directions. One set of orbits is derived from the <100> - directed orbits seen for B ll <110>; the other set arises from the unfolding of the hole orbits for B ll <110>. For B not far from this axis these orbits "constructively interfere". But with B deviating by more than 10° from <110> they "close" each other off.

abs
Per
to
pre
the
app
spl
se
ge
pr
Ho
no
Pr
(S

s
z
n
s
s
w
d

<

Calculation of $\Delta\rho/\rho$ for AuX_2 in the $\{100\}$ Plane

We have developed a theory capable of calculating the absolute value of the magnetoresistance for a complicated Fermi surface model with a single value of $\omega_c\tau$. We now wish to apply this theory to the NFE model of AuX_2 in order to predict the value of the magnetoresistance. Unfortunately, this project is, in fact, a major undertaking and we resort approximating the Fermi surfaces of zones 2,3,5, and 6 by spheres and assuming the fourth zone necks have square cross-sections. The drastic nature of these approximations suggests that calculations on this model should be considered primarily as a guide to a more exact later calculation. However, a comparison between σ_{yy} determined for the NFE model and this model was made and it indicates that the approximation may be fairly good for $\underline{B}$ less than 30° from <100> (See figure 20).

Consider figure 19. This "log-pile" surface has the same topology as the NFE Fermi surface of AuX_2 in the fourth zone. For simplicity of calculation, we have chosen the necks to have a width of 1/2 in units $2\pi\hbar/a = 1$. We consider orbits in the $\{100\}$ plane only and note that there are six types, labelled A,B,C,D,E, and H. We must calculate weighted velocity averages of these orbits and integrate over dp_z to obtain the various σ_{ij}'s.

For our model each open orbit is composed of five types of sections which we label in figure 19 as κ, κ', λ,

Figure 19 Open and closed orbits on a "log-pile" surface with the same topology as that of the fourth zone of the NFE model.

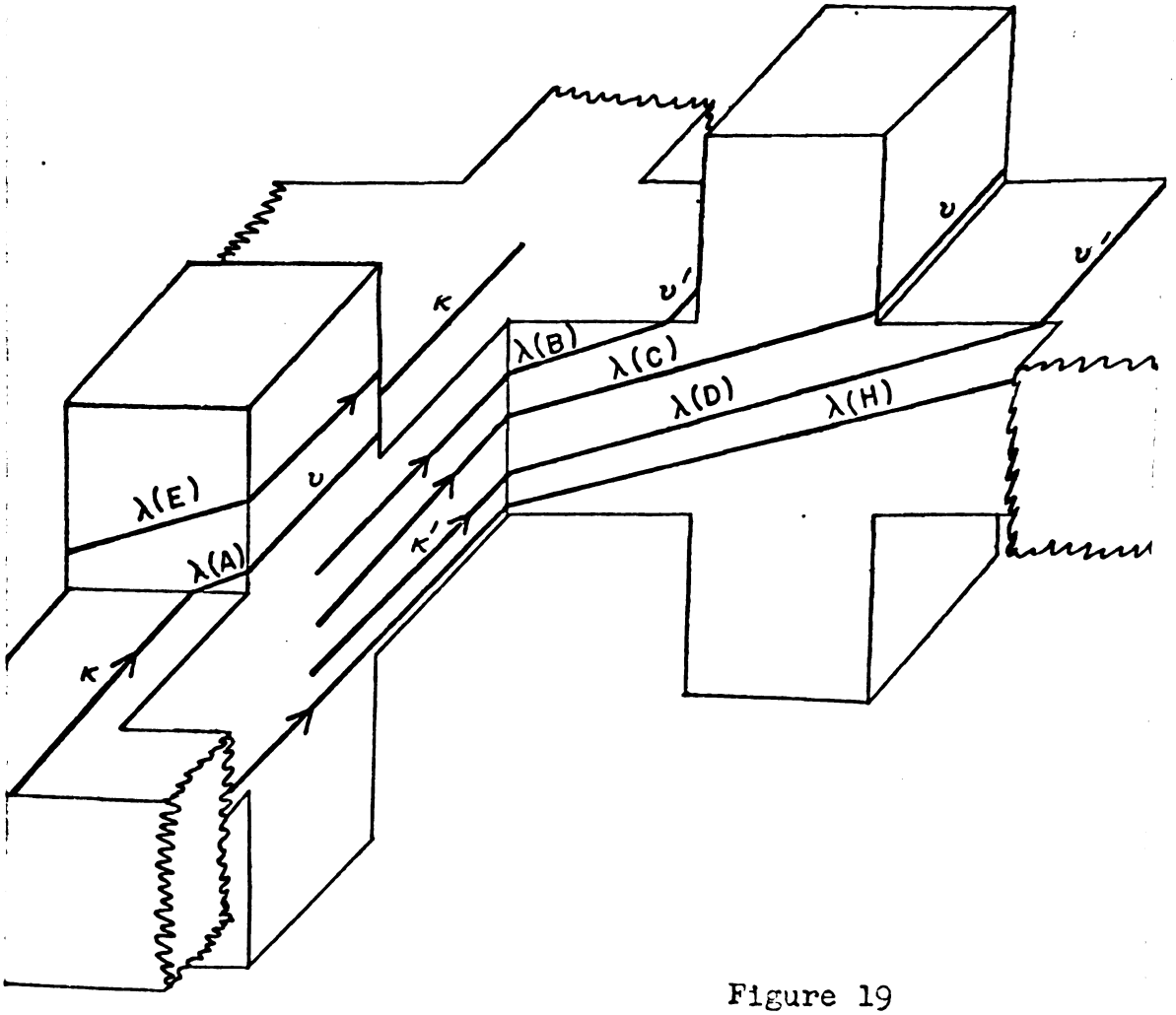

Figure 19

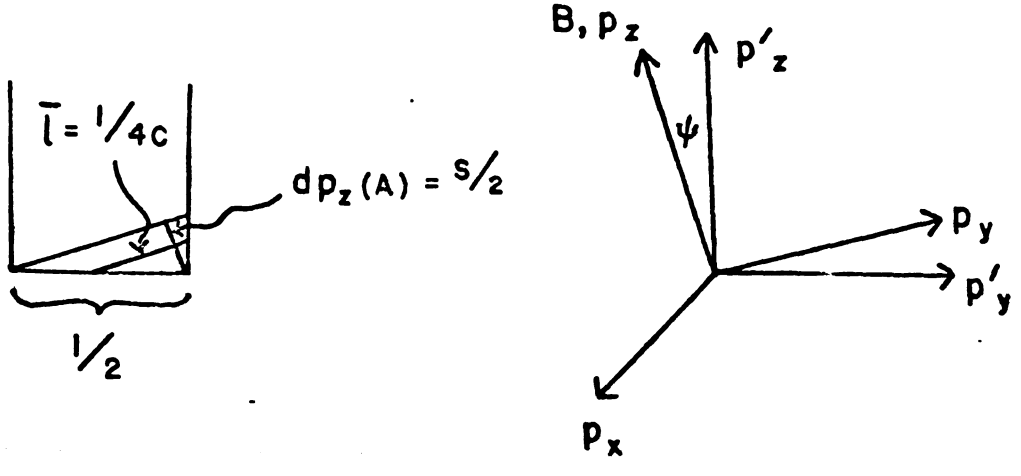

ν, and ν'. The closed electron and hole orbits are each composed of only two types. From the figure, $\kappa = -dp_t/v_\perp = -(-3/4)/v_F \sin\psi = 3/4vs = m/2s$. The Fermi velocity, $v_F = v$, is given by $\hbar k_F/m = 1.495/m \approx 3/2m$. Similarly κ' is $m/2\cos\psi = m/2c$. Also $\nu = m/3c$ and $\nu' = m/3s$. Since λ changes with angle and p_z, we leave it as $\lambda = \ell/v = (\ell \cdot 2m)/3$; ℓ is the momentum length of λ in the usual units $2\pi\hbar/a = 1$. The slow variation of ℓ with p_z is rather troublesome; a considerable simplification is obtained if we average ℓ over the appropriate range of p_z for each type of orbit. These values are $\bar{\ell}(A) = 1/4c$, $\bar{\ell}(B) = 1/4c$, $\bar{\ell}(C) = 1/c$, $\bar{\ell}(D) = 5/4c$ for the open orbits. The ranges of dp_z are all $s/2$ if $\tan\psi < 1/3$. If $1/3 < \tan\psi < 1/2$, the range of dp_z for the D orbits is $c/2 - s$ and $\bar{\ell}(D) = 1/4s + 1/2c$. For $1/2 < \tan\psi < 1$, the D orbits vanish while the range of dp_z for the C orbits changes to $1/(2\cdot(c-s))$. The value of $\bar{\ell}(C)$ remains the same however. $\bar{\ell}(E)$ and $\bar{\ell}(H)$ follow in a similar manner.

The periodic lengths of the orbits can now be evaluated:

$$\mu_o(A) = 2\kappa + 2\lambda(A) + \nu$$

$$= m/s + m/3c + m/3c$$

$$= m(1/s + 2/3c)$$

$$\mu_o(B) = 2\kappa' + 2\lambda(B) + \nu'$$
$$= (m/3)(4/c + 1/s),$$

and so on.

A check of equations 25 through 32 shows that we must still compute the following quantities for each type of orbit: $\langle v_z \rangle$, $\langle \mu v_x \rangle$, $\langle v_x \langle v_y' \rangle^{\mu} \rangle$, $\langle v_x \langle v_z' \rangle^{\mu} \rangle$, $\langle \mu v_x \langle v_x' \rangle^{\mu} \rangle$, and $\langle v_x \langle \mu' v_x' \rangle^{\mu} \rangle$ all integrated over the appropriate range of dp_z. By using $\mathfrak{I}$, this integration amounts to a simple multiplication. We will now compute these quantities for the A orbits.

$$\langle v_z \rangle = vc\kappa + 0\cdot\lambda + (-vs\nu) + 0\cdot\lambda + vc\kappa$$
$$= 3c/2s - s/2c \ .$$

$$\langle \mu v_x \rangle = \int_{\kappa}^{\kappa+\lambda} \mu v d\mu + \int_{\kappa+\lambda+\nu}^{\kappa+\lambda+\nu+\lambda} \mu(-v) d\mu$$
$$= -v(\lambda+\nu)\lambda$$
$$= -m/(8c^2) \ .$$

$$\langle v_x \langle v_z' \rangle^{\mu} \rangle = \int_0^{\mu_o} v_x d\mu \int_0^{\mu} v_z' d\mu'$$
$$= -v(v_{z\nu})\nu\lambda$$
$$= s/8c^2$$

$$\langle v_x \langle v_y' \rangle^{\mu} \rangle = -v(v_{y\nu})\nu\lambda = -1/8c \ .$$

Similarly,

$$\langle \mu v_x \langle v_x' \rangle^{\mu} \rangle = -v^2\lambda^2(\lambda/3 + \nu/2) = -1/72c^3$$
$$= -\langle v_x \langle \mu v_x' \rangle^{\mu} \rangle .$$

The evalution of all the other quantities follows in a similar manner.

In order to take account of the NFE surfaces in the second, third, fifth, and sixth zones, we have employed the following approximations:

$$\begin{aligned}
\sigma_{xx} &\approx 2\left[\sigma_{xx}(\text{fourth zone}) + (.39 + .25)m\right] \\
\sigma_{zz} &\approx 2\left[\sigma_{zz}(\text{fourth zone}) + (.39 + .25)/m\right] \\
\sigma_{xz} &\approx 2\left[\sigma_{xz}(\text{fourth zone})\right] \\
\sigma_{xy} &= 2\left[\sigma_{xy}(\text{fourth zone}) + .39 - .25\right] \\
\sigma_{yz} &= 2\left[\sigma_{yz}(\text{fourth zone})\right] \\
\sigma_{yy} &= 2\left[\sigma_{yy}(\text{fourth zone})\right]
\end{aligned} \tag{41}$$

The first three equations contain free electron approximtions for the .39 holes in the second and third zones and the .25 electrons in the fifth and sixth zones; we assume that the third zone necks are pinched off. The factor 2 arises because there are two sets of each type of orbit in the fourth zone and because the momentum volume occupied by .39 holes, for example, is $.78(2\pi\hbar/a)^3$. (In the high-field region, the Hall angle = $\pi/2$ in equation 12). We drop the

factor $2e^2\tau/(2\pi\hbar)^3$ for simplicity. The last three equations are exact in the high-field region.

The results of a computer program written to carry out such calculations (Appendix B) are presented in the graphs of figures 20 and 21. In figure 20 we have plotted the variation of $\bar{\sigma}$ with angle in the $\{100\}$ plane. We are using the convention $2\pi\hbar/a = 1$, $2e^2\tau/(2\pi\hbar)^3 = 1$, and $\alpha = 1$. As a result terms of order α^0, σ_{yy}, σ_{yz}, and σ_{zz}, appear in units 1/m; terms of order α, σ_{xy} and σ_{xz}, are dimensionless, while σ_{xx}, which is of order α^2, is measured in units of m. To determine ρ_{xx},

$$\rho_{xx} = \frac{\sigma_{yy}\sigma_{zz}-\sigma_{zy}\sigma_{yz}}{\left[(\sigma_{yy}\sigma_{zz}-\sigma_{zy}\sigma_{yz})\sigma_{xx} + \sigma_{yx}\sigma_{zy}\sigma_{xz} + \sigma_{zx}\sigma_{yz}\sigma_{xy} - \sigma_{xz}\sigma_{yy}\sigma_{zx} - \sigma_{zz}\sigma_{xy}\sigma_{yx}\right]} , \quad (39)$$

we first note that both factors in the numerator are given in units of $(1/m)^2$ while all six factors in the denominator are given in units of 1/m. It is obvious, then, from figure 20 that all terms containing σ_{xz} or σ_{zx} will be small so that

$$\rho_{xx} \approx \frac{\sigma_{yy}\sigma_{zz} - \sigma_{zy}\sigma_{yz}}{(\sigma_{yy}\sigma_{zz} - \sigma_{zy}\sigma_{yz})\cdot\sigma_{xx} - \sigma_{zz}\sigma_{xy}\sigma_{yx}} . \quad (42)$$

The magnetoresistance can be calculated from ρ_{xx} by noting that

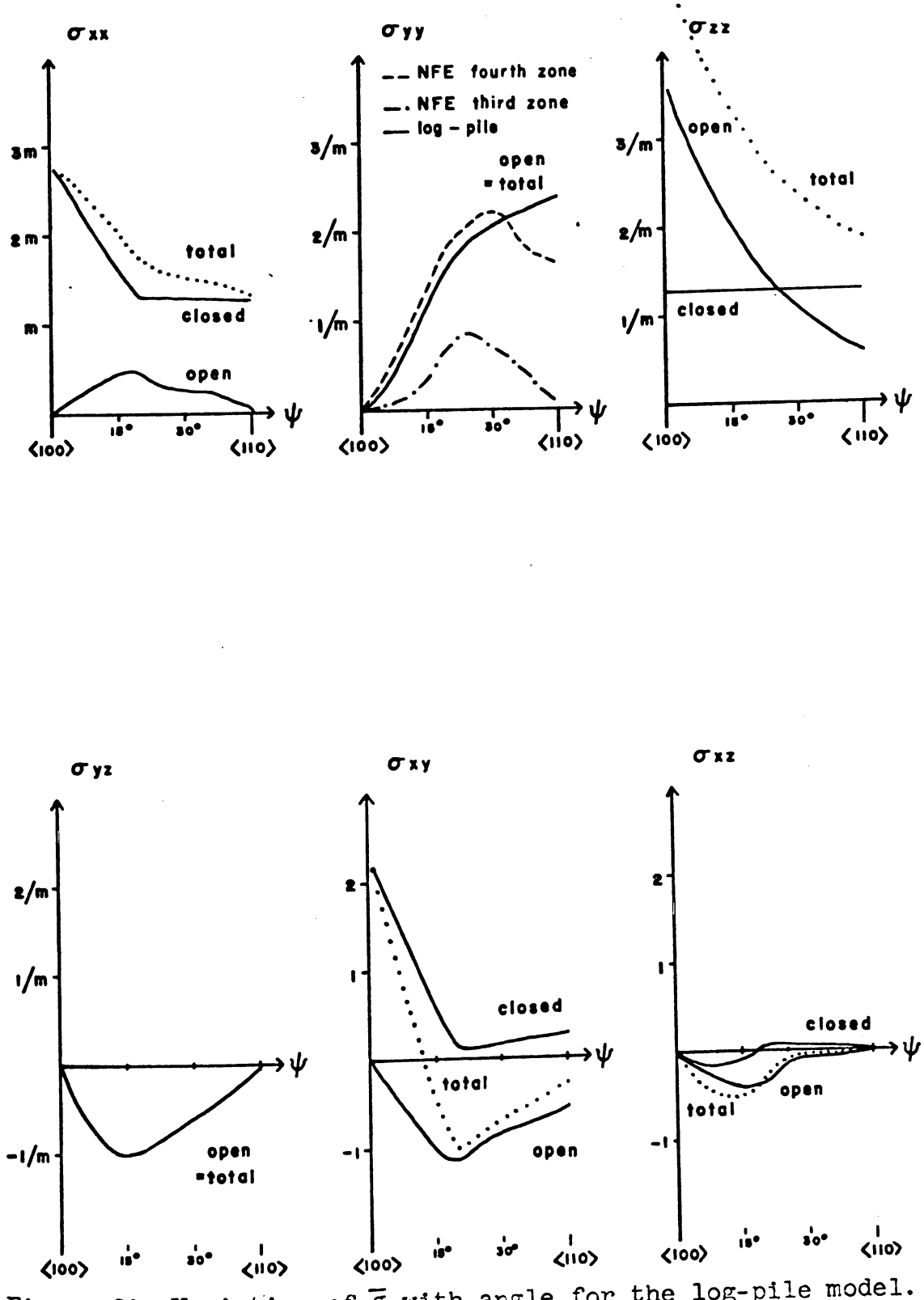

Figure 20 Variation of $\overline{\sigma}$ with angle for the log-pile model.

We

el

of

is

F

W

$$\left(\frac{2e^2\tau}{(2\pi\hbar)^3}\cdot\frac{(2\pi\hbar)^3}{a^3}\cdot m\alpha^2\right)^{-1} = \frac{ma^3}{2e^2\tau}\cdot(\omega_c\tau)^2$$

We estimate τ from the resistivity at B = 0 using a free electron approximation, $\rho = ma^3/ne^2\tau$ · n equals the number of conduction electrons per cell of volume a^3. This number is 28, so that

$$\Delta\rho/\rho = 14m\cdot\rho_{xx}(\omega_c\tau)^2 - 1 \ . \tag{43}$$

For some of the samples measured in this work, $\omega_c\tau \approx 5$, which gives

$$\Delta\rho/\rho \approx 350m\cdot\rho_{xx} - 1 \ . \tag{44}$$

The results of these calculations are given in figure 21. There are five distinct regions of ρ_{xx} depending on the number of open orbits. They are:

0°-5°	Case I behavior: a small layer of open orbits.
5°-8°	Case II behavior: a moderate number of open orbits whose importance is enhanced by the rapid decrease of σ_{xy} due to the thinning layer of hole orbits, H, and the thinning layer of electron orbits, E; all terms in (42) are important.
8°-13°	Case III behavior: a thick layer

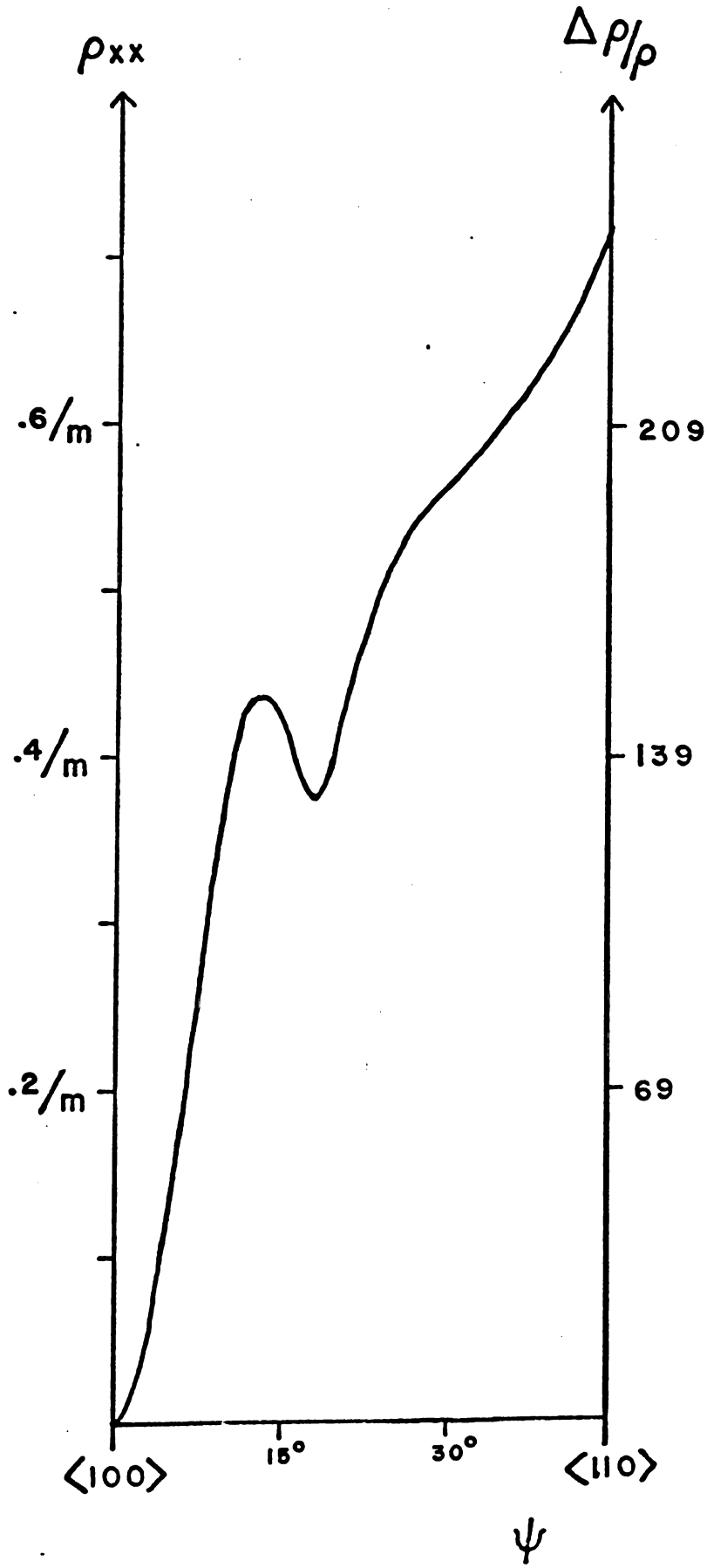

Figure 21
$\Delta\rho/\rho$ in $\{100\}$ plane for log-pile model.

of open orbits aided by the vanishing of σ_{xy} at 12° results in $\rho_{xx} \approx 1/\sigma_{xx}$.

13°-20° Case II and III behavior: a thicker layer of open orbits is moderated by a decreasing σ_{xx} so that the first term in the denominator of (44) is $\approx$ constant. The second term is increasing, however, causing ρ_{xx} to decrease.

20°-45° Case III behavior: $\rho_{xx} \approx 1/\sigma_{xx}$; σ_{xx} is in turn dependent on fourth zone open orbits for its variation.

In addition to the complete calculation of σ for this model, we have determined σ_{yy} from the third and fourth zone open orbits of the NFE model. The results of that calculation, also shown in figure 20, suggest that the log-pile model is a good approximation to the NFE fourth zone and that the open orbits from these surfaces do dominate those of the third zone even without the known reduction in the size of its copper-like necks. The dip in the NFE fourth zone curve occuring over the range 30°-45° warns us to look at ρ_{xx} in this region with some suspicion since σ_{xx} may also look somewhat differently in this interval.

si
si
cr
as
wi
fr
s
r
r
e

3. Growth and Preparation of Samples

In this section we discuss the techniques used to grow single crystals of $AuAl_2$, $AuGa_2$, and $AuIn_2$. We also consider the X-raying, sparkcutting, and mounting of the crystals. The general procedure for making the alloys was as follows. A small high-purity graphite crucible, usually with an alumina insert, was outgassed in a Lepel induction furnace, the temperature of which was increased in several steps up to 1200°C in such a manner that the pressure remained at 10^{-4} mm Hg. The pure metals were etched if necessary, washed with distilled water, and rinsed with ethyl alcohol. The desired amount of Al, Ga, or In (typically 2.5, 6, and 8 grams) was then placed in the crucible. Its weight was determined to .1 milligram on a Mettler balance and the amount of gold necessary was computed and deposited in the crucible. The crucible was then placed in the induction furnace and heated to 100°C above the melting point of the compound (cf. Table IV) either at a pressure of less than 10^{-4} mm Hg or in an argon atmosphere. Mixing was accomplished by agitating the melt mechanically and by the action of the rf field.

Several methods of growth were attempted before high purity single crystals were produced. The first success was obtained by vertical zone refining of $AuGa_2$ with an rf coil. The samples, prepared with the exact stoichiometry, had residual resistance ratios up to 250 at the bottom of

Table IV. Properties of the AuX_2 compounds. (After Jan *et al.*, ref. 13)

	$AuAl_2$	$AuGa_2$	$AuIn_2$
Resistivity at 295°K (μΩ-cm)	8	13	8
Lattice parameter at 4.2°K (angstroms)	5.988	6.055	6.487
Melting Point (°C)	1060	492	544

the crystal. The graphite boat used was grooved so that the dimensions of the crystals were 1/16" x 1/16" x 4". Three experimental runs on these crystals were disappointing. At 55 kilogauss, the largest magnetoresistance observed was 5 and no decision could be made on the state of compensation of $AuGa_2$ since the field dependences were $B^{1.0 \pm .4}$ for all measured directions. The third crystal investigated, which had $\underline{J}$ approximately parallel to <111>, did have a deep minimum with B ~ || <112> in its transverse magnetoresistance. Hall effect measurements were inconclusive: $1.2 < n_e - n_h < 1.5$ for several different general field directions.

For three reasons we decided to switch our concentration to $AuAl_2$. Straumanis and Chopra had determined that the extent of the $AuAl_2$ phase is 78.18 - 78.94 % weight Au[26]. At the stoichiometric ratio there are .152 empty lattice sites per unit cell in the Al sublattice and .076 empty lattice sites in the Au sublattice. But at the Al-rich border there was strong evidence that all of the Al vacancies were filled. A crystal grown at the Al-rich border of the phase should be appreciably better than one prepared at stoichiometry. The standard Bridgeman technique was apparently not very successful when $AuGa_2$ was prepared up to two atomic percent off stoichiometry[27]. Finally, $AuGa_2$ has a rather high room temperature resistivity of 13 μΩ-cm. compared to $AuAl_2$'s 8 μΩ-cm; this means

that $\omega_c\tau$ (free electron) for $AuAl_2$ will be about 50% larger than that for a $AuGa_2$ crystal with the same residual resistance ratio.

Our first attempt to grow Al-rich $AuAl_2$ in a graphite crucible was a failure. The crystal, which wet the crucible, had a residual resistance ratio of 33. We discovered that near 1000°C Al forms a carbide with the graphite; so we decided to place an alumina insert inside the graphite. The dimensions of this insert were 1.5" long and .42" inside diameter. The bottom of this alumina crucible was bowl-shaped so there was some premature concern that it would be difficult to grow single crystals. The crucible and its contents were, as usual, sealed in a vycor tube filled with argon and lowered thru a three turn rf coil at a speed of 1/2" per hour. The temperature of the graphite was measured with an optical pyrometer and the rf current adjusted so that the hottest portion of the crucible was 60°C above the melting point of $AuAl_2$. Upon breaking the vycor, we discovered that $AuAl_2$ had wet the alumina; however, the alumina insert had cracked due to differential contraction upon cooling, and it was possible to pry off the pieces of alumina clinging to the $AuAl_2$ slug. Back reflection X-ray photographs indicated that the crystal was single. The first two samples spark-cut from this slug had residual resistance ratios of 400 and 550 with $\underline{J}$'s parallel to <111> and <100> respectively. We designate these samples as Al <111> and Al <100>; here A

refers to the compound, 1 to the slug, and the numbers in brackets to the current direction.

Since studies similar to that of Straumanis and Chopra had not been published for $AuGa_2$ and $AuIn_2$, it was necessary to determine experimentally the dependence of their residual resistance ratios on the excess concentration of one of their constituents. Slugs of 0.0, 0.1, 0.2, 0.3, 0.4, and 0.5% weight excess Ga were prepared in the same manner as Al. The average residual resistance ratios of crystals cut from these slugs were 190, 540, 680, 710, 660, and 200 respectively. The points in figure 22 representing individual samples show a considerable spread about the average. It should be noted here that traces of Ga were found on the surface of the slugs with 0.2 - 0.5% excess Ga. This may indicate that the phase exists to about .2% weight excess Ga; as a larger amount of Ga is added it is energetically more favorable for the charge to reject this Ga, but at 0.5% the Ga phase begins to coexist with the $AuGa_2$ phase inside the slug. See figure 23.

A $AuIn_2$ slug of exact stoichiometry had a residual resistance ratio of 60. By varying the composition to both sides, the highest value achieved was 75 in a .1% In excess $AuIn_2$ slug. Several growth methods were tried in an attempt to improve on this value; these included vertical zone refining and horizontal zone refining and leveling. Crystals prepared in such a manner had residual resistance ratios less than 60.

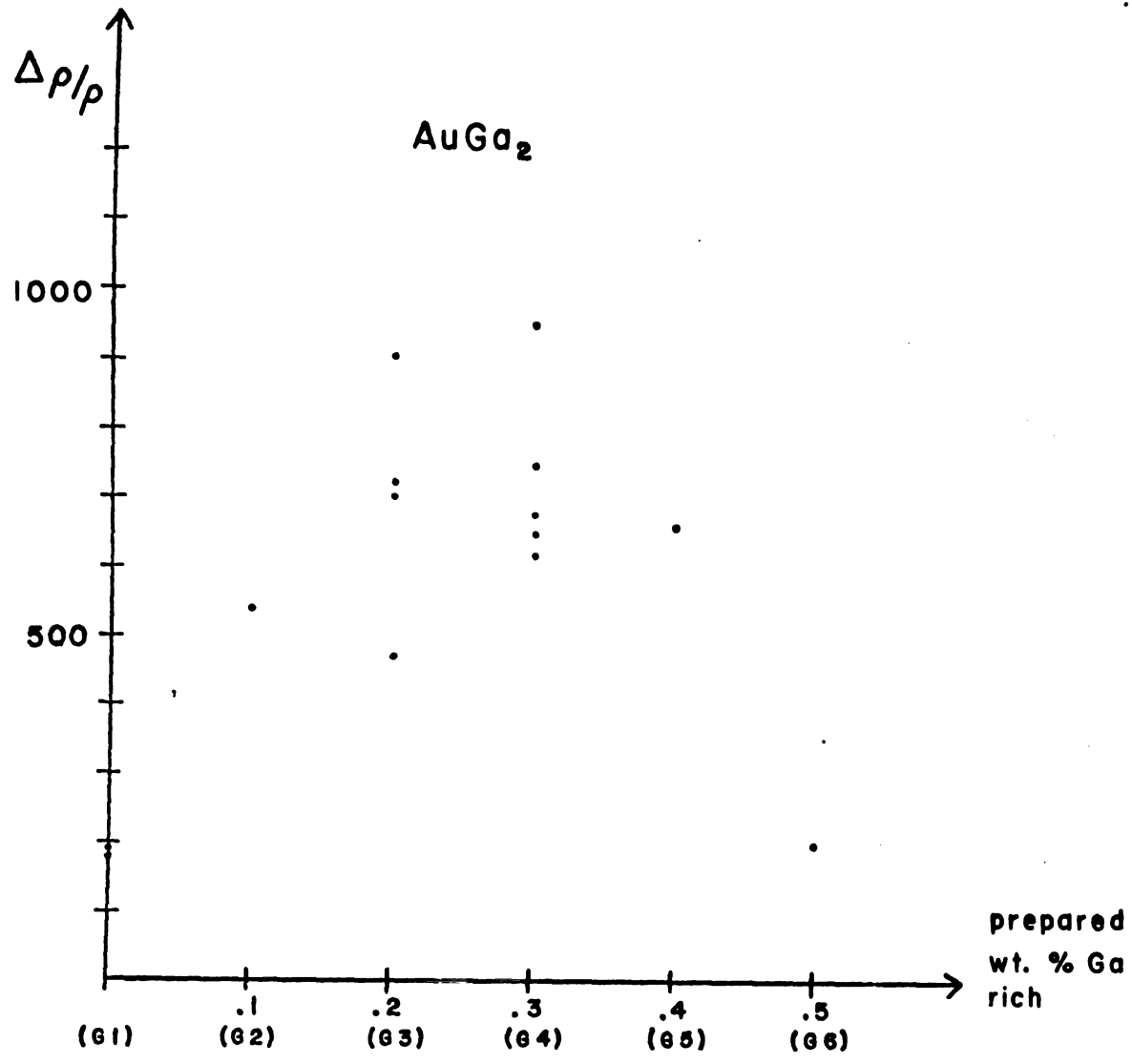

Figure 22 RRR of $AuGa_2$ crystals vs. excess Ga concentration.

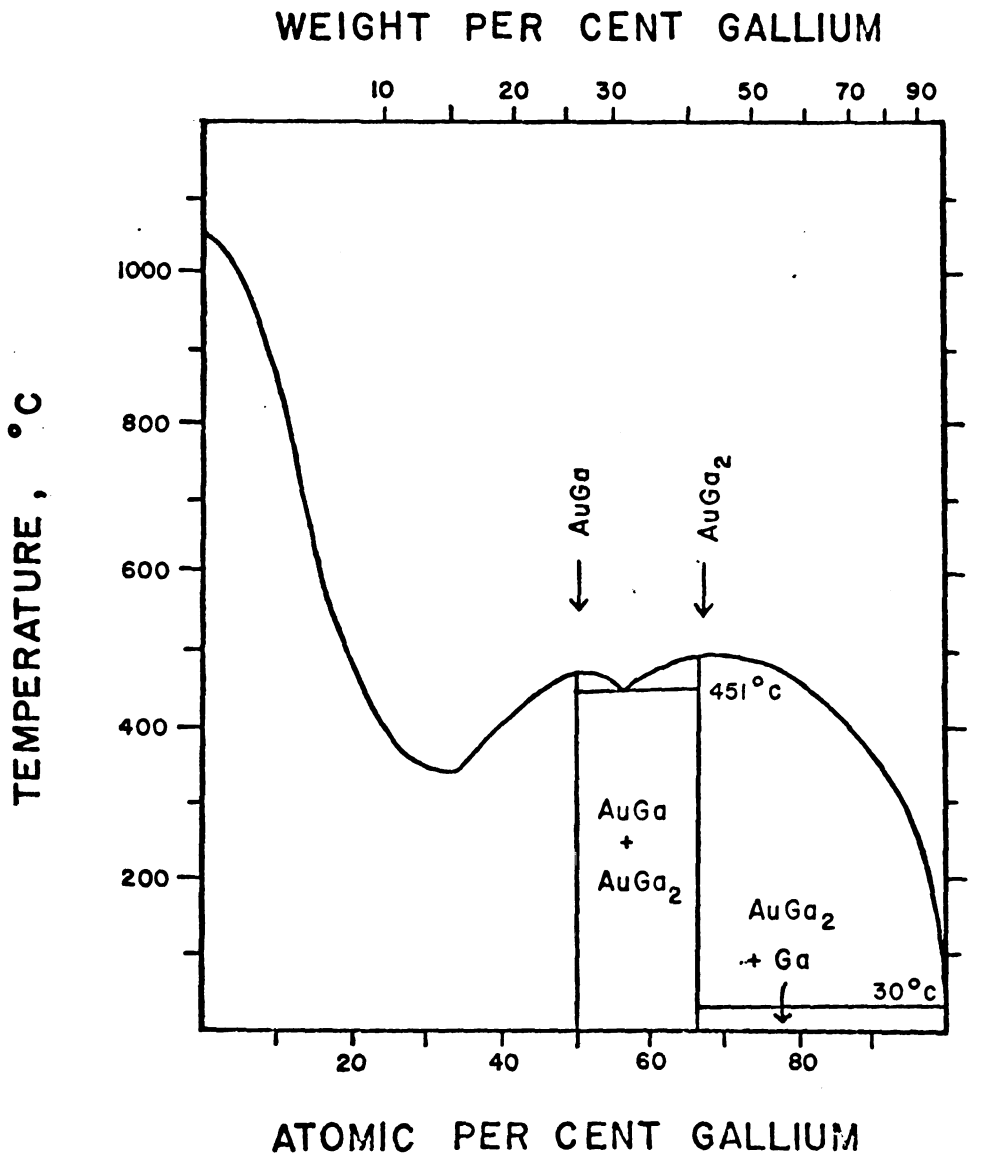

Figure 23 Phase diagram of Au-Ga.

Table V is puzzling for at least two reasons: $AuIn_2$ cannot be prepared to within even a factor of ten as highly ordered as $AuGa_2$, and $AuAl_2$ of exact stoichiometry can be grown with residual resistance ratios greater than 100 despite the fact that 1.9% of all the sites are empty according to Straumanis and Chopra. This latter effect is extremely peculiar because Sellmyer[3] has shown that AuSn qualitatively obeys the same empirical law as many of the elements,

$$RRR \sim 10^4 / I , \quad 1 \lesssim I \lesssim 10^4 \tag{45}$$

Here I is impurity or vacancy content in parts per million (p.p.m.). Thus 49's, 59's, and 69's metals typically have residual resistance ratios of 10^2, 10^3, and 10^4. This is reasonable because metals have room temperature resistivities of 1 - 10 μΩ-cm, while the resistivity due to impurities or vacancies in dilute alloys is from 1 - 10 μΩ-cm. per atomic %. Assuming that $AuAl_2$ obeys this law, a residual resistance ratio of 140 is equivalent to I = 71 p.p.m. or .0071%. This compares very unfavorably with the 1.9% from the Straumanis and Chopra study. The difference cannot be explained by the fact that compounds prepared with stoichiometric proportions may grow off stoichiometry; consider the limiting case of the Al-rich border: we expect I = .634% but, experimentally, I ~ .0018%. A possible explanation is that vacancies are segregated and not dispersed throughout the material; adding extra Al or Ga

Table V. RRR of AuX_2 crystals

	$AuAl_2$ prepared		$AuGa_2$ prepared		$AuIn_2$ prepared	
	exact	Al-rich	exact	Ga-rich	exact	In-rich
largest RRR	140[13]	550	250	904	60	75

simply cuts down on the size and number of aggregates. The variation of residual resistance ratio over the slugs tends to support this belief.

In this discussion we have neglected the residual resistivity due to the impurities in the Au, Al, Ga, and In. The ASARCO gold and indium had $I \sim 9$ p.p.m. For the MRC aluminum, $I \sim 2$ p.p.m., and for the ALCOA gallium, $I \sim 1$ p.p.m. Table VI shows that the residual resistance ratios of both $AuAl_2$ and $AuGa_2$ are appreciably affected by the impurity content of the starting material if the law $RRR \sim 10^4 / I$ holds. For some combinations of impurity and host, a law in which 10^4 is replaced by 10^5 better fits the resistivity data; this is the case for Mg in Cd and Sn in In. The numbers in parentheses are the appropriate changes which, in this case, clearly indicate order limiting of the residual resistance ratio. The use of 69's gold in these compounds could determine a suitable form of the law and possibly provide a most desirable increase in the average relaxation time.

Samples were obtained by placing each slug in a small brass cup and securing with one metal and five nylon retaining screws. This cup was screwed into the face of a goniometer and the slug oriented to within 1° of the desired current axis with the standard Laue back reflection technique. The entire goniometer assembly was now mounted on a platform which was the high voltage side of a Servo Met spark cutter. A stainless steel tube attached to the

Table VI. Impurities in AuX_2 crystals.

	$AuAl_2$	$AuGa_2$	$AuIn_2$
prepared RRR	550	904	75
I from eqn. 45 (p.p.m.)	18 (180)	11 (110)	133 (1330)
I from starting material (p.p.m.)	4.3	3.7	9
I from ordering (p.p.m.)	13.7 (175.7)	7.3 (106.3)	124 (1321)
RRR (if limited only by impurities)	2300 (23000)	3720 (37200)	1110 (11100)
RRR (if limited only by ordering)	770 (570)	1360 (940)	80 (75)

working arm at ground potential then cut out a cylindrical sample. Non-metallic debris was removed through a side arm of the tube connected to a water pump. Since it is impossible to obtain X-ray pictures from a spark-cut surface of these compounds and etching is also of no benefit, the crystals were spark-planed on four sides to give a rectangular cross section. This is an extremely tedious process but well worth the effort when attempting to mount four orthogonal Hall probes. The final shape was roughly 10mm x 1.5mm x 1.5mm. Usually, major symmetry axes were perpendicular to each face.

Mounting six potential and two current leads to a sample this size requires that it be firmly mounted to a large heat sink. The sites selected for probe placement were lightly abraded with a pointed object or a pencil sand blaster. This area was then tinned with solder until a very small bead was formed (less than .5 mm in diameter). The leads could then be quickly soldered to such sites. Wood's metal solder and Sta-Clean flux were used for $AuGa_2$ and $AuIn_2$. Rose's alloy was found superior for $AuAl_2$. Table VII lists those samples selected for experiments.

Table VII. Samples selected for experiments.

Date	Crystal	RRR	B(kG)	Type of Data
8-65	G(random$_1$)	230	55	MR and Hall
3-66	G(random$_2$)	205	55	MR and Hall
6-66	G<111>	160	55	MR
9-66	G1<110>	190	85	MR
	G1<100>	200	140	MR
	G<111>	160	140	MR
	G(random$_1$)	230	140	MR
	* I1<100>	60	140	MR
	* A1<100>	550	140	MR
	* A1<111>	400	140	MR
8-67	G4{110}	620	50	MR and Hall
	G4{111}	775	50	MR and Hall
11-67	* G3{100}	475	150	MR and Hall
	* G3<100>	725	150	MR and Hall
	* G3<110>	904	150	MR and Hall
	* A1<100>	500	150	MR and Hall
	* A2(random)	550	150	MR and Hall
	* I2<110>	75	150	MR and Hall

* Interpretation of data in section 5 is based on evidence from these samples.

4. Apparatus and Experimental Techniques

The experiment consists of measurements of the magnetoresistance and Hall coefficient as a function of the magnitude and direction of the magnetic field. The apparatus used at Michigan State has already been described.[3] Since we will just present data taken at the 150 kG fields available at the Francis Bitter National Magnet Laboratory, we will only consider the apparatus kindly provided for our use there by Dr. D. J. Sellmyer.[28]

Figure 24 is a schematic diagram of the apparatus and circuitry. The apparatus, shown in figure 25, permits the field to be oriented along any crystallographic direction for an arbitrary sample axis. This is accomplished by use of the worm gear which changes the tip angle φ, and the spiral gear which changes ψ. The sample is mounted on an insert, I, which is removeable so that the crystal can be positioned by Laue back reflection techniques until a certain axis is parallel to BB'. The advantage of this positioning is that all rotations of ψ for any φ will be straight lines on a stereogram centered at $\langle lmn \rangle$ if $\underline{J}$ is in the plane $\{lmn\}$. This is seen in figures 26 a and b. The drive rod D is connected at the top of the cryostat to a motor whose speed was normally adjusted to achieve a 180° rotation of ψ in 10 minutes. Rotation plots were recorded continuously on an X-Y recorder with the X axis signal coming from a linear ten-turn potentiometer coupled to drive rod D. We estimate

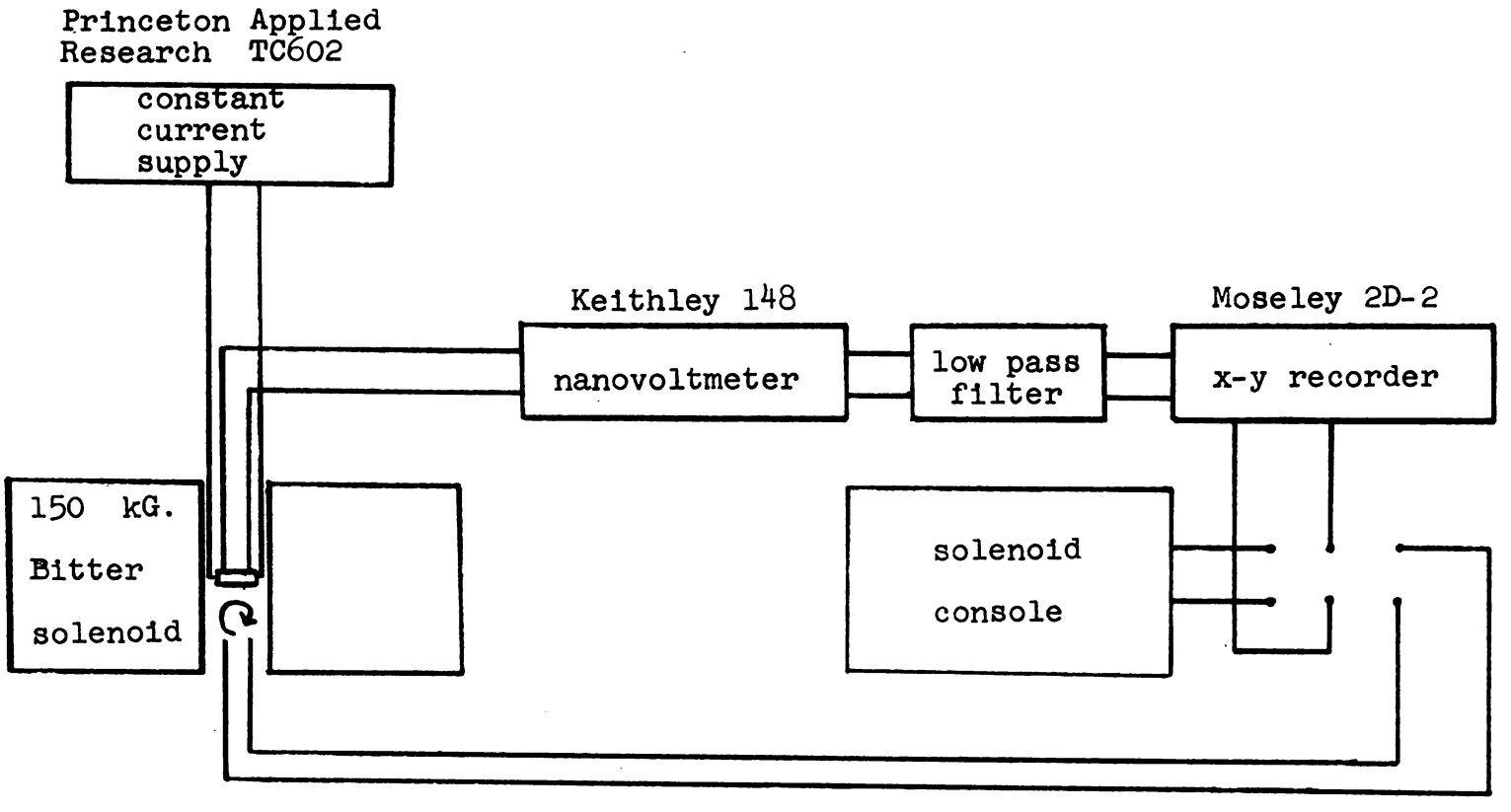

Figure 24. Schematic of apparatus and circuitry.

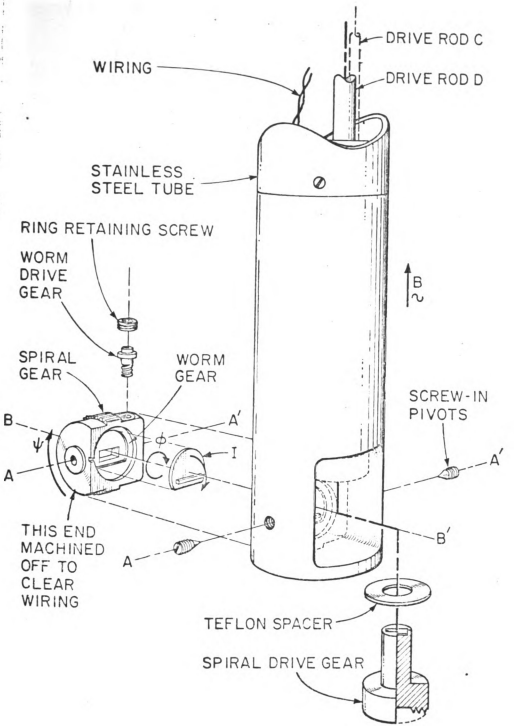

Figure 25 Experimental apparatus (after Sellmyer, ref. 28)

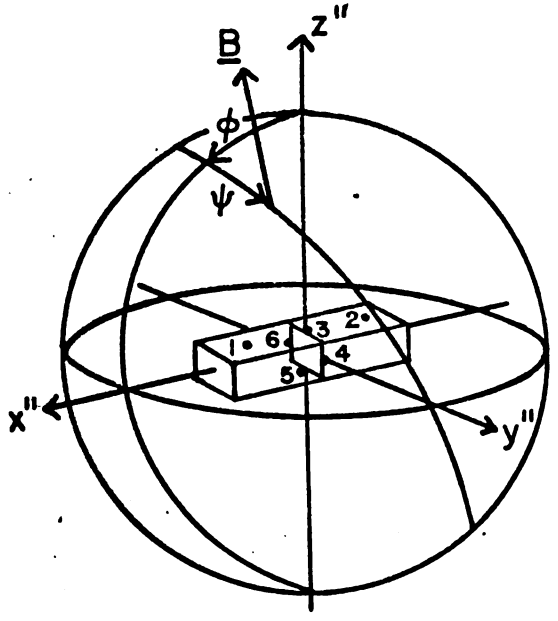

Figure 26a Rotation and tipping geometry in the sample coordinate system. Magnetoresistance leads are connected at 1,2; Hall leads at 3, 4, 5, 6.

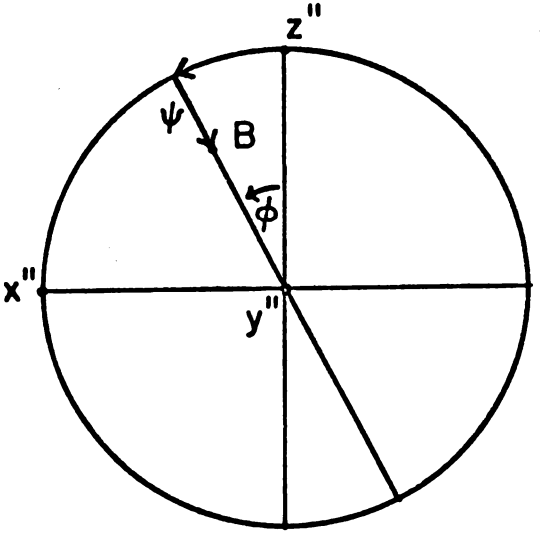

Figure 26b Stereogram showing the effect in the sample coordinate system of rotating and tipping the sample in the magnetic field.

that the maximum total error in our knowledge of $\underline{B}$ with respect to the crystallographic axes is $\pm 2^{\circ}$. This estimate is based on accumulating the errors due to x-raying, spark-cutting and gear backlash. If there are sharp extrema in a rotation plot, the position is usually known to $\pm .5^{\circ}$.

Analysis of Tipping Arrangement

Consider figure 27. In the xyz coordinate system, the current density is

$$\underline{J} = R^{-1}_{xy'}\underline{J}'' = \begin{pmatrix} 1 & 0 & 0 \\ 0 & \cos\psi & -\sin\psi \\ 0 & \sin\psi & \cos\psi \end{pmatrix} \begin{pmatrix} \cos\varphi & 0 & -\sin\varphi \\ 0 & 1 & 0 \\ \sin\varphi & 0 & \cos\varphi \end{pmatrix} \begin{pmatrix} J_o \\ 0 \\ 0 \end{pmatrix}$$

$$= \begin{pmatrix} \cos\varphi & 0 & -\sin\varphi \\ -\sin\psi\sin\varphi & \cos\psi & -\sin\psi\cos\varphi \\ \cos\psi\sin\varphi & \sin\psi & \cos\psi\cos\varphi \end{pmatrix} \begin{pmatrix} J_o \\ 0 \\ 0 \end{pmatrix}$$

$$= \begin{pmatrix} \cos\varphi \\ -\sin\psi\sin\varphi \\ \cos\psi\sin\varphi \end{pmatrix} \cdot J_o$$

The double primed coordinate system is the sample's. We wish to measure voltages in the sample system. Thus,

$$\underline{E} = \bar{\rho} \cdot \underline{J}$$
$$\underline{E}'' = R_{xy'}\bar{\rho}R^{-1}_{xy'} \cdot \underline{J}'' \ .$$

Let us begin by considering the case of all closed orbits.

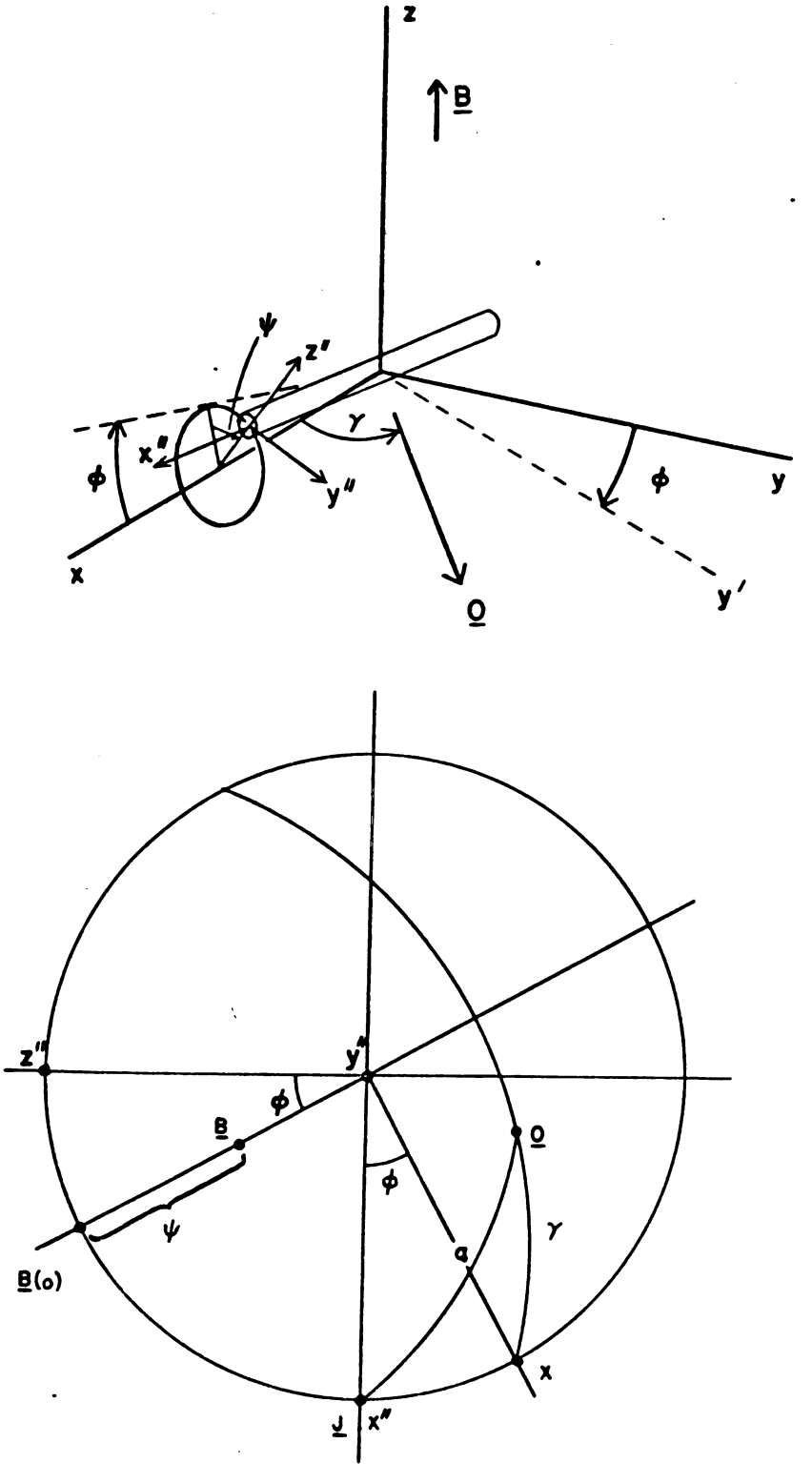

Figure 27 Rotation and tipping geometry in the laboratory coordinate system.

$$\bar{\rho} = \begin{pmatrix} aB^{o} & \rho_{xy} & aB^{o} \\ \rho_{yx} & aB^{o} & aB^{o} \\ aB^{o} & aB^{o} & aB^{o} \end{pmatrix}$$

By straightforward matrix multiplication,

$$\bar{\rho}'' = \begin{pmatrix} aB^{o} & \cos\varphi\cos\psi\rho_{xy} & \sin\psi\rho_{yx} \\ \cos\varphi\cos\psi\rho_{yx} & aB^{o} & -\sin\varphi\cos\psi\rho_{yx} \\ \sin\psi\rho_{xy} & -\sin\varphi\cos\psi\rho_{xy} & aB^{o} \end{pmatrix} .$$

Therefore,

$$\begin{pmatrix} E''_x \\ E''_y \\ E''_z \end{pmatrix} = \begin{pmatrix} aB^{o} \\ \cos\varphi\cos\psi\rho_{yx} \\ \sin\psi\rho_{xy} \end{pmatrix} \cdot J_o .$$

By measuring E''_y and E''_z we can determine ρ_{yx},

$$\rho_{yx} = \frac{1}{J_o}\left(\frac{E''^2_y + E''^2_z}{\cos^2\varphi\cos^2\psi + \sin^2\psi}\right)^{1/2} . \tag{46}$$

Careful analysis of figure 27 shows that

$$\cos^2\varphi\cos^2\psi + \sin^2\psi = \cos^2\beta .$$

β is the angle of departure of the crystal from the x-y plane. Thus

$$\rho_{yx} = \frac{(E''^2_y + E''^2_z)^{1/2}}{J_o\cos\beta} \tag{47}$$

Now consider $\underline{J}$ to be || to x and allow orbits to be

open in a direction which makes an angle γ with x and, of course, $\pi/2$ with $\underline{B}$. One can easily show that

$$\bar{\rho} \propto \begin{pmatrix} B^2\cos^2\gamma & -B^2\cos\gamma\sin\gamma & B^0 \\ -B^2\cos\gamma\sin\gamma & B^2\sin^2\gamma & B^0 \\ B^0 & B^0 & B^0 \end{pmatrix} . \tag{48}$$

If the crystal is now rotated by arbitrary angles φ and ψ, we find that

$$E''_x \propto \Delta\rho/\rho \propto B^2(\cos\gamma\cos\varphi + \sin\gamma\sin\varphi\sin\psi)^2 . \tag{49}$$

Inspection of figure 27 gives us

$$\Delta\rho/\rho \propto B^2\cos^2\alpha \ . \tag{50}$$

α is the angle between the current and open orbit directions. The B^2 dependence due to open orbits is washed out if the open direction is about 90° from $\underline{J}$. Note that this must always occur when $\underline{B}$ is near $\underline{J}$.

Experimental Difficulties

The ideal magnetoresistance behavior of B^0 or B^2 is not usually achieved in practice because $\langle\omega_c\tau\rangle$ is not much greater than 1. Estimates of $\omega_c\tau$ give values of 3-10 at 150 kG for three of the samples (Table IX). The $\omega_c\tau$ of G3<110> is possibly greater than 10, while that of both $AuIn_2$ crystals is less than 3. Copper samples with $\omega_c\tau \approx 10$ have a "quadratic" behavior of $B^{1.8-2.0}$. (29) The reason for the exponent not achieving 2.0 is simply explained.

Assume orbits open in the x-direction; for simplicity, take

$$\rho_{xx} = \frac{\sigma_{yy}\sigma_{zz} - \sigma_{zy}\sigma_{yz}}{(\sigma_{yy}\sigma_{zz} - \sigma_{zy}\sigma_{yz})\,\sigma_{xx} - \sigma_{zz}\sigma_{xy}\sigma_{yx}} \tag{42}$$

If $\alpha = 1/eB\tau$ is not much less than 1,

$$\sigma_{xx} = \alpha^2\, a_{xx} + \alpha^4 b_{xx},$$

$$\sigma_{yy} = \quad a_{yy} + \alpha^2 b_{yy},$$

$$\sigma_{zz} = \quad a_{zz} + \alpha^2 b_{zz},$$

$$\sigma_{xy} = \alpha\, a_{xy} + \alpha^2 b_{xy},$$

$$\sigma_{yz} = \quad a_{yz} + \alpha\, b_{yz}.$$

Then,

$$\rho_{xx} = a_1(\omega_c\tau)^2 + a_2\,(\omega_c\tau) + a_3 + \ldots\ldots$$

The deviation from quadratic behavior depends on the value of $\omega_c\tau$ and factors contained in the a_{ij} and b_{ij}.

Chambers[30] has formulated an explanation of poor saturation if there are extended orbits for a certain direction of the field. For an electron which only traverses a section along one side of a closed orbit before colliding, the orbit appears to be open. Thus in the field region for which $\omega_{closed}\cdot\tau \gg 1 \gg \omega_{ext}\cdot\tau$, $\rho_{xx} \propto B^2$; at fields such that $\omega_{ext}\cdot\tau \gg 1$, ρ_{xx} will saturate. Since we are only in the region $\omega_{ext}\cdot\tau > 1$, poor saturation is to be expected. (ext = extended)

Values of the exponent, m, are calculated by sweeping the field to 150 kG at fixed angle or by performing two rotations at different fields, usually 130 and 145 kG. Unless otherwise noted m is the high-field exponent.

Because of experimental limitations, the procedure of reversing both current and field directions should be used in making measurements. We define V_{MR} as that component of the voltage measured on contacts 1-2 in figure 26 which reverses sign with current but not with field. V_H is defined as that part of the voltage on probes 3-5 or 4-6 which is odd in both current and field. It can be shown[3] that

$$V_{MR} = \frac{1}{4}\left[V(+I, +B) + V(+I, -B) - V(-I, +B) - V(-I, -B)\right]$$

$$V_H = \frac{1}{4}\left[V(+I, +B) - V(+I, -B) - V(-I, +B) + V(-I, -B)\right]$$

These current and field reversals eliminate thermal voltages from both V_{MR} and V_H. They also eliminate magnetoresistive voltages from V_H and Hall voltages from V_{MR} caused by probe misalignment. Since the unwanted voltages appearing on the transverse probes can be as large as V_H, it is imperative that V_H be measured in this manner. The unwanted voltages appearing on contacts 1-2 are usually small for field directions supporting open orbits so that $V_{MR} = V_{12}(+I, +H)$ to a very close approximation. For general field directions, however, $V_{12}(+I, +H)$ can be quite small ($\sim 5\ \mu v$) and errors can be appreciable. Unfortunately, the amount of magnetoresistance data required for a complete study of a metal far outweighs the necessary amount of Hall data. A compromise solution is in order: selected measurements on 1-2 are made in the rigorously correct manner to

estimate the magnitude of the discrepancies to be expected when only $V_{12}(+I, +H)$ is measured.

From Eq. (48) one can see that the dominant voltage on the transverse probes will be proportional to $B^2 \cos \alpha \sin \alpha$ when there are open orbits. We have not studied these transverse - even voltages in any systematic way because the time-consuming field and current reversals must be employed in this case also.

Voltage measurements were not appreciably affected by the noise level of .05 - .5 microvolts at the highest fields. With a two ampere sample current, Hall voltages were typically 10 μ volts and resistive voltages from 5 to 500 μ volts at 150 kG.

Summary of High-Field Galvanomagnetic Properties

The constant relaxation time treatment given in section 2 enabled us to calculate the magnitude of all the ρ_{ij} as well as their field dependences. A summary of those high-field galvanomagnetic properties which do not depend on any assumptions about the relaxation time is given in Table VIII. These results of the Lifshitz theory are dependent only on the requirements that a semiclassical treatment is valid and that a certain field, B_o, is exceeded. B_o is that field at which all carriers complete many cyclotron orbits before being scattered.

Table VIII Summary of High-Field Galvanomagnetic Properties

Type of orbit and state of compensation	Magnetoresistance	Hall Field *
1. All closed and uncompensated ($n_e \neq n_h$)	$\sim B^0$	$\dfrac{-\Omega B}{(n_e - n_h)\lvert e\rvert \cos\beta}$
2. All closed and compensated ($n_e = n_h$)	$\sim B^2$	$\sim B$
3. Open in one direction**	$\sim B^2 \cos^2\alpha$	$\sim B$
4. Open in two directions	$\sim B^0$	$\sim B^{-1}$
5. Singular field direction	$\sim B^0$	$\dfrac{-\Omega B}{(n_e - n_h \mp \Delta n)\lvert e\rvert \cos\beta}$

* i.e. electric field per unit current density; β is the complement of the angle between $\underline{J}$ and $\underline{B}$.

** $\underline{J}$ makes an angle α with the open orbit direction.

5. Experimental Results and Discussion

Since measurements of the effective number of carriers per primitive cell most clearly indicate deviations from NFE behavior in AuX_2, we begin with a presentation of Hall data and a discussion of possible changes in the model. We follow this section with evidence from the magnetoresistance behavior of these compounds which corroborates our interpretation of the Hall data.

High-field magnetoresistance is, potentially, a more useful phenomenon for investigating a Fermi surface than the Hall effect, but it is also more difficult for two reasons. The first is experimental: a large amount of data is required to make a quantitative comparison with a model and, more importantly, data determining the angular extent of the two-dimensional regions must be taken at field directions which have carriers of unusually large cyclotron masses. Schoenberg has said that "the poor man's dHvA effect involves looking only at low mass pieces of the Fermi surface". In a similar vein it might be said that the poor man's magnetoresistance experiment is concerned with measurements in high symmetry planes only. Secondly, if a good model of the surface is not available in an analytic form so that a computer can look for field directions supporting open orbits, one must be both clever and diligent to make quantitative comparisons between theory and experiment.

Hall Effect in AuX_2

General Field Directions

From Table VIII and the discussion on page 71, we have

$$E_H = \frac{-\Omega B}{(n_e - n_h)|e|\cos\beta}$$

in the high field region at a general field direction supporting no open orbits. For the NFE model, AuX_2 have seven conduction elections per primitive cell, one full zone, and two hole zones giving $n_e - n_h = 1$. Measurements of V_H vs. B enable us to determine $n_e - n_h$ and hence to check the above assumptions about the NFE model.

The results for a $AuAl_2$ crystal with a residual resistance ratio of 550, (A2(random)), are shown in figure 28. Each curve represents a general field direction for which the magnetoresistance approaches B^0 dependence. For typical sample cross section (1.5 mm x 1.5 mm), current (2 amps), and at 150 kG, $V_H = -8\ \mu$ volts/$(n_e - n_h)$. We have shifted these curves vertically so that a line tangent to them at 150 kG passes through the origin; we can then simply use the value of V_H(150 kG) to determine $n_e - n_h$.

Table IX lists the values of $n_e - n_h$ for $AuAl_2$ and $AuGa_2$. The last three $AuGa_2$ values are for a crystal with a residual resistance ratio of 475, G3 $\{100\}$. The first value is for a crystal with a residual resistance ratio of 725, G3 <100>. The exponent, m, of B in the magnetoresistance is also given. This exponent is a better measure of the attainment of the high-field region than the linearity

Figure 28 V_H vs. B in $AuAl_2$ for general field directions supporting no open orbits.

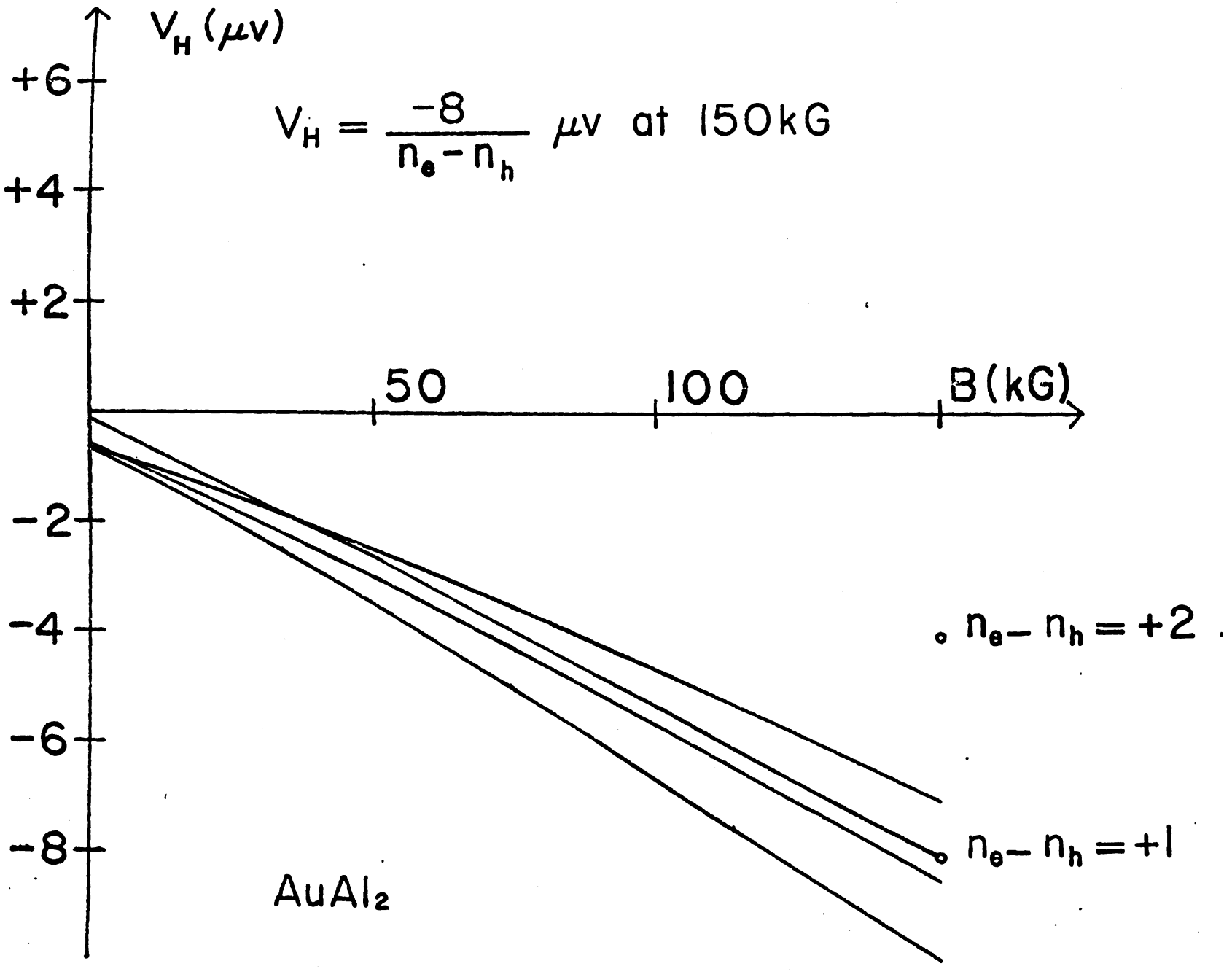
V_H (μv)
+6
+4
+2
-2
-4
-6
-8
$V_H = \frac{-8}{n_e - n_h}$ μv at 150kG
50
100
B(kG)
$n_e - n_h = +2$
$n_e - n_h = +1$
$AuAl_2$

of the Hall curves. Generally, the higher m's correspond to larger deviations from $n_e - n_h = 1$. Note that $AuAl_2$ tends to have $n_e - n_h < 1$, while in $AuGa_2$ $n_e - n_h$ is usually greater than 1. Any deviation of $n_e - n_h$ from integral values indicates that some carriers are still not in the high-field region because of their low mobility (high cyclotron mass). The sign of the deviation indicates whether such carriers are electrons or holes[1]. Thus in $AuAl_2$ electrons appear to be the lower mobility carriers while in $AuGa_2$ the situation is reversed. The $AuAl_2$ Hall behavior is fairly easy to understand on the model. The vast majority of the fourth zone closed electron orbits are extended over several zones. From plots similar to figure 16, one can easily show that the cyclotron masses of these orbits are several times the free electron mass. From the same plots, the cyclotron masses of the third zone hole orbits are calculated to be usually less than the free electron mass. Thus we predict that the number of electrons not in the high field region will be greater than the corresponding number of holes, $n_e - n_h < 1$. On the NFE model, the $AuGa_2$ Hall values are hard to understand. Since V_H/IB is known within 1%, the only other source of important experimental error is in the measurement of the sample dimensions. These were made with two micrometers; values were averaged for several attempts. We estimate the possible overall experimental error at less than 5%. There is only one group of field directions on the NFE model for

which the third zone extended orbits have cyclotron masses larger than those of the fourth zone. It is just outside the two-dimensional region of figure 19 and within the <110>, <111>, <211> spherical triangle. The $AuGa_2$ values were not determined here.

Hall measurements can be combined with magnetoresistance measurements to give an estimate of $n_e + n_h$ and $\langle\omega_c\tau\rangle$ (equns. 16 and 17). For G3 <100>,

$$\frac{\rho_{xx}}{\rho_{zz}} = \frac{4.5\ \mu v}{3.0\ \mu v} = \left(\frac{n_h + n_e}{n_h - n_e}\right)^2 = \left(\frac{n_h + n_e}{.98}\right)^2$$

$$n_h + n_e = 1.22$$

$$\frac{\rho_{xy}}{\rho_{xx}} = 7.8 = \frac{n_h - n_e}{n_h + n_e} \cdot \omega_c\tau$$

$$\omega_c\tau = 9.5$$

From the NFE model, $n_h + n_e = .39 + 1.39 = 1.78$. The experimental approximation is probably too small; from dHvA data[13], we estimate that $n_e + n_h \sim 1.6$. A free-electron (F.E.) calculation of $\omega_c\langle\tau\rangle$, using the resistivity at 4.2^oK, predicts a value of 4.5. The experimental ω_c's are certainly as large as ω_c(F.E.), and thus the $\langle\tau\rangle$ obtained from ρ (4.2^oK, 0 kG) seems to be an underestimate. Similar analyses of two other crystals have been carried out with the results also listed in Table IX. We conclude that for <u>general</u> field directions our data for $AuAl_2$ and $AuGa_2$ and calculations based on it are in substantial agreement with the NFE model which predicts an effective carrier

Table IX. Hall data, general field directions.

	m	n_e-n_h	n_e+n_h	$\omega_c\tau$(calc.)	$\omega_c\tau$(exp.)
F.E.	0.00	7.00	7.00		
N.F.E.	0.00	1.00	1.78		
G3<100>	.20	.98	1.22	4.5	9.5
G3{100}	.51	1.13	1.26	2.8	5.2
	.42	1.25	1.49	2.8	4.4
	.74	1.01	1.88	2.8	3.5
A2(random)	.38	.81	1.32	4.6	6.5
	.89	1.15	2.90	4.6	3.0
	.50	.99	1.70	4.6	5.1
	.25	.95	1.38	4.6	6.0

concentration of 1 electron/primitive cell. Due to time limitations, we did not attempt measurements on the rather impure $AuIn_2$ for general field directions.

Symmetry Directions

Four symmetry directions are of interest to us; they are <211>, <110>, <111>, and <100>.[25] With the field parallel to <211>, Hall voltages in all three compounds were buried within .5 μv of peak-to-peak noise at 150 kG. A slight monotonic decrease with increasing field was noted. When this behavior is coupled with a saturating magnetoresistance, as it is here, we can state with some certainty that there are non-intersecting orbits open in the two directions <110> and <111> (Case 4., Table VIII). This is in agreement with the NFE model: on the fourth zone surface there are orbits open in <111> and <110>; in the third zone, there are orbits open in <111> only.

The behavior for B ll <110> is somewhat clearer now than it was in an earlier report[6], but by no means transparent. The Hall voltage is linear in B with a slope which depends critically on alignment with minima associated with <110> in $\Delta\rho/\rho$ vs. ψ curves. The magnetoresistance itself is a rapidly varying function near <110> with exponents ranging from .25 to 1.5 at the minima. We will later argue for open orbits when B ll <110> in agreement with the NFE model. The Hall behavior in all three compounds is consistent with the model also (Case 3, Table VIII).

Major discrepancies with the model occur when B is parallel to <111> and <100>. Figure 29 displays the Hall voltages in $AuIn_2$ for the NFE model. The experimental curves have been shifted vertically as in figure 28. The value of n_{100} = .68 means that there are .68 holes/per primitive cell compared to .372 on the NFE model. Electrons on the fourth zone sheet being replaced by holes must entirely account for this value if dHvA measurements of the third zone necks are correct in predicting a smaller area so that no Δn arises from this hole surface. For B ll <111> we see that V_H first swings positive and then crosses back at 60 kG. Further, the curve has been displaced more than its total voltage drop. The $\Delta\rho/\rho$ vs. B sweep here gives m = 1.08 at 150 kG. Thus the value n_{111} = +1.34 cannot be relied upon. The difficulty is caused by the low residual resistance ratio (75) of this sample. Table X contains all of the results including reliable values of n_{111} for $AuAl_2$ and $AuGa_2$.

The n_{111} values for $AuGa_2$ and $AuAl_2$ are less than 1.0 even with a 5% experimental error. We must conclude, then, that there are hole orbits on an electron sheet for this field direction in these compounds. Inspection of figure 9 reveals the sensible way for this to occur. If the NRC group[13] is correct in postulating that the fifth and sixth zone electron pockets have been emptied by the lattice potential, the remaining three zones must contain them. From figure 9 it is clear that the cut at p_z= 0.0

Figure 29 V_H vs. B in $AuIn_2$ for singular field directions.

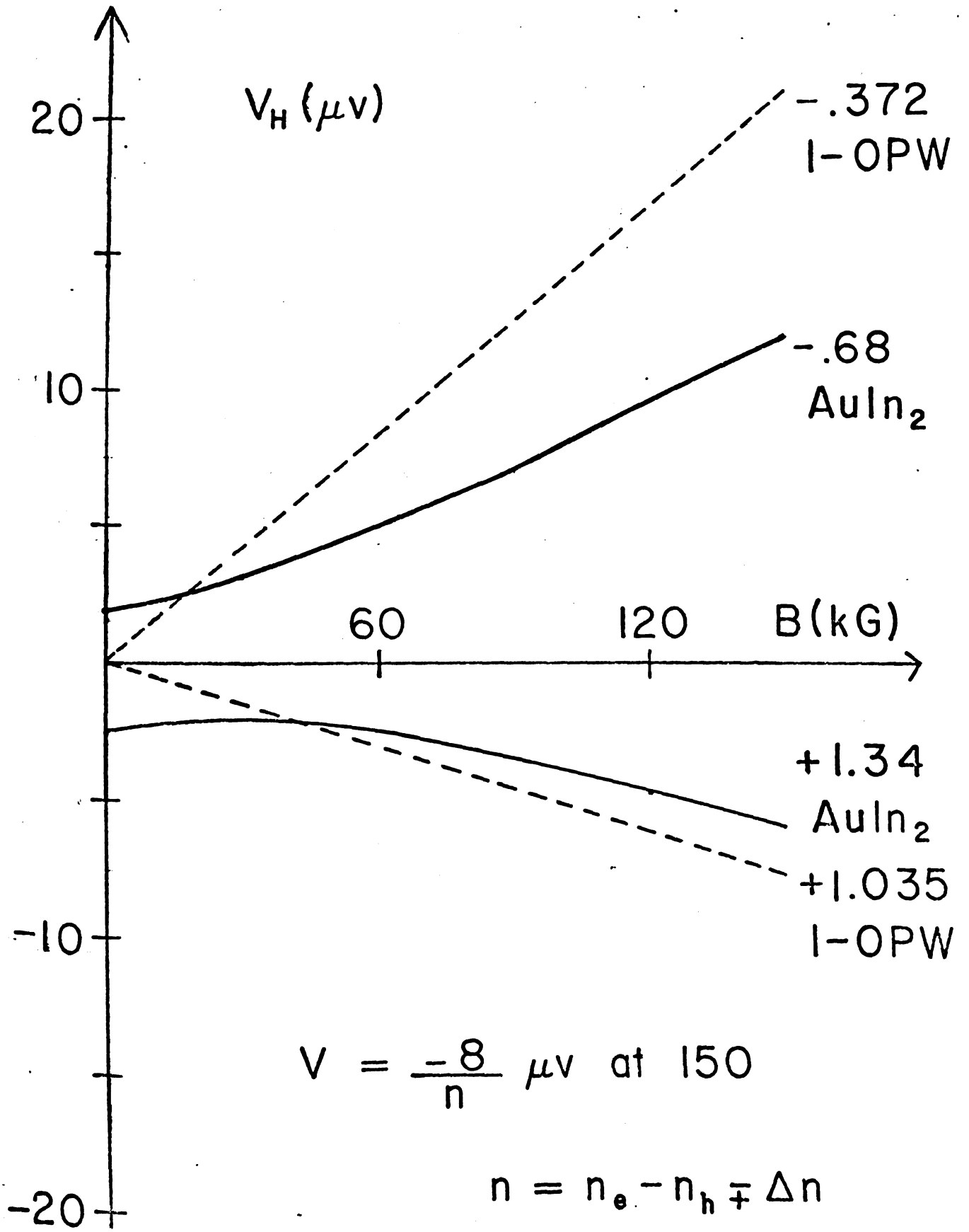
V_H (μv)
20
10
-10
-20
60
120
B(kG)
-.372
1-OPW
-.68
$AuIn_2$
+1.34
$AuIn_2$
+1.035
1-OPW
$V = \frac{-8}{n}$ μv at 150
$n = n_e - n_h \mp \Delta n$

Table X. Hall data, <100> and <111>; $n = n_e - n_h \mp \Delta n$.

	m	n_{100}	m	n_{111}
F.E.	0.0	7.00	0.0	7.00
N.F.E.	0.0	-.372	0.0	1.035
I2<110>	.57	-.68	1.08	(1.34)
G3{100}	.32	-.63		
G3<110>	0.0	-.62	.48	.89
G3<100>	.38	-.68	.50	.92
A1<100>	.43	-.79	.36	.57

produces electron orbits which are closer to contact than the orbits of any other section. Thus an excess of electrons in this zone could produce the required hole orbits. There is a catch, however; the NRC group has tentatively assigned a dHvA frequency to these very electron orbits in $AuAl_2$, called C_4 in figure 6. They point out that this frequency should continuously join on to the frequency they have postulated for B_4 as the field is swept towards <110> in the $\{110\}$ plane. In fact, both frequencies are restricted to 5° intervals from these major symmetry axes. The reason for the restricted angular range near <111> appears obvious from our Hall data; their frequency corresponds to the area of the hole orbit, which will clearly vanish for some angle of deviation from <111>. Unfortunately, the sign of the effective mass of $m^*(C_4)$ is not known. Note that there are two types of hole orbits; the one centered at Γ is extremal while the other, centered at the corners of the hexagonal unit cell, is not.

The easiest way to make quantitative checks of this postulate is to increase the radius of the Fermi sphere until the desired n_{111} is reached and then calculate the area and angular extent of the orbit by running the Harrison construction program in the usual manner. We can only hope for an estimate with this method since the NFE fifth and sixth zone electrons are almost certainly preferentially located in the ravines near the sharp tips of C_4. This "corner rounding" occurs because in general the

periodic potential of the crystal lattice acts to reduce the exposed area of the Fermi surface.[16] Thus the <100> arms probably are more cylinder-like than appears to be the case in figure 6. The results of the calculation are given in Table XI. The models which were fit to give the experimental n_{111} are in better agreement with dHvA and n_{100} results than the NFE model. The A_4 results are noticeably bad but we expect this as a result of "corner-rounding".

There is one possibility of salvaging the NFE model and that is to postulate magnetic breakdown of electron orbits like C_4 to form the hole orbits observed. Several experimental facts discredit this postulate. We would expect $AuGa_2$ to be most easily broken down from the arguments in section 1, but our n_{100} and n_{111} values indicate the opposite occurrence. A much simpler explanation is that $AuGa_2$ is more nearly free-electron-like than $AuAl_2$ and that both breakdown fields are greater than 150 kG.

If breakdown is occurring, we can set an upper limit on the field at which breakdown will be complete. In $AuAl_2$ our Hall curves give values of $n_{111} = .57$ and $n_{100} = -.79$ within 5% for B > 50 kG. For our best $AuGa_2$ crystal, a 5% tolerance is maintained down to 25 kG, while for the poorest crystal, V_H vs. B is linear to one part in 20 above 40 kG. We can demonstrate that breakdown is not complete at 25 - 50 kG if we assume that a simple breakdown model has validity here.

Table XI Calculations based on a model with a Fermi sphere fit to give experimental n_{111} values. NFE radius = 1.495, fit $AuGa_2$ radius = 1.532, fit $AuAl_2$ radius = 1.552. As usual $2\pi\hbar/a = 1$. There are hole orbits until z = .013 in the $AuGa_2$ model and z = .062 in $AuAl_2$; see figure 9. Data in parentheses is from early results of a study soon to be published by P.A. Schroeder, M. Springford, and J. T. Longo.

	Hall Effect		dHvA		"fit models"		NFE
	$AuAl_2$	$AuGa_2$	$AuAl_2$	$AuGa_2$	$AuAl_2$	$AuGa_2$	
n_{111}	.57	.91			.57	.91	1.035
n_{100}	-.79	-.64			-.84	-.72	-.372
<111> extremal area			1.7		~1.4	~1.5	1.4 = C_4
range of <111> orbit towards <110>			~5°	(~10°)	~10°	~5°	45°
B_4			1.15	(1.05)	~1.2	~1.09	.75
A_4			.62	.60	~.81	~.77	.62
A_4'			1.2	(1.0)	~.92	~1.05	1.2

The probability of transition between two orbits coupled by magnetic breakdown is given by[31]

$$P = e^{-B_o/B}$$

where

$$B_o = K\Delta^2 \, mc/\epsilon_F e\hbar \quad , \quad K \approx 1$$

Δ is the gap separating two energy bands. Our data indicates that $B_o \ll 50$ kG or $B_o \gg 150$ kG when the field is parallel to <111> or <100>. Assume $B_o = 10$ kG (250 kG) then with $\epsilon_F = 9.4$ ev, $\Delta \sim .1$ ev (.5 ev). Now we make a rough estimate of Δ and B_o from the dHvA results by noting from figure 9 that C_4 must breakdown via C_3 to give the experimentally observed area for the hole orbit. We construct a simplified two-dimensional model (figure 30) in which C_4 is represented by an electron overlap into the second zone, and C_3 by first zone holes. Then we have

$$m^* = \frac{1}{2\pi} \frac{\delta A_p}{\delta E} \quad , \quad \Delta \sim 2\delta E$$

In $AuAl_2$ $m^*(C_4) = 1.5\ m_e$, the area of the NFE $C_4 = 1.7(2\pi\hbar/a)^2$, and the measured area $= 1.4(2\pi\hbar/a)^2$. Therefore

$$\Delta_2 \sim \frac{2\ (1.7 - 1.4)\ \left(\frac{2\pi\hbar}{a}\right)^2}{2\pi\ (1.5\ m_e)} = .6 \text{ ev}$$

$$B_o \sim 360 \text{ kG}$$

Similarly, with $m^*(C_3) = .58\ m_e$, a measured C_3 area of $.6\ (2\pi\hbar/a)^2$ and a NFE area of $.65\ (2\pi\hbar/a)^2$, we obtain

$$\Delta_1 = .26 \text{ ev} \quad , \quad B_o \sim 68 \text{ kG}$$

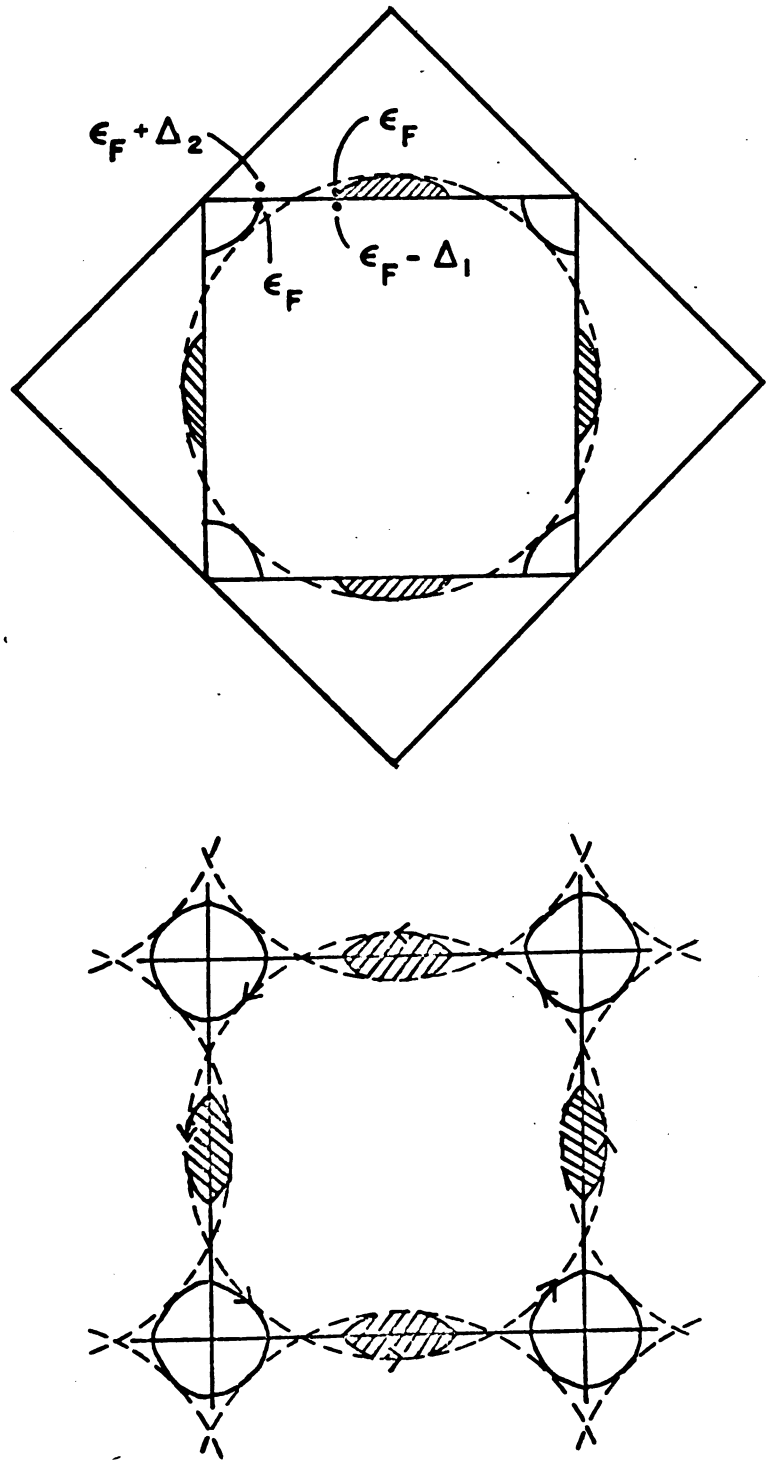

Figure 30 Simple model for the magnetic breakdown of orbits C_4.

Evidence that this estimated breakdown field of 68kG is too low is given by the normal behavior of the magnetoresistance vs. B curve which does not have the predicted anomaly at a field $\approx B_o/2$.[32]

We conclude that our Hall measurements along <100> and <111> give strong support to a fourth zone electron sheet which has hole orbits for B || <111> caused by the contact of orbits C_4.

The High-Field Magnetoresistance of AuX_2

The {100} Plane

Figure 31 displays the magnetoresistance of all three compounds in the {100} plane. Calculations of $\omega_c\tau$ for Al<100> and G3{100} give values near 5 (Table IX) so that the curves for these compounds can be compared directly to the calculated curve of figure 21. The agreement is good considering the assumptions about the relaxation time and the shapes of the surfaces that went into the calculation. Actually, the $AuGa_2$ curve should be multiplied by the factor $1/\cos^2\alpha = 1.16$ because $\underline{J}$ is 22° from <100> in G3{100}. This improves the fit slightly. The fact that there is no dip in the experimental curves at $\psi \approx 18^o$ suggests that hole orbits persist on the real fourth zone surface for several degrees beyond the 18° range on the log-pile model. Figure 20 shows why: σ_{xy}(closed), σ_{xx}(closed), and σ_{xx}(total) will then be larger at 18°, while $|\sigma_{xy}(\text{total})|$ will be smaller. Hence

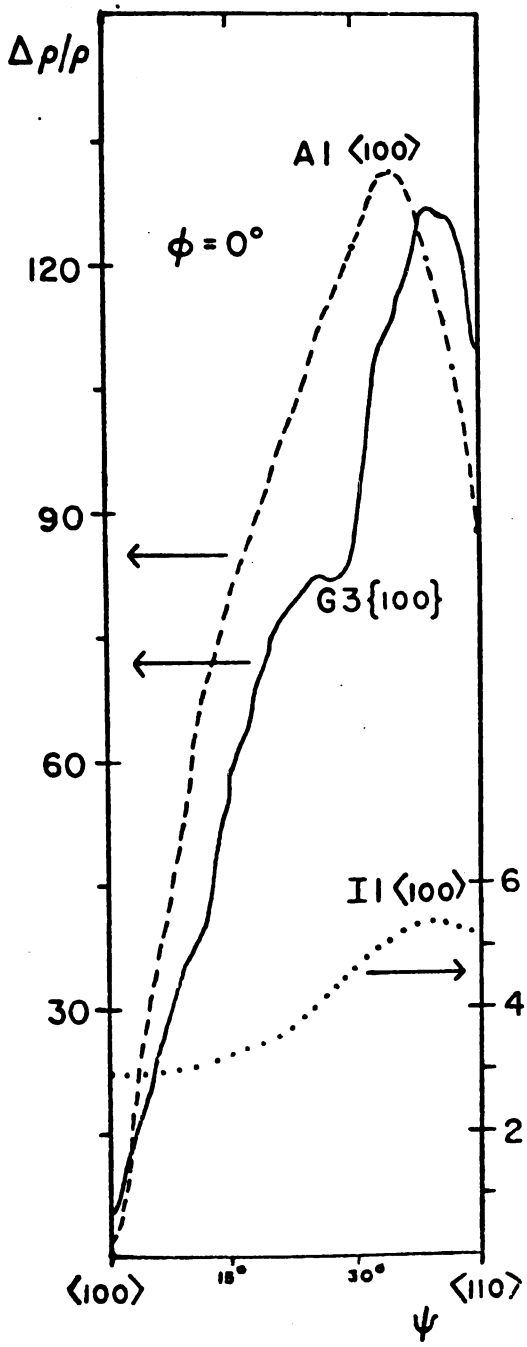

Figure 31 Δρ/ρ vs. ψ for all three compounds in {100} B = 140 kG

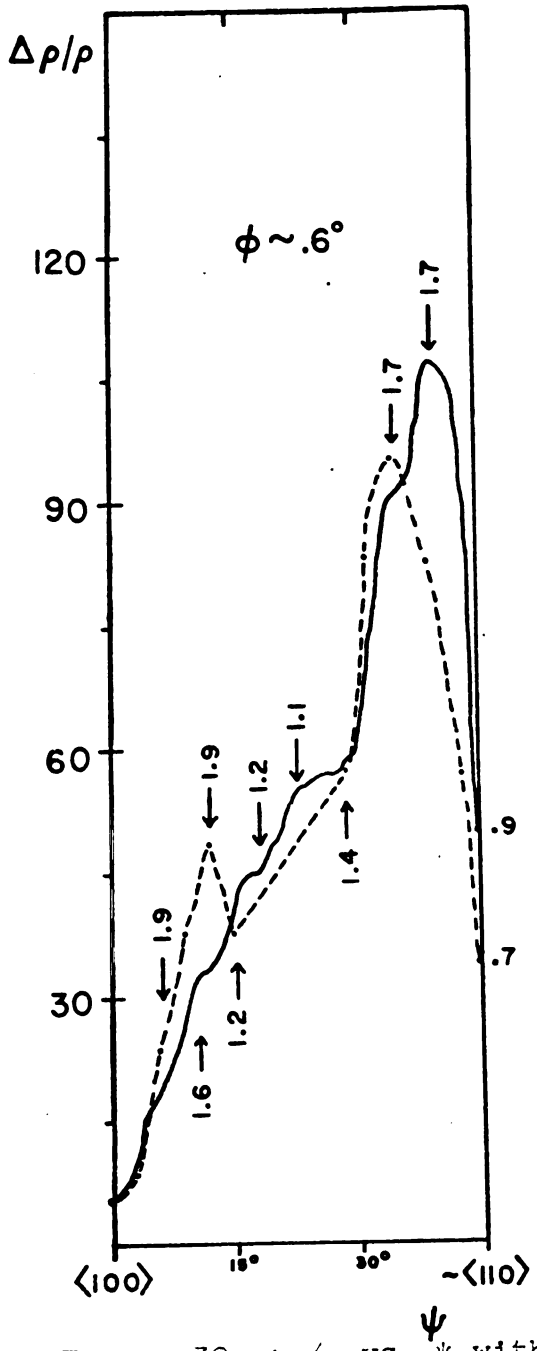

Figure 32 Δρ/ρ vs. ψ with φ changed by .6° from fig. 31. B = 140 kG

$\rho_{xx} \sim 1/\sigma_{xx}$, unlike the model, resulting in a monotonic increase in the magnetoresistance. This suggestion seems reasonable because the arms of the log-pile model do have a smaller cross sectional area than the measured value A_4 through the symmetry point W. [13] No pertinent dHvA data is available to aid in affirming this suggestion.

We estimate that $\underline{B}$ does not deviate from $\{100\}$ by more than $.5^{\circ}$ in the $AuAl_2$ and $AuGa_2$ curves of figure 31. We arrive at this estimate from the fact that a <u>change</u> of φ in figure 25 by $\pm .6^{\circ}$ produced curves similar to those of figure 32. (Values of m are given). Unfortunately, measurements of m were not made for the rotations of figure 31. Nevertheless, we know from the field dependence of the magnetoresistance at peaks observed in $\Delta\rho/\rho$ vs. ψ curves for other crystals that the entire $\{100\}$ plane supports open orbits except for $\underline{B} \parallel \langle 100 \rangle$ and $\langle 110 \rangle$. The $\langle 100 \rangle$ axis is singular. The magnetoresistance at $\langle 110 \rangle$ was determined to be "quadratic", m = 1.5 at 115 kG, by rotational measurements on Al$\langle 111 \rangle$ at three different fields. See figure 33. The very large magnetoresistance observed in figure 31 indicates that $\Delta\rho/\rho$ is probably quadratic at $\langle 110 \rangle$ in $AuGa_2$ also. We attribute the sharp drop in magnetoresistance near $\langle 110 \rangle$ in figure 32 to the $\cos^2\alpha$ term of Table VIII, $\alpha = 90^{\circ}$. Figure 35 provides an illustration of this effect.

Two-Dimensional Regions in $AuAl_2$ and $AuGa_2$

The region between 15° and 30° in figure 32 is begin-

Figure 33 $\Delta\rho/\rho$ vs. ψ in $\{111\}$ for $AuAl_2$ at 83.1, 99.8, and 129.9 kG. The exponents computed from these graphs for B || <110> are m = 1.7 at 91.5 kG and m = 1.5 at 115 kG.

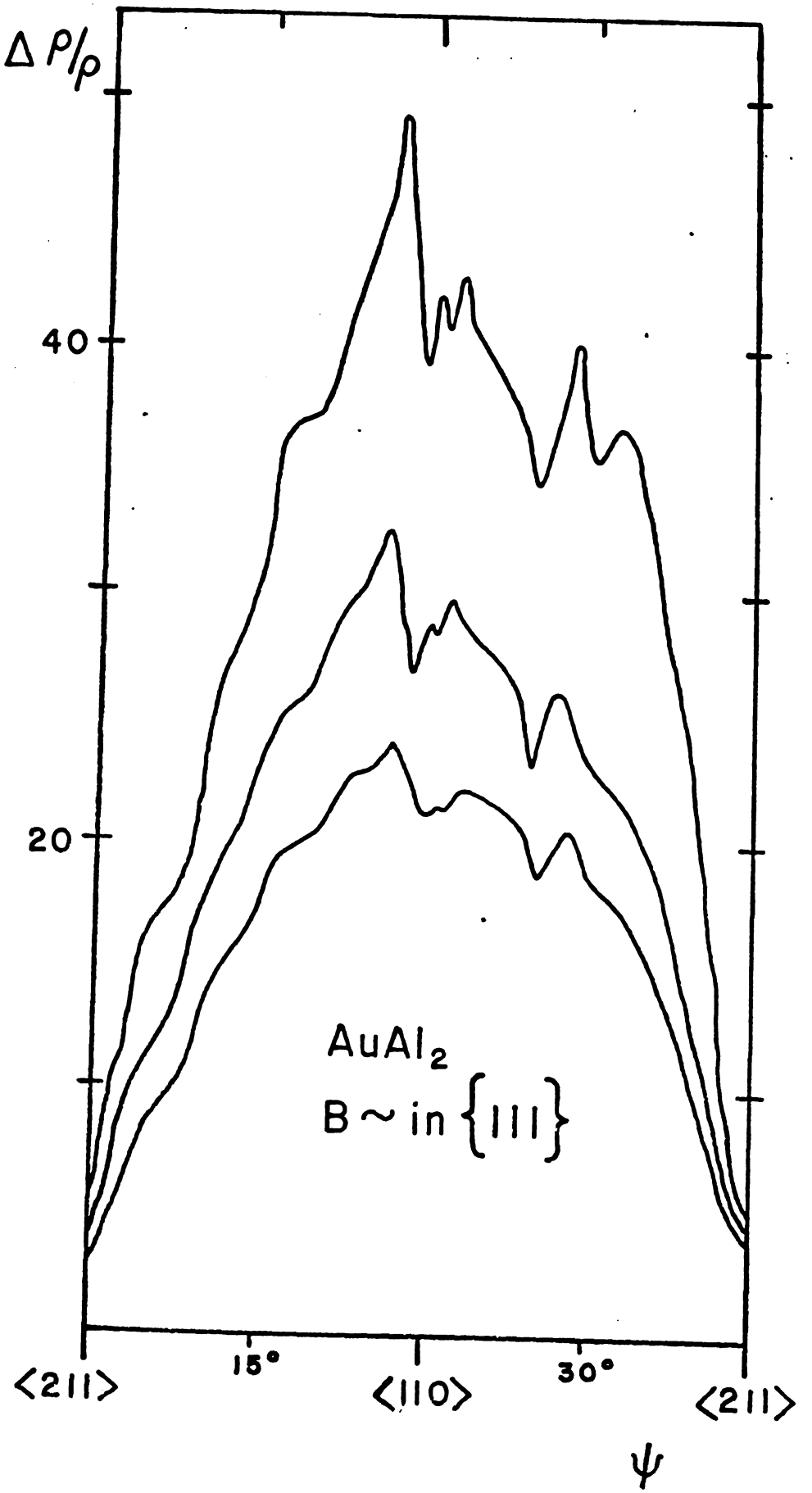

Figure 33

ning to saturate because the orbits here are most likely not open but extended. By tipping φ to several angles and performing rotations at two different fields, a systematic exploration of field directions supporting open orbits can be carried out. We begin with a presentation of the results of such an analysis on Al<100> and G3<100>. We will also follow this with a discussion of our results on several other crystals.

Figure 34 displays the magnetoresistance of Al<100> and G3<100> along the paths indicated in the stereograms of figures 35 and 36. In the latter figures we use the symbol of an open circle to represent "saturation", i.e., $\Delta\rho/\rho = B^m$, $m < .7$; and we use a solid line or dot to represent the extent of "quadratic" field dependence, $m > 1.5$. Intermediate or unknown values of m are not marked. Shaded areas of all stereograms represent probable regions of open orbits primarily as determined by data on one crystal. If information on a certain section of a stereogram is not available from this data, we have supplied this information from results on other crystals. The similarity of the two curves of figure 34 is as remarkable as their disagreement with the NFE model which predicts a B^2 dependence along the entire rotation path. A summary of the results of several similar rotations is given in figures 35 and 36. The behavior predicted by the NFE model in the fourth zone (figure 37) is not seen experimentally. Open orbits from the third zone of the NFE model could give a qualitative explanation of the

Figure 34 $\Delta\rho/\rho$ vs. ψ for Al<100> and G3<100> along paths indicated in the stereograms of figures 35 and 36. B = 145 kG.

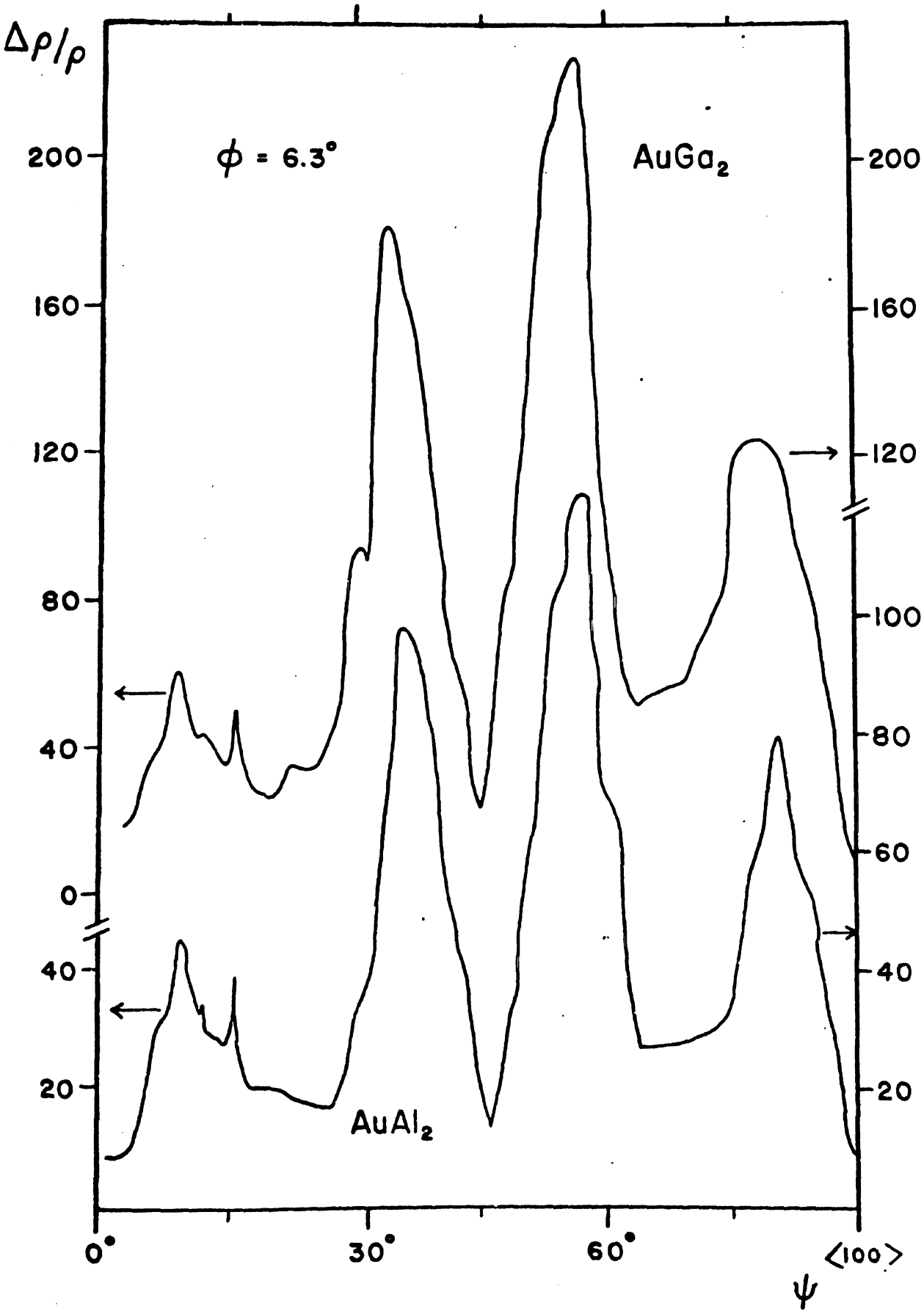
Δρ/ρ
φ = 6.3°
AuGa₂
AuAl₂
200
160
120
80
40
0
40
20
200
160
120
100
80
60
40
20
0°
30°
60°
<100>
ψ

Figure 34

Figure 35 Magnetoresistance stereogram for Al<100>. Bars and dots indicate $m > 1.5$; open circles mean $m < .7$.

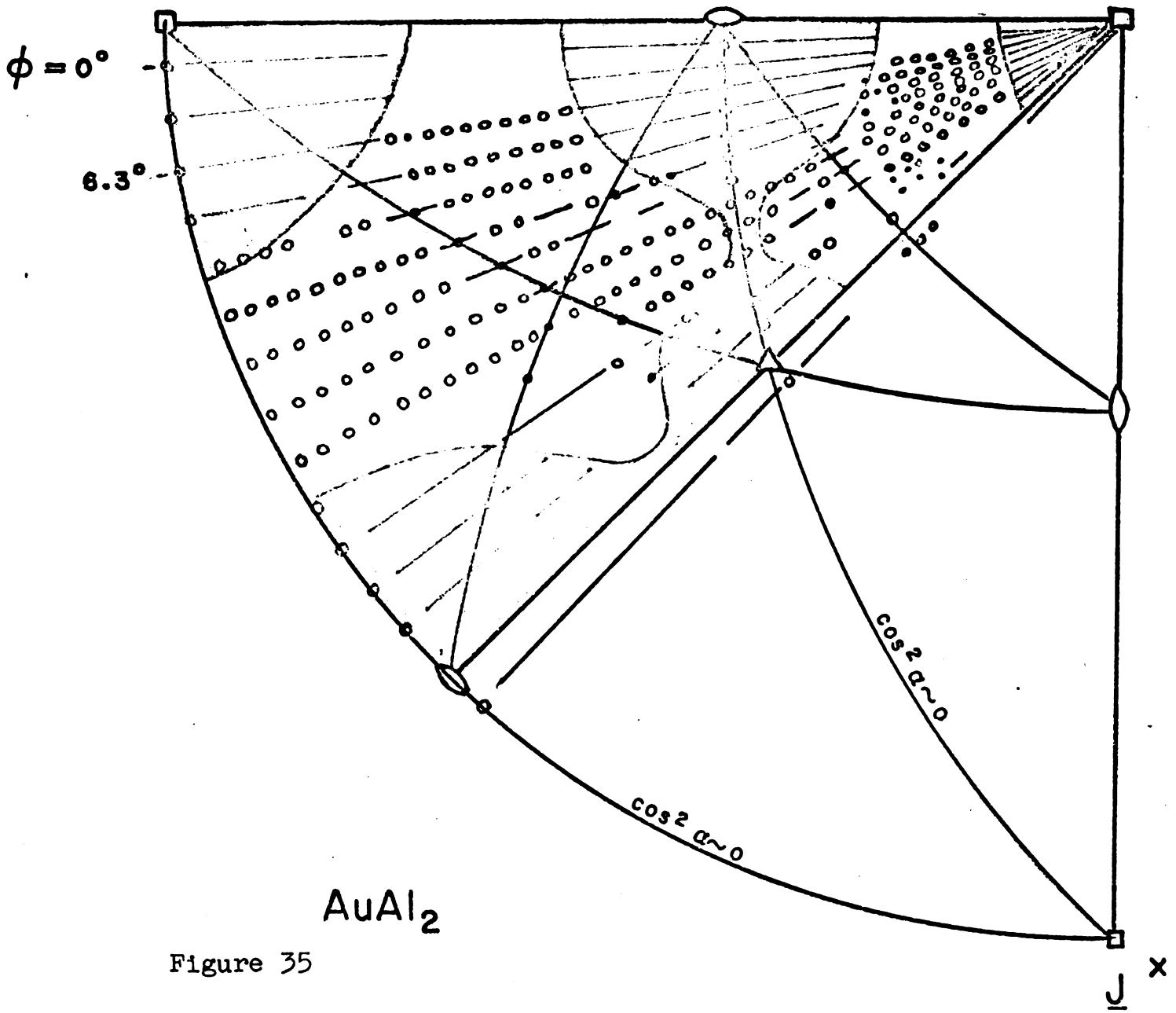

$AuAl_2$

Figure 35

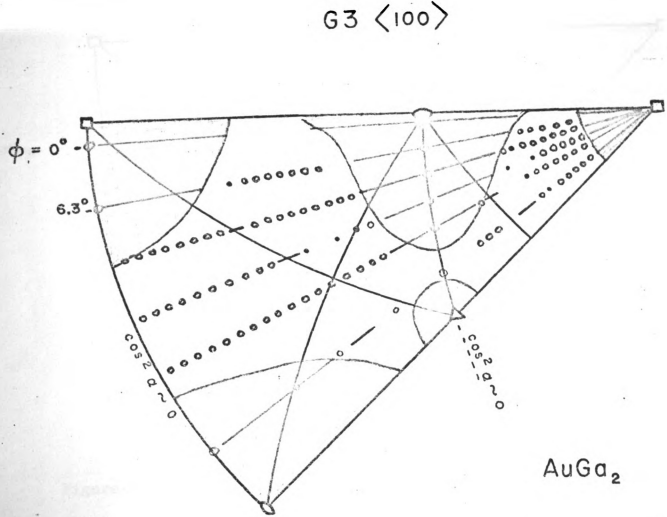

Figure 36 Magnetoresistance stereogram for G3<100>.

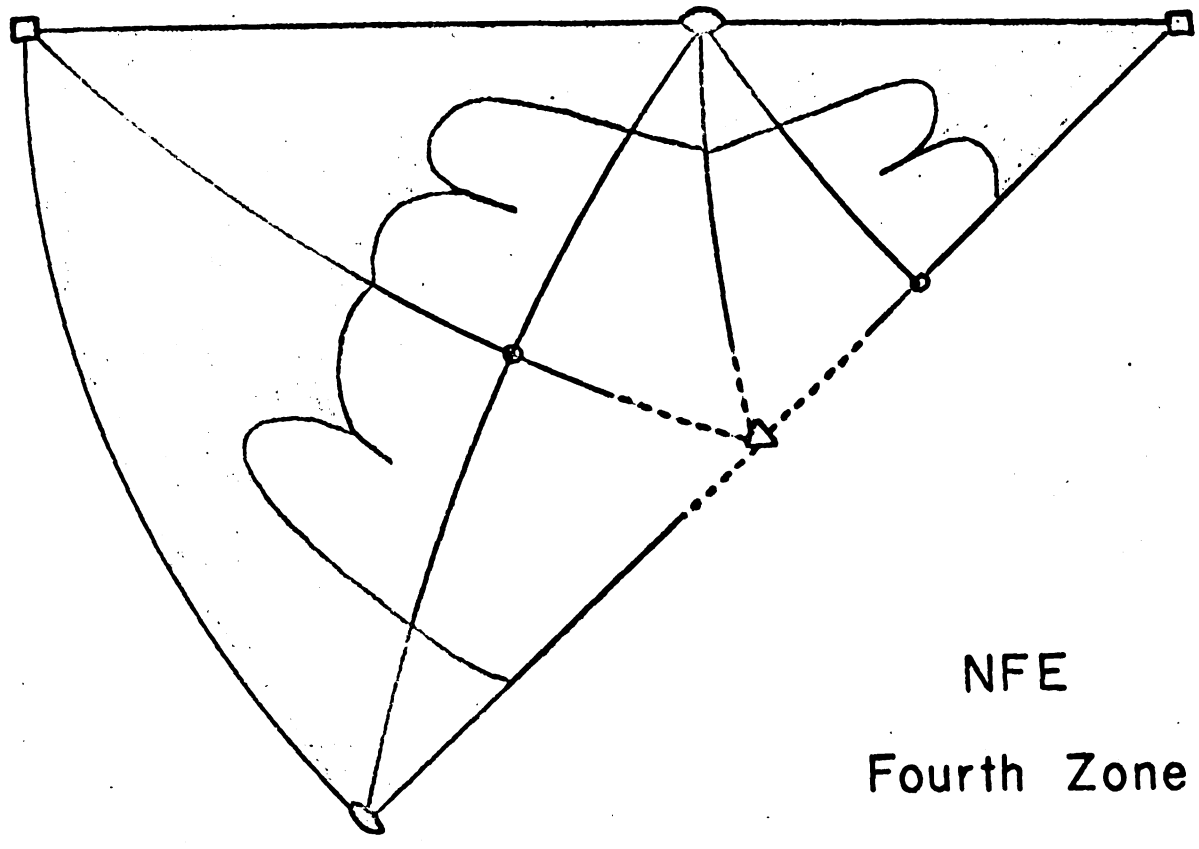

Figure 37 Magnetoresistance stereogram for NFE model in fourth zone.

<110> two-dimensional region in $AuGa_2$. However the restriction of the neck size observed in dHvA almost certainly eliminates this possibility: calculations of the extent of this region with a Fermi radius increased $\lesssim$ 5 per cent to give the dHvA area of the third zone neck show that open orbits exist only within 10° of <110> in $AuGa_2$ and 5° in $AuAl_2$.

We have a considerable amount of supplementary data on $AuGa_2$. Figure 38 is the result of a rotation of G3{100} along an arc of the great circle indicated in figure 39. Seven other rotations yielded the remaining data on this crystal with the results symbolized in figure 39. Note that m assumes more intermediate values here than it did for G3<100>, a better crystal. The saturation observed inside the suggested <110> two-dimensional region results from the $\cos^2\alpha$ = 0 arc being shifted from the {110} plane since $\underline{J}$ is 22° from <100>.

Our best data relevant to the directions of $\underline{B}$ supporting open orbits in $AuGa_2$ comes from G3<110>. We observed extremely sharp structure in rotations, e.g., figure 40 and only a minority of the measurements of m gave equivocal results. (See figure 41) The analysis of nine pairs of $\Delta\rho/\rho$ vs. ψ curves at fields of 125.0 and 144.7 kG resulted in figure 42. Most of the dots represent higher-order open orbits which are "excited" as the field crosses low symmetry planes. A complete analysis of the extent of these "whiskers" from the major symmetry directions has been carried out

Figure 38 $\Delta\rho/\rho$ vs. ψ for G3{100} along path indicated in figure 39 at fields of 130 and 140 kG.

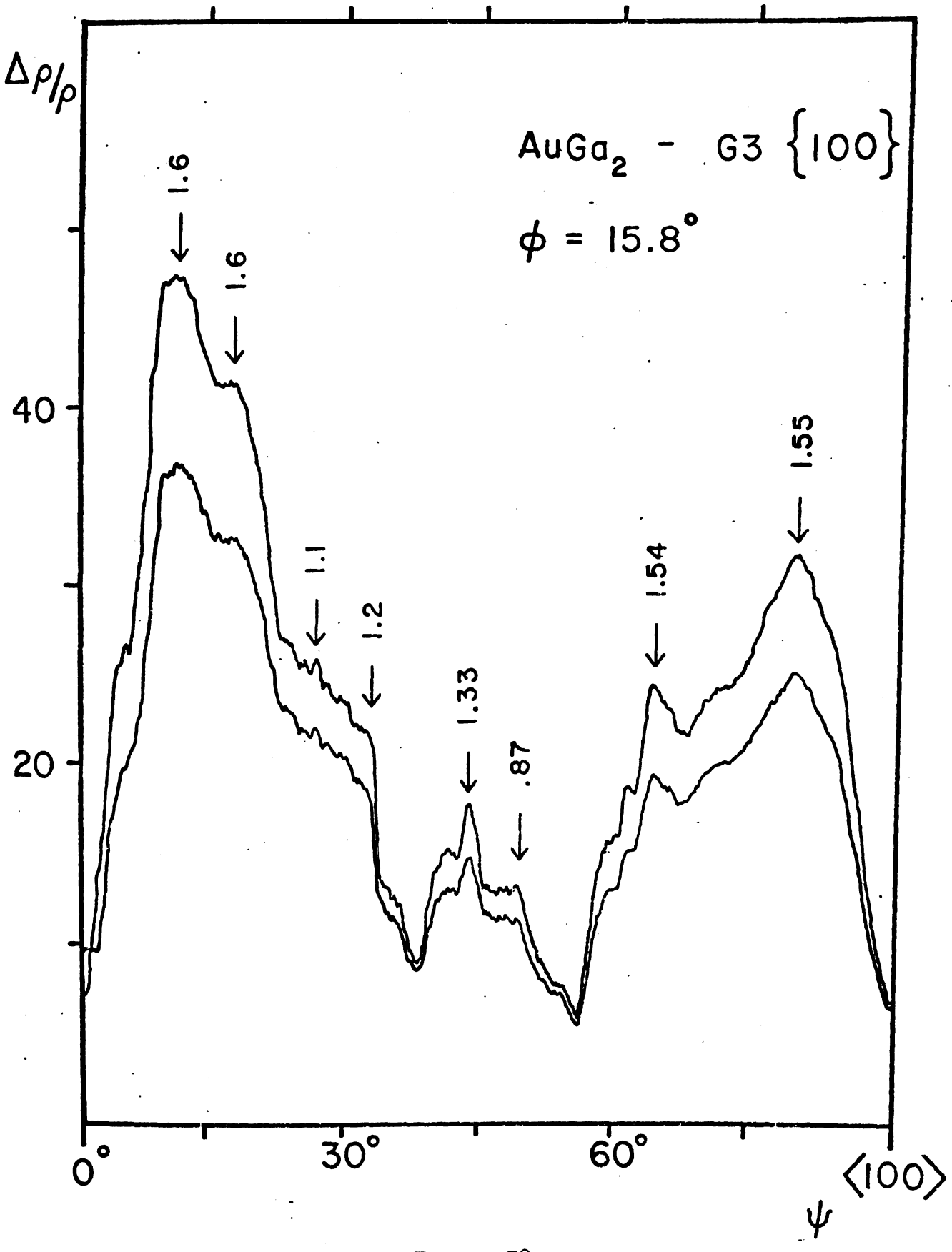

Figure 38

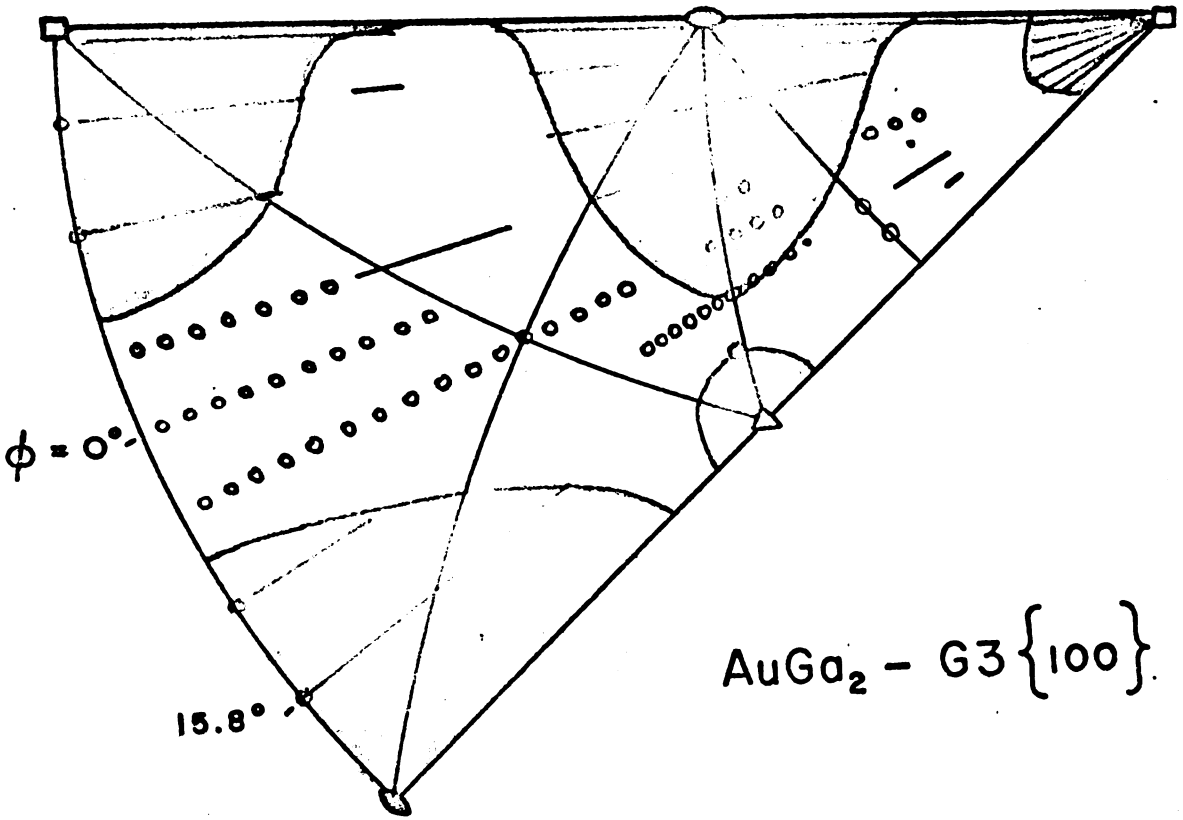

Figure 39 Magnetoresistance stereogram for G3{100} .

Figure 40 $\Delta\rho/\rho$ vs. ψ for G3<110> along path indicated in figure 42.

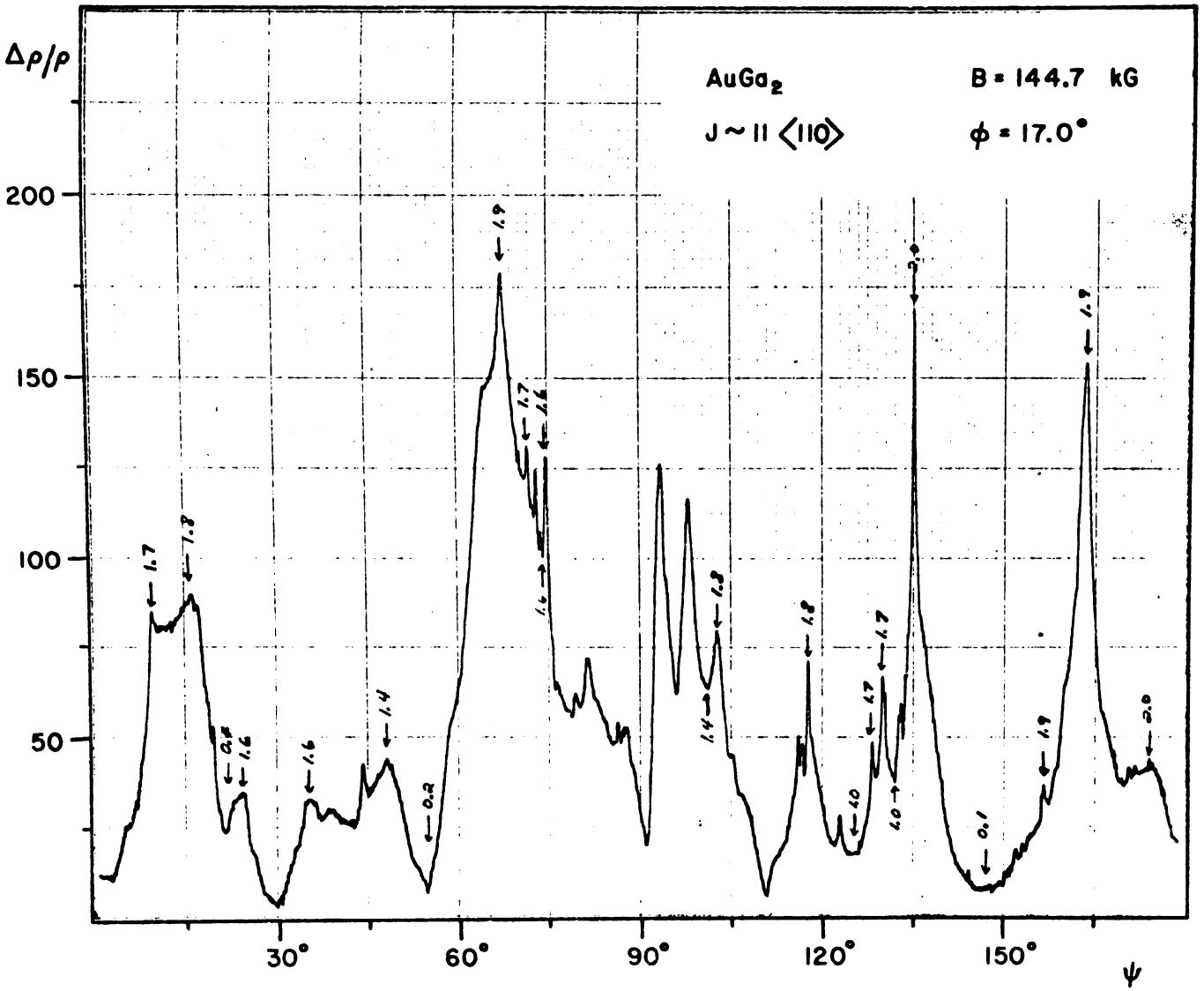

Figure 40

Figure 41 $\Delta\rho/\rho$ vs. B for $\underline{B}$ oriented along three crystallographic directions in G3<100>. m = 0.0, 0.2, 1.8 .

Figure 41

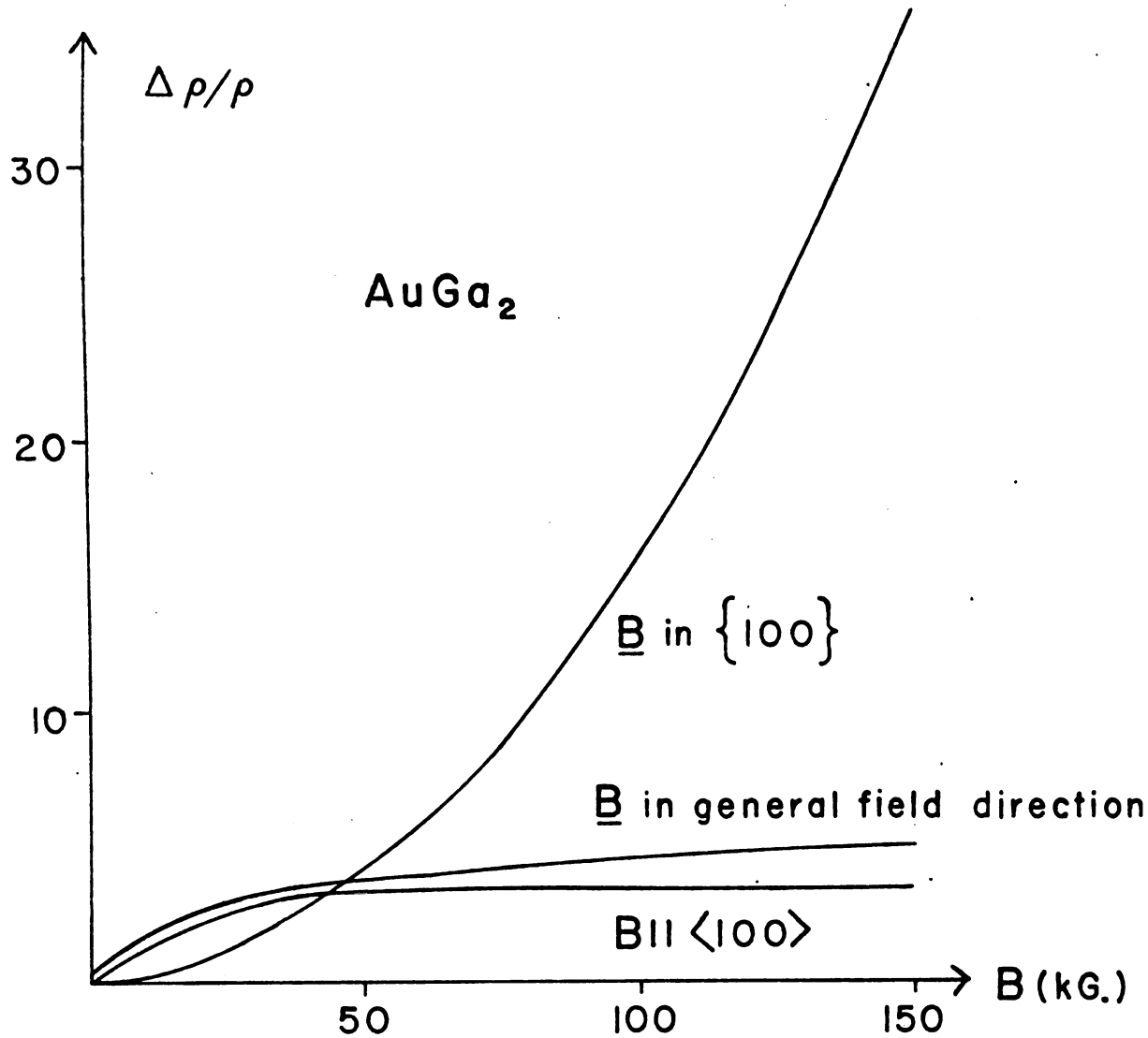
Δρ/ρ
30
20
10
AuGa2
B in {100}
B in general field direction
B∥⟨100⟩
50
100
150
B (kG.)

Figure 42 Magnetoresistance stereogram for G3<110>.

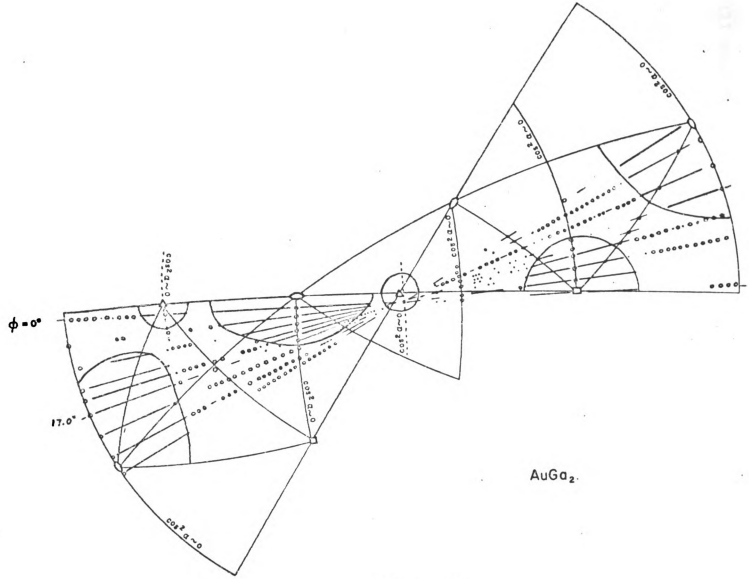

Figure 42

based on information from another set of runs on this same crystal with φ at the more favorable values near 90°. We will conclude this section with those results.

In 1966 several rotations at one field were performed on Al<100> and Al<111> with the <110> axis parallel to BB' of figure 25. We cannot make any definitive statements about B^2 regions of the stereogram from this data but experience has shown that, usually, saturation is associated with low, slowly varying parts of the curves and quadratic behavior with sharp peaks and the highest parts of the curves. Thus we can interpret these curves in a qualitative fashion. Consider figure 43. In the upper trace, we speculate that $\Delta\rho/\rho$ is quadratic from 35° to 65° except at the minima where m takes on an intermediate value. From the lower curve, we guess that the two-dimensional region about <111> extends out approximately 10°, while the region about <110> measures 15° when the field is in the plane $\{211\}$. Figure 44 shows that these predictions, which were made before the 1967 runs, generally conform with the established results taken from figure 35.

Figure 45 is a rotation of Al<111> along the same path as the upper curve of figure 43 to within 2°. The difference in the shape of the two curves is explained by the term $\cos^2\alpha$. The peak at 18° in figure 45 is missing in figure 43 because the angle between the open orbit direction [010] and the current direction [100] is 90°. A similar analysis explains the difference in the relative height of other B^2

Figure 43 $\Delta\rho/\rho$ vs. ψ for Al<100> along paths indicated in figure 44. B = 130 kG.

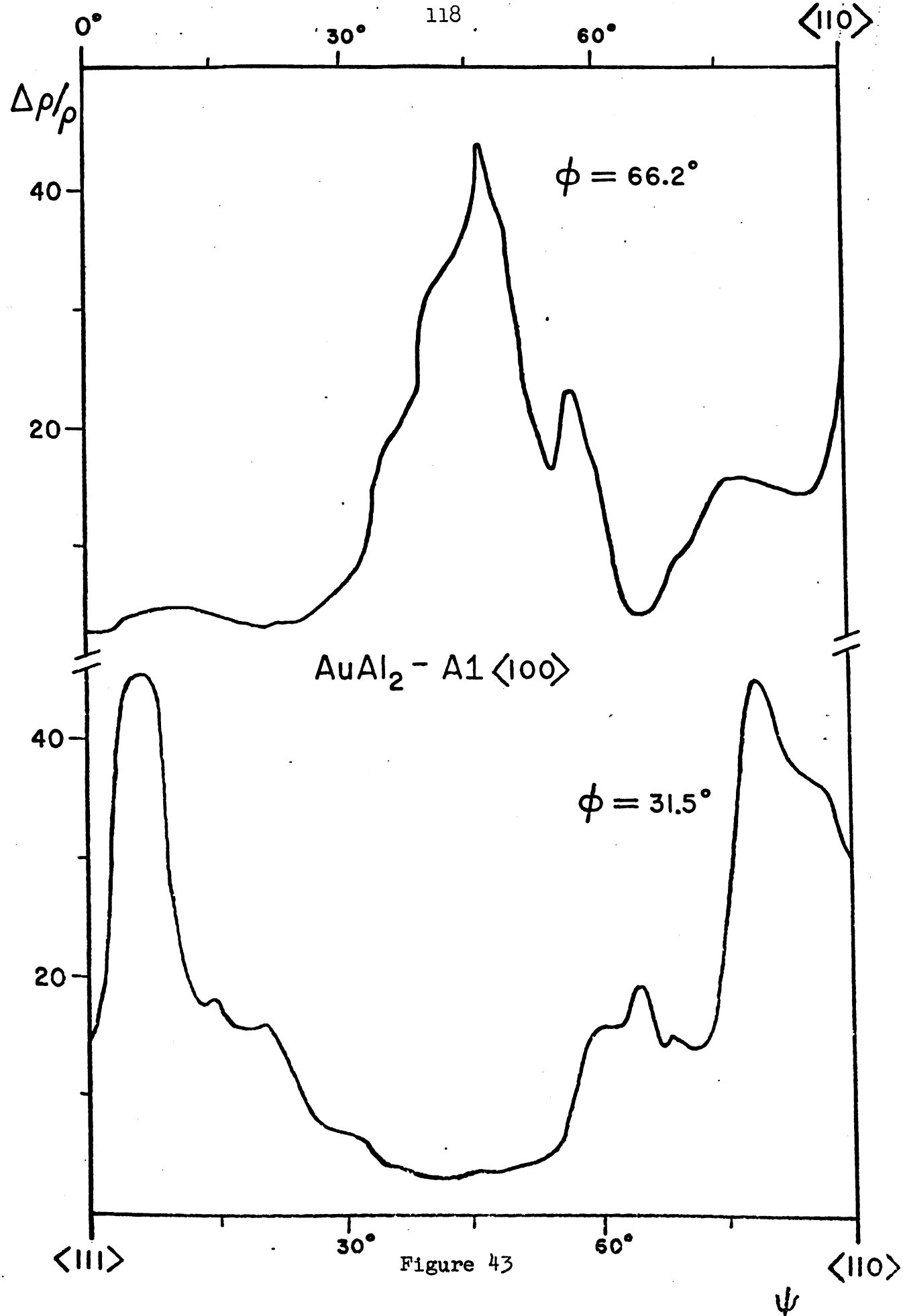

Figure 43

Figure 44 Magnetoresistance stereogram for Al<100>. Shaded areas depicting two-dimensional regions were determined from figure 35.

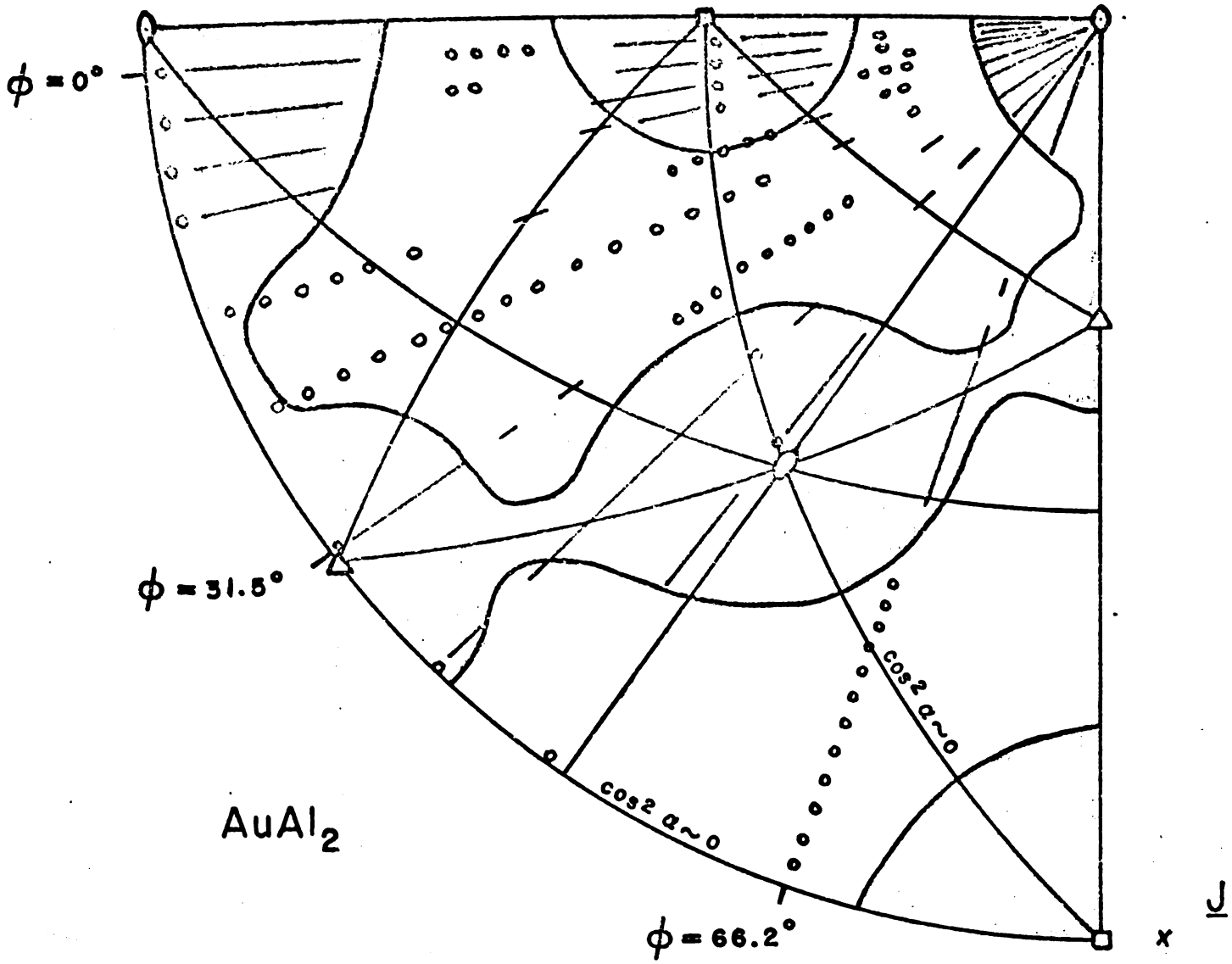

Figure 44

Figure 45 $\Delta\rho/\rho$ vs. ψ for Al<111>. B = 130 kG.

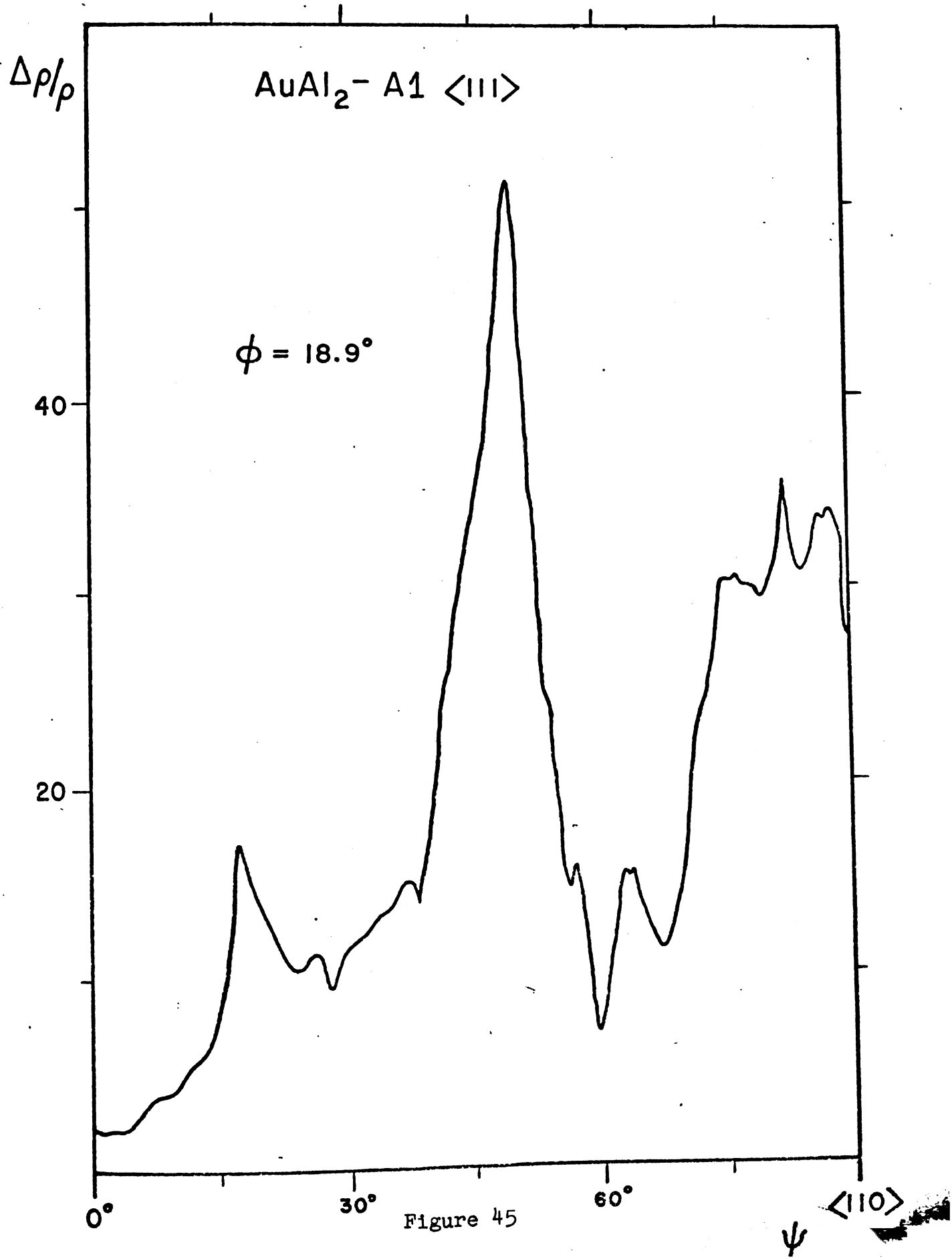

Figure 45

regions.

In all of the experimental stereograms, we have shown unexplained B^2 regions near the axis <211>. Some of these are close to, or in, the planes {210} and {211} and could be attributed to one-dimensional regions of open orbits. Others are not in high symmetry planes and evade explanation unless there is a two-dimensional region of open orbits surrounding <211>. <211> is not surrounded by aperiodic open orbits on the NFE model.

Our data indicates that the <100> and <110> two-dimensional regions are not connected along {100} unless this region is very narrow, i.e., less than $.6^{\circ}$ (see figure 32 and the discussion concerning it on page 96). Our data indicates that the <110> and <111> open orbit regions are probably connected in $AuAl_2$ but not in $AuGa_2$. However, there are some minor discrepancies. Figure 46 is a rotation of A2 (random) in which B is known to be 2 2 degrees outside of {110} at the heads of the arrows depicting the region of quadratic behavior. The upper limit of 4° on the connecting area is in disagreement with figures 43 and 45. Here we must appeal to the questionability of our interpretation of those figures and to the fact that there could be a 2° error in the knowledge of the field in figures 43 and 45 also. Figure 47 is a rotation of G3<110> very close to the {110} plane. At 12° and 63° we know that B is 2° 1° from {110}. The rather large magnetoresistance seen here (values of m are unknown) suggests that the orbits are open

Figure 46 $\Delta\rho/\rho$ vs. ψ for A2(random). B = 130, 145 kG.

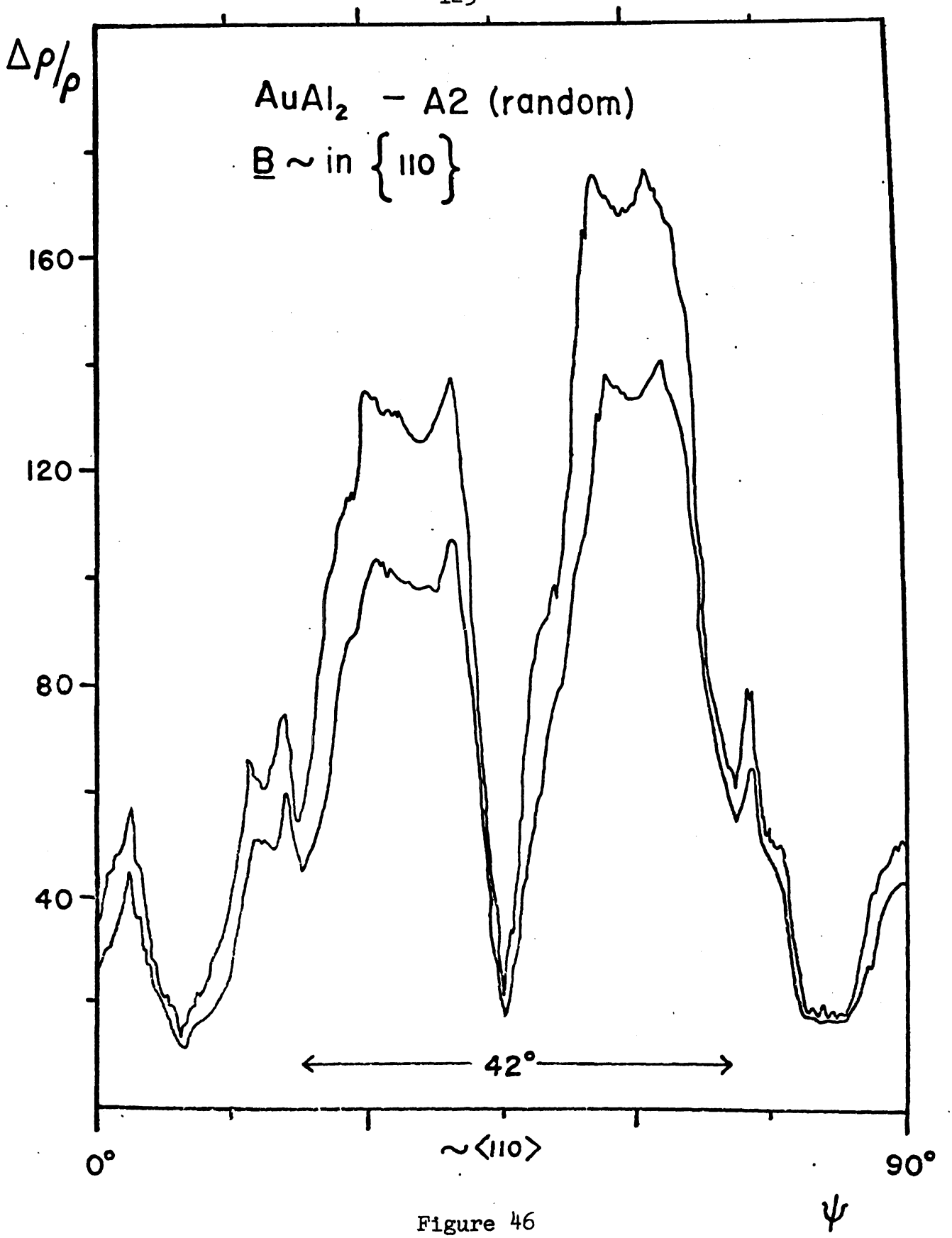

Figure 46

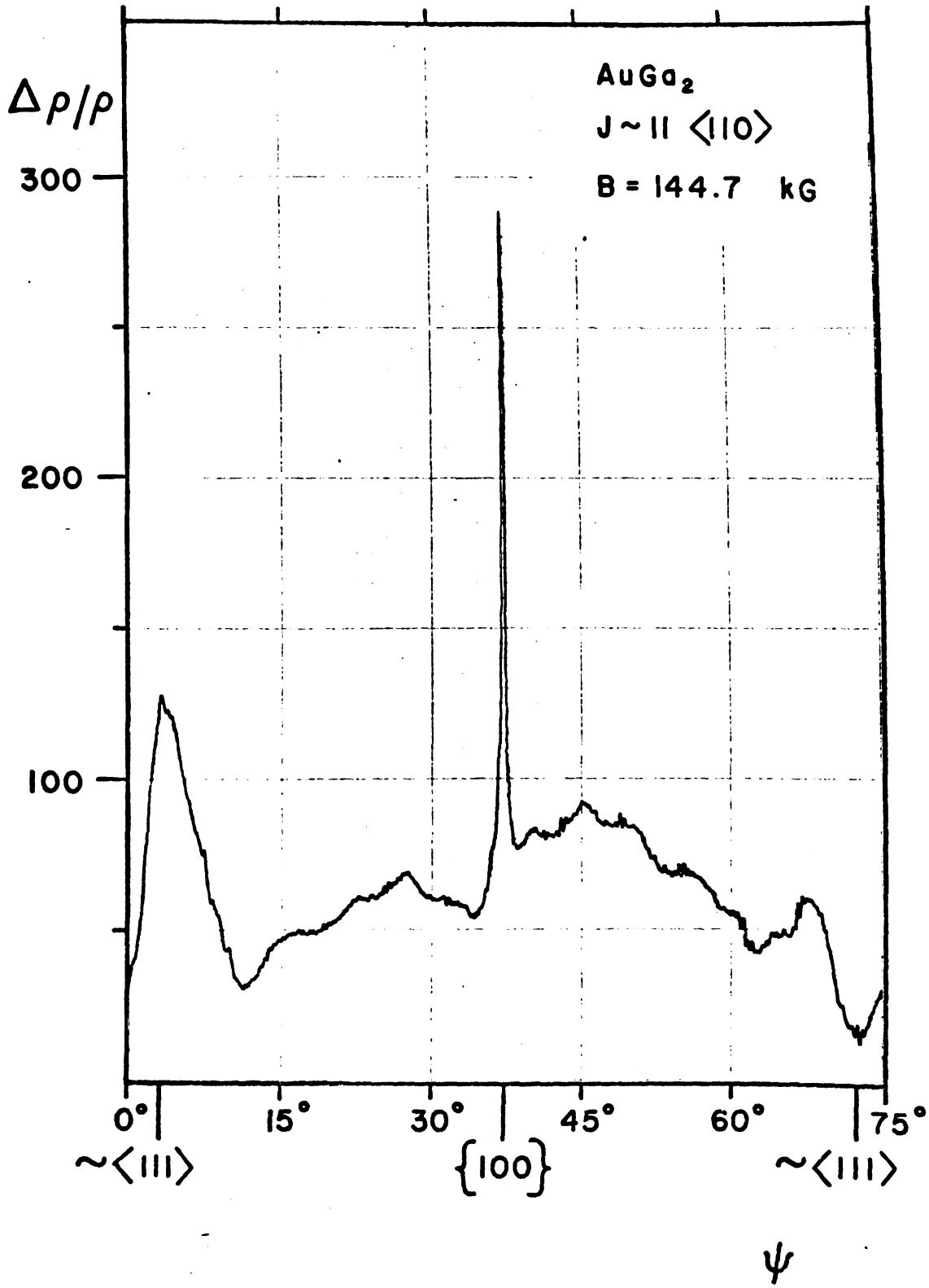

Figure 47. Δρ/ρ vs. ψ for GB<110>.

in disagreement with our other results. The fact that these points are minima, however, leaves open the possibility that these orbits are merely extended.

"Whiskers" in $AuGa_2$

The sharpness of the {100} peak in figure 47 indicates that carriers on <100> directed open orbits in G3<110> are rather far into the high-field region. (33) Using this crystal, which has the highest residual resistance ratio of any intermetallic compound on which data has been published, we easily resolved sixth and higher order open orbits in the magnetoresistance. The peaks on the left side of figure 48 are due to orbits open in directions <110>, <210>, <310>, <511>, <100>, <611>, <511>, <311>, <211>, <533>, <322>, <111>, <553>, <774>, <221>, <331>. The two-dimensional regions of open orbits which produce the broad peaks are centered on <111> and <110>. Note again the sharpness of the peak observed when $\underline{B}$ crosses {100} at about $\psi = 130^\circ$. Several similar rotations with φ varying between 60° and 90° produced figures 49 and 50. The lengths of the whiskers in these figures are determined by noting the disappearance of a peak as φ is changed. We demonstrate this in figure 51. At $\varphi = 72.1^\circ$ we are inside the <100> two-dimensional region until $\psi = 43^\circ$; the magnetoresistance is slowly varying because only the coefficient of B^2 is changing. When φ is changed to 75.3°, we skirt the edge of the two-dimensional region. For $\underline{B}$ in certain symmetry planes only, open orbits

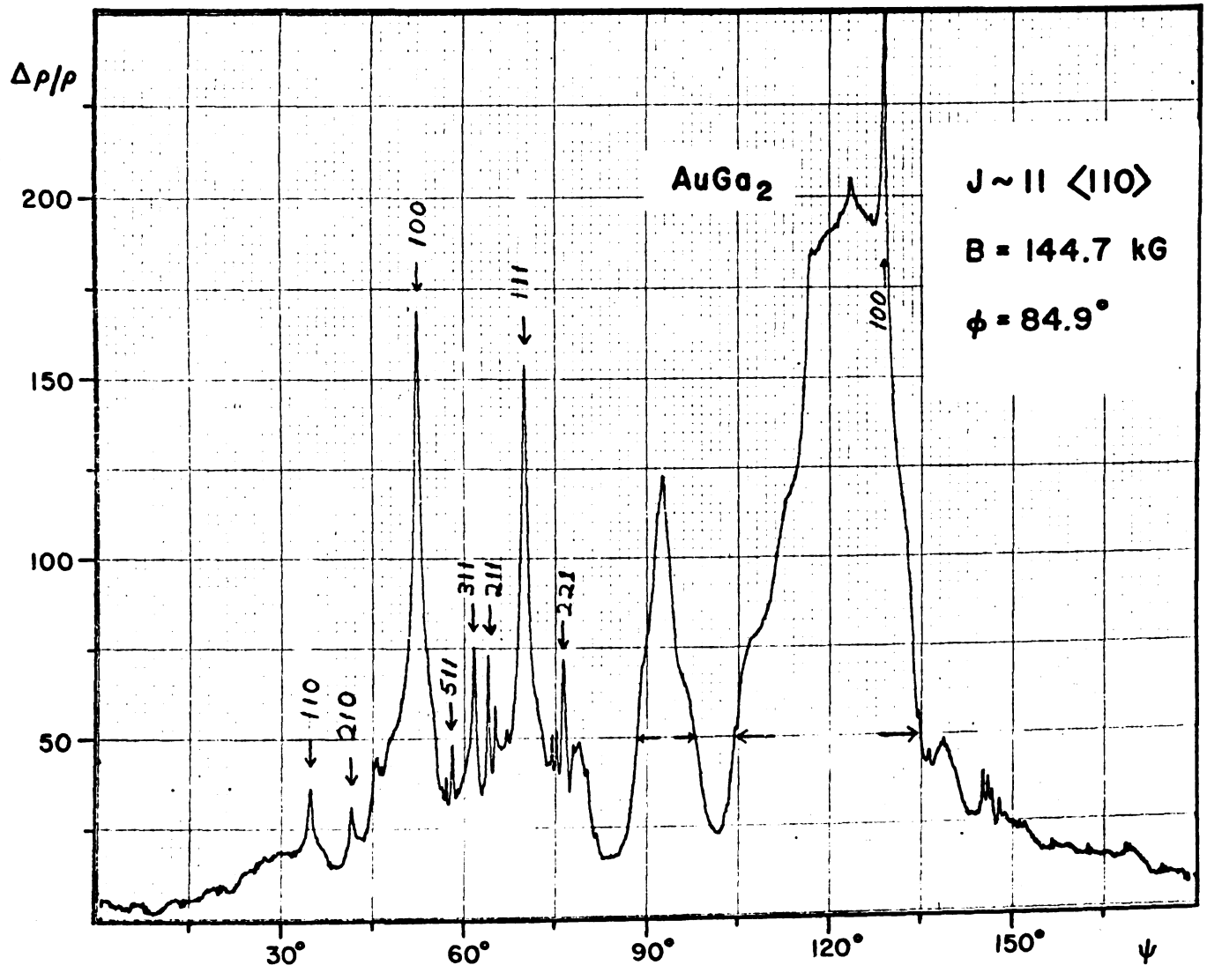

Figure 48 $\Delta\rho/\rho$ vs. ψ for G3<110>.

Figure 49 Magnetoresistance stereogram for G3<110>.

G3 ⟨110⟩

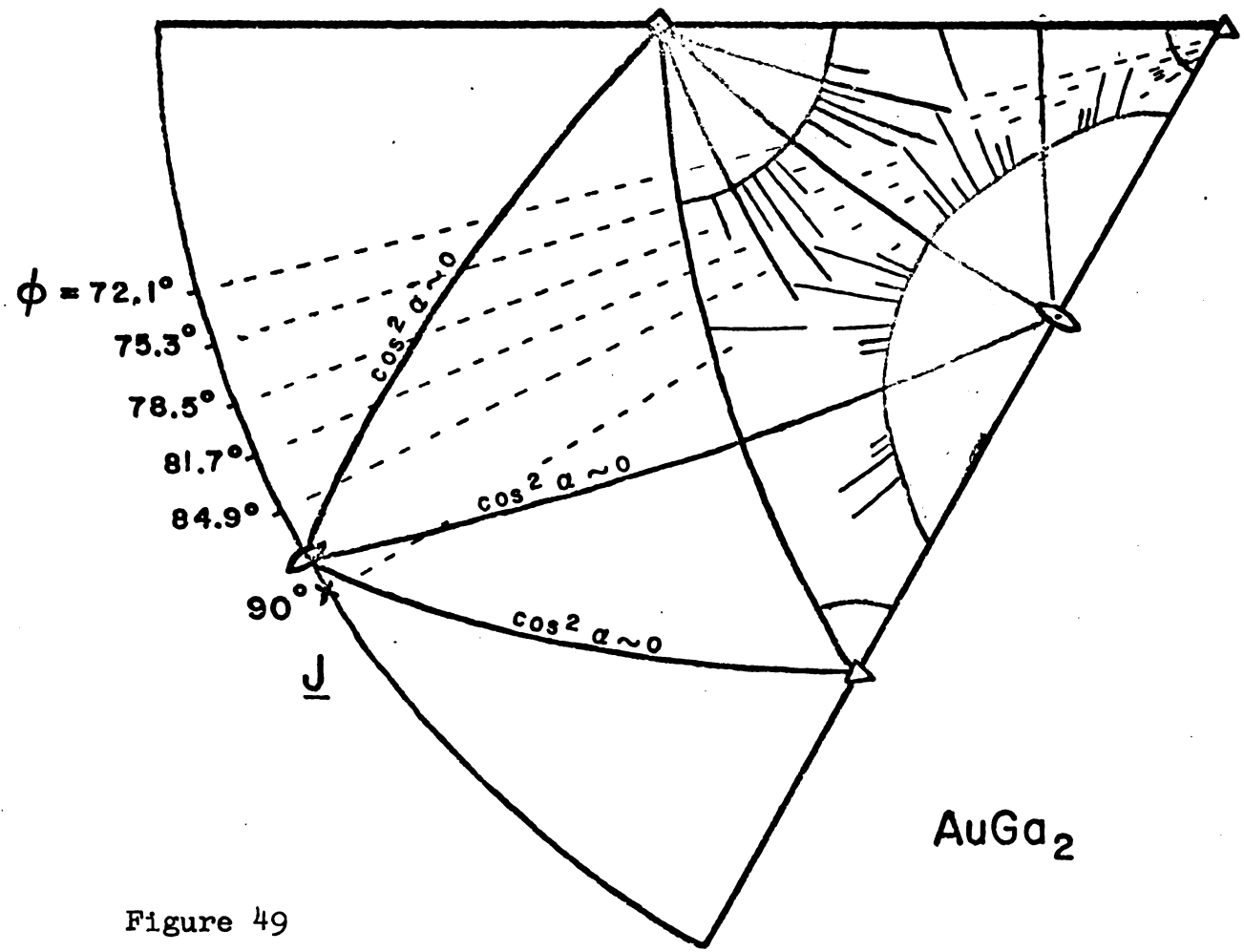

Figure 49

Figure 50 "Whiskers" and two-dimensional regions in $AuGa_2$.

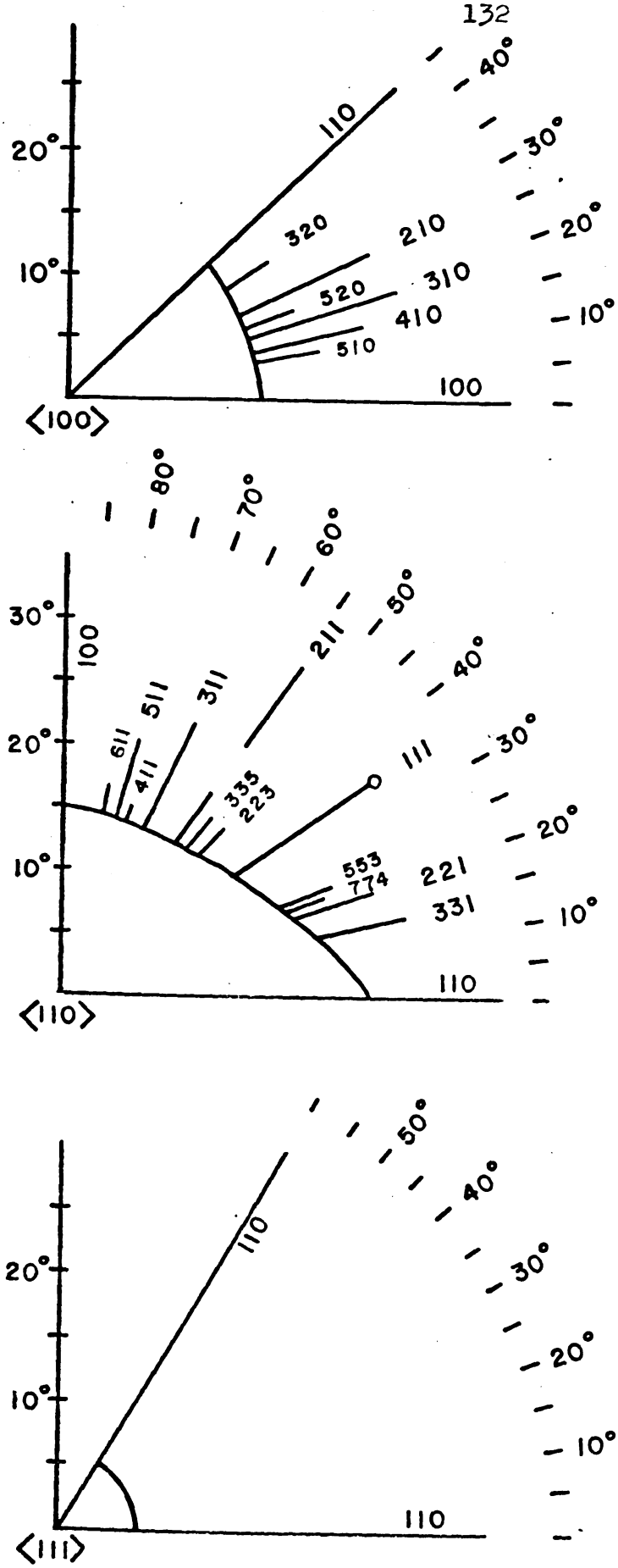

$AuGa_2$

Figure 50

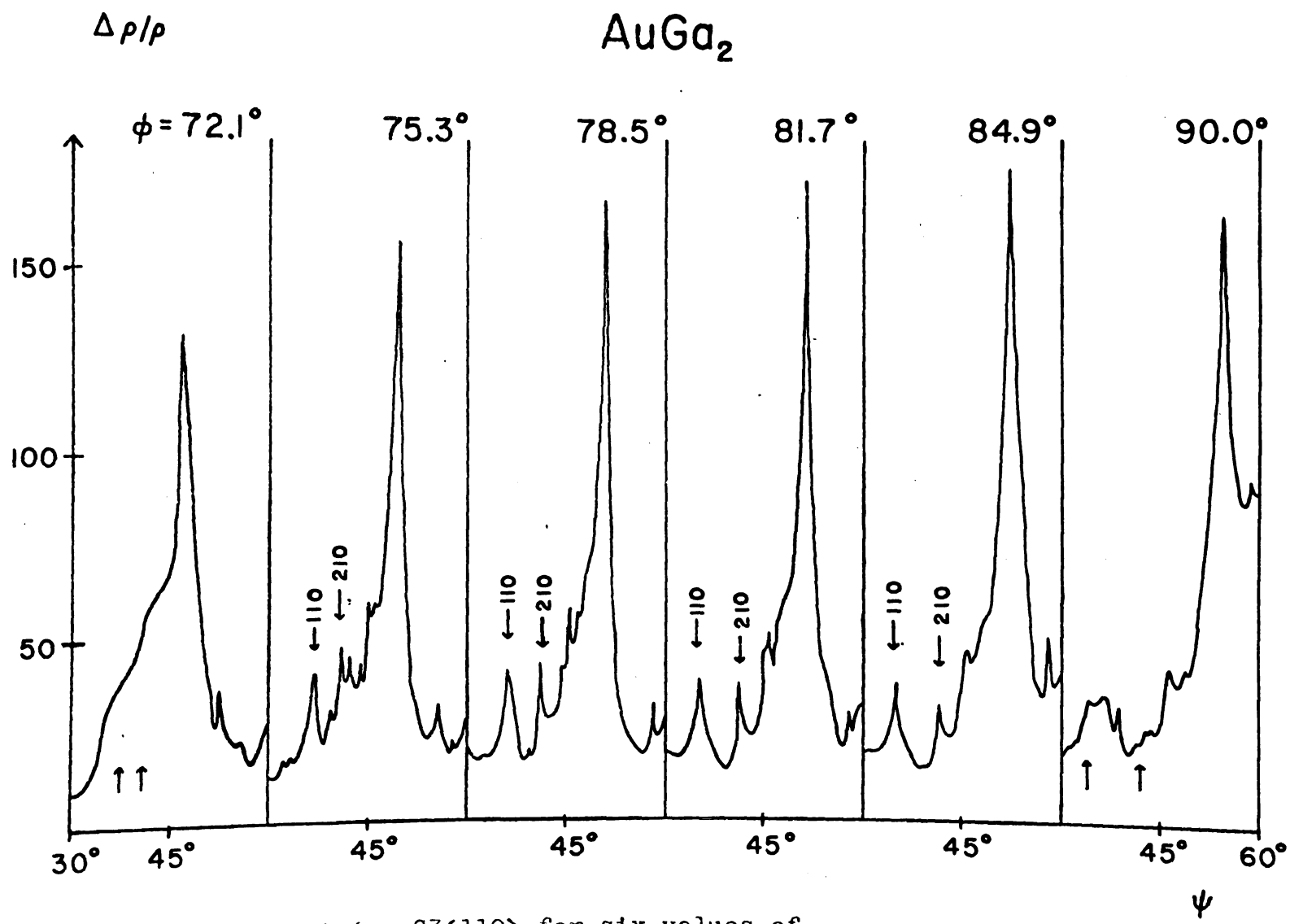

Figure 51 $\Delta\rho/\rho$ vs. ψ for G3<110> for six values of φ .

still exist; the magnetoresistance acquires structure because of the transition between saturating and quadratic behavior. At $\varphi = 81.7^{\circ}$ the "fuzz" due to very high order open orbits has disappeared. Finally, at $\varphi = 90^{\circ}$, the 210 whisker has ended and the peak due to the crossing of the $\{110\}$ plane has merged into a B^2 background near <211> on the stereogram.

The assignment of the 774 and 553 whiskers in figure 50 must be considered tentative since the planes $\{332\}$ and $\{443\}$ are within 1° of the position of $\underline{B}$ on the stereogram where the magnetoresistance peaks occur. However, the data is sharp enough that we estimate a maximum error of $\pm .5^{\circ}$ in ψ, which gives considerable weight to our assignment.

Table XII gives the order of the open orbits arising from <111> and <100> - directed necks according to the simple scheme used in section 2. (34) In copper the "whiskers" have a strength and extent that decreases with increasing order of the orbit. (25) From Table XII and figure 50, we see that if this property held for a complicated surface like that of the fourth zone of AuX_2, the whiskers extending out of the <110> axis must be partially derived from the third zone surface with its <111>-directed necks. We have already shown, however, that in the NFE model of the fourth zone the <111> open orbits exist for $\underline{B}$ anywhere in $\{111\}$ while the lower order <110> open orbits vanish for $\underline{B}$ near <111> in $\{110\}$. Thus the lengths of the whiskers in $AuGa_2$ may be explicable without appealing to

Table XII Higher order open orbits for Fermi surfaces with <100> or <111>-directed primary open orbits.

Order	Possible open orbit directions	
1	<100>	<111>
2	<110>	<100>, <110>
3	<111>, <210>	<311>, <331>
4	<211>, <310>	<210>, <211>, <221>
5	<311>, <221>, <410>, <320>	<511>, <531>, <551>, <533>, <553>
6	<411>, <321>, <510>	<310>, <320>, <321>, <322>, <332>

third zone open orbits.

Models

A comparison of any of the experimental stereograms in this section with the NFE stereograms of figures 18 and 37 shows that the NFE model does not explain our experimental results on the extent of two-dimensional regions about <100> and <110>. With a smaller third zone neck, it does not even predict the existence of one about <111>. Another point of disagreement concerns the extent of open orbits in the $\{110\}$ plane. In all three compounds the magnetoresistance in $\{110\}$ is quadratic unless the field is close to <211>. On the NFE model $\{110\}$ is not a one-dimensional region of open orbits near <111>.

As we pointed out at the beginning of this section, we must have an analytic model to obtain results we can compare in a quantitative way with experiment. The obvious choice is NFE models with radii swollen to give the n_{111} values since these models were successful in interpreting the Hall data at <100> and various dHvA areas. If the Hall effect and magnetoresistance data are consistent, these models should also yield two-dimensional regions of approximately correct dimensions. Because of the cost involved (~ twenty-five dollars per angle), we limited ourselves to four symmetry and ten non-symmetry directions of $\underline{B}$ for each model. On the NFE model only one of the non-symmetry directions of $\underline{B}$ gives the experimental result.

In figures 52a,b we summarize the analysis of general field directions and compare it with experimental results. Agreement is excellent for the $AuAl_2$ model: all ten field directions produce the type of orbit experiment found. In the $AuGa_2$ model four of the field directions give erroneous results and indicate that the <100> two-dimensional region is too large while that about <111> is too small. The $AuAl_2$ model actually gives a better fit to the $AuGa_2$ experimental results than the $AuGa_2$ model for the ten non-symmetry directions. The fact that the experimental two-dimensional region near <100> in $AuGa_2$ does not extend a few degrees beyond the range observed in $AuAl_2$ is somewhat surprising since the experimental Hall coefficient at <100>, as well as that obtained from the models, indicates that there are fewer holes on the electron sheet in $AuGa_2$ than there are in $AuAl_2$(Table XI). This is a minor but interesting point for which we have no explanation. The behavior of the $AuGa_2$ model near <111> and <110> is in better agreement with experimental data. Although the two dimensional region about <111> is too small, we must remember that the hole orbit layer is very thin on the model (less than five per cent of the height of the unit cell) and the tendency for electrons in excess of the NFE number is to deviate from rigid-band placement, resulting in corner-rounding. Thus, it would seem that a small change in the model near the hole orbit layer could produce the experimental angular extent of the aperiodic open orbits near <111>. Of great importance is the

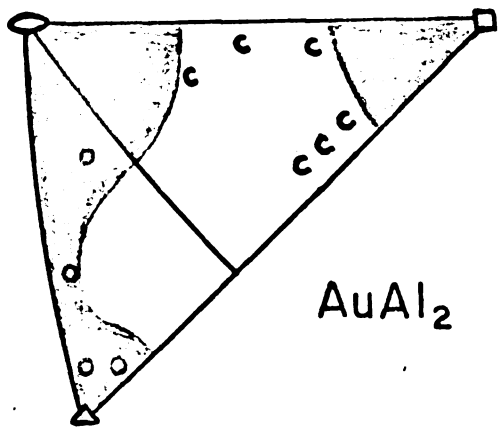

Figure 52 Magnetoresistance stereograms comparing experimental open orbit regions (shaded) with the type of orbits (c=closed, o=open) determined on the models.

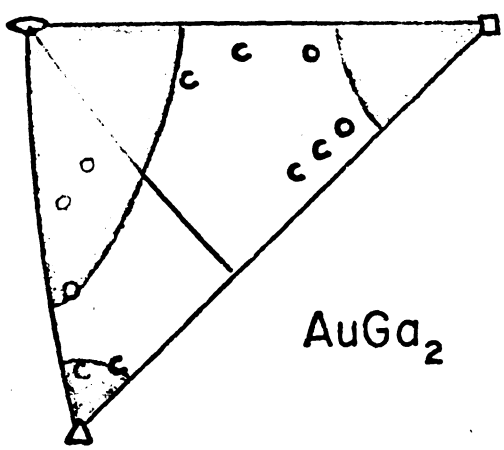

fact that the two-dimensional region about <111> on the $AuAl_2$ model is clearly larger than the region about this axis on the $AuGa_2$ model and furthermore that there is evidence that the <111> and <110> two-dimensional regions on the $AuAl_2$ model are connected, while on the $AuGa_2$ model they are not. These features are in agreement with experiment. Thus, with the field near <111>, our magnetoresistance data corroborates our interpretation of the Hall data, i.e., that the open surfaces of $AuGa_2$ may be more NFE-like than those of $AuAl_2$.

We find that there are extended closed hole orbits for general field directions on these models. This is in disagreement with our Hall data since $n_e - n_h = 0$ then. We take this as evidence that excess electrons do deviate from rigid-band placement.

The behavior of the models at <100> and <111> has already been described. Both models were fit to give the experimental n_{111} and then gave better values than the NFE model for the experimental n_{100}. With $\underline{B}$ || to <110>, the fourth zone open orbit layer has diminished in width, while the hole orbit layer has increased in width. This should result in an increase in the size of the two-dimensional region about <110> over the NFE value in agreement with experiment. At <211> there are still orbits open in two directions. Furthermore, on the $AuAl_2$ model, there is a small band of hole orbits on the electron sheet, which offers a possible explanation for the suspected aperiodic open orbits near this axis. No hole orbits were observed on the $AuGa_2$ model.

We were unable to measure the two-dimensional regions of open orbits in $AuIn_2$ due to the small relaxation times of our samples. An approximate B^2 dependence of the magnetoresistance was measured in $\{100\}$ and $\{110\}$. The magnetoresistance at <211> saturates, while at <110>, $m \sim 1.5$. Hall effect measurements at <100> indicate that the Fermi surface of $AuIn_2$ may be similar to that of $AuGa_2$.

We have presented experimental results on whiskers in $AuGa_2$ primarily for later researchers who might want to compare two analytic models of the Fermi surface which give good fits to the experimental two-dimensional regions. In such a case, the extent of the whiskers can aid in deciding which model is superior. (25) For the present they merely serve as an indicator of the large value of $\omega_c\tau$ achieved in G3<110>.

Summary

In summary, the NFE model does not agree with the results of the magnetoresistance experiments because it does not yield open orbits near <111> and because it does yield them in the region between <100> and <111>. An NFE model with a radius swollen from $1.495(2\pi\hbar/a)$ to $1.552(2\pi\hbar/a)$ to give the experimental n_{111} in $AuAl_2$ provides an excellent fit to the magnetoresistance data on $AuAl_2$ for a sampling of fourteen field directions. An NFE model with a radius swollen from $1.495(2\pi\hbar/a)$ to $1.532(2\pi\hbar/a)$ to give the experimental n_{111} in $AuGa_2$ produces the experimental magnetoresistance of

$AuGa_2$ for most of the fourteen directions of the field which were sampled. Therefore our magnetoresistance results give strong support to our interpretation of the Hall data, i.e., there are hole orbits on an electron sheet for $\underline{B} \parallel \langle 111 \rangle$ and the open surfaces of $AuGa_2$ may be more NFE-like than those of $AuAl_2$.

6. Conclusions

Extensive galvanomagnetic measurements on the AuX_2 compounds have demonstrated the feasibility of obtaining rather detailed topological information on the Fermi surfaces of metallic compounds. In $AuGa_2$ we were able, for the first time, to consistently observe magnetoresistance ridges due to higher order open orbits, while in both $AuAl_2$ and $AuGa_2$ we were able to determine the angular extent of aperiodic open orbits.

Hall effect and magnetoresistance data in $AuAl_2$ and $AuGa_2$ cannot be explained by the NFE model. A modified NFE model which increases the number of fourth zone electrons better explains both galvanomagnetic and dHvA data.

High-field galvanomagnetic properties primarily consist of weighted velocity averages over the open surfaces. Thus we have presented evidence that the open surfaces of $AuGa_2$ may be more NFE-like than those of $AuAl_2$. This result is consistent with the OPW predictions of section 1. The evidence available indicates that the Fermi surface of $AuIn_2$ is similar to that of $AuGa_2$. Relativistic effects may play an important role in this case.

We have shown that our extension of a single-relaxation time theory applied to a NFE-like model of AuX_2 gives a fair approximation to the experimental magnetoresistance in the $\{100\}$ plane. Perhaps, more importantly, we have demonstrated that for one complicated Fermi surface, the

magnetoresistance falls into the same three categories we described for a combination of cylindrical and spherical Fermi surfaces.

LIST OF REFERENCES

LIST OF REFERENCES

1. E. Fawcett, Advan. Physics 13, 139 (1964).
2. D. J. Sellmyer and P. A. Schroeder, Phys. Letters 16, 100 (1965).
3. D. J. Sellmyer, Ph.D. thesis, Michigan State University (1965), unpublished.
4. J. Piper, J. Phys. Chem. Solids 27, 1907 (1966).
5. D. J. Sellmyer, J. Ahn, and J.-P. Jan, Phys. Rev. 161, 618 (1967).
6. J. T. Longo, P. A. Schroeder, and D. J. Sellmyer, Phys. Letters, 25A, 747 (1967).
7. W. G. Pfann, Zone Melting (John Wiley, Inc., 1958).
8. E. Fawcett, W. A. Reed, and R. R. Soden, Phys. Rev. 159, 533 (1967).
9. E. Fawcett and W. A. Reed, Phys. Rev. 134, A723 (1964).
10. A. S. Joseph and W. L. Gordon, Phys. Rev. 126, 489 (1962).
11. J. P. G. Shepherd and W. L. Gordon, Phys. Rev. (to be published).
12. A. C. Thorsen and T. G. Berlincourt, Nature, London, 192, 959 (1961).
13. J.-P. Jan, W. B. Pearson, Y. Saito, M. Springford, and I. M. Templeton, Phil. Mag., 12, 1271 (1965).
14. D. J. Sellmyer (to be published).
15. J. Ahn and D. J. Sellmyer, Bull. Amer. Phys. Soc., 13, 485 (1968).

16. C. Kittel, Quantum Theory of Solids (John Wiley and Sons, Inc., New York, 1963) pp. 249-266.

17. T. L. Loucks, Augmented Plane Wave Method (W. A. Benjamin, Inc., New York, 1967) p. 15.

18. M. Kohler, Ann. Physik 5, 99 (1949).

19. E. Justi and H. Scheffers, Metallwirtschaft 17, 1359 (1938).

20. I. M. Lifshitz, M. Ya Azbel', and M. I. Kaganov, Zh. Eksperim. i Teor. Fiz. 31, 63 (1956). [English transl: Soviet Phys. - JETP 4, 41 (1957)].

21. R. V. Coleman, A. J. Funes, J. S. Plaskett, and C. M. Tapp, Phys. Rev. 133, A521 (1964).

22. W. A. Harrison, Phys. Rev. 118, 1190 (1960).

23. I. M. Lifshitz and V. G. Peschanskii, Zh. Eksperim. i Teor. Fiz. 38, 188 (1960). [English transl: Soviet Phys. - JETP 11, 137 (1960)].

24. J. E. Kunzler and J. R. Klauder, Phil. Mag. 6, 1045 (1961).

25. J. R. Klauder, W. A. Reed, G. F. Brennert, and J. E. Kunzler, Phys. Rev. 141, 592 (1966).

26. M. E. Straumanis and K. S. Chopra, Zeitschrift fur Physikalische Chemie Neue Folge 42, p. 344 (1964).

27. D. J. Sellmyer, private communication.

28. D. J. Sellmyer, Rev. Sci. Instr. 38, 434 (1967).

29. A. J. Funes and R. V. Coleman, Phys. Rev. 131, 2084 (1963).

30. R. G. Chambers, The Fermi Surface (John Wiley, Inc., 1960) p.114.

31. E. I. Blount, Phys. Rev. 126, 1636 (1962).

32. L. M. Falicov and Paul R. Sievert, Phys. Rev., 138, A88 (1965).

33. I. M. Lifshitz and V. G. Peschanskii, Zh. Eksperim. i. Teor. Fiz. 35, 1251 (1958). [English transl.: Soviet Phys. - JETP 8, 875 (1959)].

34. J. R. Klauder and J. E. Kunzler, The Fermi Surface (John Wiley, Inc., 1960) p. 125.

APPENDIX A

APPENDIX A

The Harrison Construction Program

This program is conveniently divided into the following sections:

I. Read in

II. Calculations

- A. Rotation of lattice and zone boundaries
- B. Plotting of zone boundaries
- C. Plotting of Fermi circles

III. Subroutines

- A. Matrix multiplication
- B. Coordinate elimination

Definitions of important variables are:

1. ROT is the Euler angle rotation matrix.
2. THETA, PHI, and PSI are the Euler angles in radians as given by Goldstein.
3. X are the coordinates of the lattice points in momentum space. EX are the rotated latice points.
4. VARRAD are the radii of all the Fermi spheres at their intersection with the plane Z.
5. AB and ORD are the x, y values of points on the Fermi circles.
6. C and S are the values of the cosine and sine.
7. V gives the directions of the vectors perpendicular to the Bragg reflection planes and the distance of the plane from the origin. CE is the rotated version of V.

8. XT and YT are trial values for coordinates describing the line formed by the intersection of Z and the Bragg reflection plane. XX and YY are the acceptable values of XT and YT (those which are not outside plotter bounds)

9. The two intersecting planes may be written $\alpha x + \beta y + \gamma z = \delta$, $z = \epsilon$; $DE = \delta - \gamma\epsilon$.

10. VOLBRZ is the volume of the Brillouin zone in units $2\pi\hbar/a = 1$. VALENCE is the number of valence electrons per primitive cell.

11. SX and SY are scaling factors for the plotter. SX = .67 means that a line in the x direction of length 1.5 will be plotted with a length of 1".

12. NC counts the number of cross-sections plotted in the x direction. RNC is the distance the plotter pen moves back to x = 0 after a row of cross-sections has been completed.

13. NPLNS is the number of cuts parallel to B, i.e. the number of Z planes.

14. In CALL PLOT(Y,X,n,SY,SX), Y and X are the values to which the pen moves; if n=1, the pen is down; if n = 2, the pen is up.

Because the Harrison construction only requires a knowledge of the crystal structure and the number of electrons in the conduction band, it is easy to adjust this programmed version of it to other metals by appropriately changing X, V, VOLBRZ, and VALENCE. This has been done for a body centered tetragonal metal (white tin) and for the hexagonal metals (cadmium, magnesium, and zinc). An adap-

tion of this program by Professor Sellmyer's students at MIT has calculated the NFE model of $AuSb_2$.[15]

```
      PROGRAM ONEORN
      DIMENSION ROT(3,3), X(3,100), EX(3,100),VARRAD(100), Z(15)
      DIMENSION AB(100), ORD(100)
      DIMENSION THETA(10), THATA(10), PHI(10), PHY(10), PSI(10), PSY(10)
      DIMENSION C(100), S(100)
      DIMENSION CF(3,20), V(4,20), XT(25),YT(25), XX(25), YY(25)
      DIMENSION GAR(2), DE(20,3)
      INTEGER STEP, QUIT, SENT, GUARD, UB
      READ 1000, VOLBRZ, VALENCE
 1000 FORMAT (2F10.6)
      READ 600, SX, SY, NC
  600 FORMAT(2F10.3, I5)
      READ 637,GAR(1), GAR(2), NNN
  637 FORMAT(2F10.4, I5)
      L = 1
 2001 READ 2010, THATA(L), PHY(L), PSY(L), QUIT
 2010 FORMAT (3F10.5, I1)
      IF (QUIT .EQ. 1)  GO TO 2011
      L = L + 1
      GO TO 2001
 2011 NA = L - 1
      J = 1
 2999 READ 3000,   (X(I,J), I=1,3),  SENT
 3000 FORMAT (3F10.6, I1)
      IF (SENT .EQ. 1 )  GO TO 3001
      J = J + 1
      GO TO 2999
 3001 NLF = J - 1
      K = 1
  299 READ 300, (V(I,K), I = 1, 4), GUARD
  300 FORMAT(4F10.6, I1)
      IF (GUARD .EQ. 1) GO TO 301
      K = K + 1
      GO TO 299
  301 NPTS = K - 1
      CONV = 3.14159265 / 180.0
      READ  501, (C(I), I = 1,72)
  501 FORMAT(8F10.4)
      READ  502, (S(I), I = 1,72)
  502 FORMAT(8F10.4)
      RADIUS =  SQRT((.375/3.14159)*VOLBRZ*VALENCE)
      UB = 60*NA + 23
      CALL PLOT (UB, X, 3)
      DO 9000 L = 1, NA
      THETA(L) = CONV * THATA(L)
      PHI(L) = CONV * PHY(L)
      PSI(L) = CONV*PSY(L)
      AA = COS(PHI(L))
      BB = SIN(PHI(L))
      CC = COS(PSI(L))
      DD = SIN(PSI(L))
      EE = COS(THETA(L))
      FF = SIN(THETA(L))
      ROT(1,1) = CC*AA-EE*BB*DD
      ROT(1,2) = CC*BB+EE*AA*DD
      ROT(1,3) = DD*FF
```

```
      ROT(2,1) = -DD*AA-EE*BB*CC
      ROT(2,2) = -DD*BB+EE*AA*CC
      ROT(2,3) = CC*FF
      ROT(3,1) = FF*BB
      ROT(3,2) = -FF*AA
      ROT(3,3) = EE
C     ROTATE MAGNETIC FIELD TO THETA(L), PHI(L), PSI(L)
      CALL MTRXML(ROT,X,EX,NLP,3)
      CALL MTRXML (ROT, V, CE, NPTS,4)
C     PRINT THE THREE MATRICES AND THETA(L), PHI(L), PSI(L)
      PRINT 1010, VOLBRZ, VALENCE, RADIUS
 1010 FORMAT(1H1, 25X *THE HARRISON CONSTRUCTION* //// *VOLUME OF BR. ZO
     1NE = *, F10.6,5X* VALENCE =*,F10.6,/
     2          *RADIUS OF FERMI SURFACE = *, F10.6 //)
      PRINT 4000, THATA(L), PHY(L), PSY(L)
 4000 FORMAT(1H ,*THE ROTATION MATRIX CORRESPONDING TO THETA = *,
     1F8.3, *,* 2X *PHI =*,F8.3, *,* 2X *PSI =*, F8.3,* IS*/)
      PRINT 4010, ((ROT(I,J), J=1,3), I=1,3)
 4010 FORMAT(30X, 3F10.4)
      PRINT 4011
 4011 FORMAT (//35X * THE LATTICE POINTS ARE*
     1//10X *       X(1)       X(2)       X(3)*10X*       EX(1)       EX(2)
     2  EX(3)*/)
      PRINT 4030, ( J, (X(I,J), I=1,3), (EX(I,J), I=1,3), J = 1, NLP)
 4030 FORMAT(1H , I10, 3F10.4, 10X, 3F10.4)
 4040 PRINT 4050
 4050 FORMAT(//30X, *V*, 44X, *CE*/)
      PRINT 4060, (J, (V(I,J), I=1,4), (CE(I,J), I=1,3), J=1,NPTS)
 4060 FORMAT(1H, I10, 4F10.4, 10X, 3F10.4)
      NPLNS = 10.0 * EE + 1.0
      DO 4500 M = 1, NPLNS
      G = M - 1
 4500 Z(M) = G * 0.1
      CALL PLOT ( 0.0, 0.0, 0, SY, SX)
      CALL PLOT(11.0, -45.0, 2, SY, SX)
      CALL PLOT( 0.0, 0.0, 0, SY, SX)
      NCHECK = 1
      DO 5500 M = 1, NPLNS
      PRINT 5410, Z(M)
 5410 FORMAT(1H-2, *Z =*, F8.3)
B.
C     DRAW ZONE BOUNDARIES
      PRINT 105
  105 FORMAT(//10X *I      K          DE(I,K)      BIG       SMALL    NB*
     1          *     XX(NB)    NS     XX(NS)      XT(I)      YT(I)*)
      DO 200 I = 1, NPTS
      DO 200 K = 1, NNN
C     WE ABBREVIATE DE= D(K) - C * CONST.  WHERE D(K) = GAR(K) * D
      DE(I,K) = GAR(K) *V(4,I) - CE(3,I)*Z(M)
C     WE ARE SOLVING THE PAIR OF SIMULTANEOUS EQUATIONS
C     AX + BY + CZ = D,    Z = CONST.    THUS WE CONSIDER THE VARIOUS
C     POSSIBILITIES A=B=0, A=0,  B=0, A.NE. 0 AND B .NE. 0.
      IF (CE(1,I) .EQ. 0.0 .AND. CE(2,I) .EQ. 0.0) GO TO 200
      IF (CE(1,I) .EQ. 0.0) GO TO 150
      IF (CE(2,I) .EQ. 0.0) GO TO 140
      DO 130 J = 1, 11
      AJ = J
```

```
      XT(J) = -3.0 + AJ/2.0
  130 YT(J) = (DE(I,K) - CE(1,I)*XT(J)) / CE(2,I)
C     WE ELIMNATE UNACCEPTABLE VALUES OF Y AND DIMENSION A NEW
C     VARIABLE YY WHICH ONLY CONTAINS NN ACCEPTABLE VALUES
      CALL ELIMNATE(YT,XT,YY,XX,NN)
      IF (NN .GE. 2) GO TO 100
      DO 131 J = 1, 11
      AJ = J
      YT(J) = -3.0 + AJ/2.0
  131 XT(J) = (DE(I,K) -CE(2,I)*YT(J))/CE(1,I)
      CALL ELIMNATE(XT,YT,XX,YY,NN)
C     NO SENSE IN DRAWING A LINE IF THERE IS ONLY ONE ACCEPTABLE VALUE
      IF ( NN .LT. 2) GO TO 61
C     NOW WE FIND THE LARGEST YY AND THE SMALLEST YY AND DRAW A LINE
C     BETWEEN THEM
  100 BIG = YY(1)
      SMALL = YY(1)
      NB = 1
      NS = 1
      DO 69 KK=2,NN
      IF (YY(KK).GT. SMALL) GO TO 67
      SMALL = YY(KK)
      NS = KK
      GO TO 69
   67 IF (YY(KK).LT. BIG) GO TO 69
      BIG = YY(KK)
      NB = KK
   69 CONTINUE
      PRINT 70, I, K, DE(I,K), BIG, SMALL, NB, XX(NB), NS, XX(NS)
   70 FORMAT(6X, 2I5, 5X, 3F10.3, I5, F10.3, I5, F10.3)
      BIG = BIG + 5.5
      SMALL = SMALL + 5.5
      XX(NB) = XX(NB) + 5.5
      XX(NS) = XX(NS) + 5.5
      CALL PLOT (SMALL, XX(NS), 2, SY, SX)
      CALL PLOT (BIG, XX(NB), 1, SY, SX)
      GO TO 200
  140 XT(I) = DE(I,K) / CE(1,I)
      IF (XT(I) .LT. -3.0 .OR. XT(I) .GT. 3.0)  GO TO 200
      PRINT 141, I, K, DE(I,K), XT(I)
  141 FORMAT(6X, 2I5, 5X, F10.3, 50X, F10.3)
      XT(I) = XT(I) + 5.5
      CALL PLOT(2.5,XT(I), 2, SY, SX)
      CALL PLOT( 8.5, XT(I), 1, SY, SX)
      GO TO 200
  150 YT(I) = DE(I,K) / CE(2,I)
      IF (YT(I) .LT. -3.0 .OR. YT(I) .GT. 3.0) GO TO 200
      PRINT 151, I, K, DE(I,K), YT(I)
  151 FORMAT(6X, 2I5, 5X, F10.3, 60X, F10.3)
      YT(I) = YT(I) + 5.5
      CALL PLOT(YT(I),2.5, 2, SY, SX)
      CALL PLOT(YT(I),   8.5, 1, SY, SX)
      GO TO 200
   61 PRINT 62, I , K, DE(I,K), NN
   62 FORMAT(6X, 2I5, 5X, F10.3, 70X, I5)
  200 CONTINUE
```

```
C
C.  5000 DO 5400 J = 1, NLP
         ARG = RADIUS*RADIUS - (Z(M)-EX(3,J))**2
         IF (ARG - 0.0001) 5090,5090,5100
    5090 VARRAD(J) = 0.0
         GO TO 5400
    5100 VARRAD(J) = SQRTF(ARG)
C        WE WILL NOT PLOT CIRCLES IF THEY WOULD EXCEED THE PLOTTER BOUNDS
         CHECK1 = ABS(EX(1,J)) + VARRAD(J)
         IF (CHECK1 .LT. 5.5) GO TO 5389
    5380 PRINT 5381, J
    5381 FORMAT(1X, *CHECK1 FOR J =*,I3)
    5389 CHECK2 = EX(2,J) - VARRAD(J)
         IF (CHECK2 .GT. -5.5) GO TO 5110
    5390 PRINT 5391, J
    5391 FORMAT(1X, *CHECK2 FOR J =*,I3)
         GO TO 5400
    5110 IF (VARRAD(J) .GE. 1.00) STEP = 1
         IF (VARRAD(J) .GE. .50 .AND. VARRAD(J) .LT. 1.00)  STEP = 2
         IF (VARRAD(J) .LT. .50)  STEP = 3
         DO 5200 I = STEP,72,STEP
         AB(I) = EX(1,J) + VARRAD(J) * C(I) + 5.5
    5200 ORD(I) = EX(2,J) + VARRAD(J) * S(I) + 5.5
         CALL PLOT (ORD(72), AB(72), 2, SY,SX)
         DO 5210 I = STEP, 72, STEP
    5209 CALL PLOT (ORD(I), AB(I), 1, SY, SX)
    5210 CONTINUE
    5400 CONTINUE
         PRINT 5412
    5412 FORMAT(/ *VARRAD(J) ARE*)
         PRINT 5411, (VARRAD(J), J = 1, NLP)
    5411 FORMAT(1X, 10F10.3)
         NCHECK = NCHECK + 1
         IF (NCHECK .NE. NC) GO TO 5499
         CALL PLOT(11.0, -45.0, 2, SY, SX)
         CALL PLOT (0.0,  0.0, 0, SY, SX)
         NCHECK = 1
         GO TO 5500
    5499 CALL PLOT (0.0, 11.0, 2, SY, SX)
         CALL PLOT (0.0,0.0,0,SY,SX)
    5500 CONTINUE
    9000 CONTINUE
         CALL PLOT (11.0,-2.0,2,SY,SX)
         CALL PLOT (0.0,0.0,-1, SY,SX)
         END
C
```

A

B

FTN5,3A 02/20/67

III A.

```
      SUBROUTINE MTRXML(ROT,X,EX,NLP,L)
      DIMENSION ROT(3,3), X(L,NLP), EX(3,NLP)
      DO 3010 J = 1, NLP
      DO 3010 I = 1, 3
      EX (I,J) = 0.0
      DO 3010 K = 1, 3
 3010 EX(I,J) = EX(I,J) + ROT(I,K) * X(K,J)
      RETURN
      END
C
```

FTN5,3A 02/20/67

B.

```
      SUBROUTINE ELIMNATE(YT,XT,YY,XX,NN)
      DIMENSION YT(23), XT(23), YY(23), XX(23)
      JJ= 1
      DO 60 II = 1, 11
      IF (YT(II).GT. 3.0 .OR. YT(II).LT. -3.0) GO TO 50
      YY(JJ)= YT(II)
      XX(JJ)= XT(II)
      JJ = JJ + 1
   50 IF(II .EQ. 11) NN = JJ - 1
   60 CONTINUE
      RETURN
      END
```

A print-out of calculations made by this program for B in the {110} plane 10° from <100> is included below. The cross-section plotted would be a cut through Γ ($p_z = 0.0$).

```
                    THE HARRISON CONSTRUCTION

VOLUME OF BR. ZONE =    4.000000        VALENCE =  7.000000
RADIUS OF FERMI SURFACE =    1.495133

THE ROTATION MATRIX CORRESPONDING TO THETA =    10.000,  PHI =  45.000,  PSI =    0.000 IS

                          0.7071     0.7071     0.0000
                         -0.6964     0.6964     0.1736
                          0.1228    -0.1228     0.9848
```

		FX(1)	FX(2)	FX(3)
X(3)			0.0000

THE LATTICE POINTS ARE

	X(1)	X(2)	X(3)	EX(1)	EX(2)	EX(3)
1	0.0000	0.0000	0.0000	0.0000	0.0000	0.0000
2	2.0000	0.0000	0.0000	1.4142	-1.3927	0.2456
3	-2.0000	0.0000	0.0000	-1.4142	1.3927	-0.2456
4	0.0000	2.0000	0.0000	1.4142	1.3927	-0.2456
5	0.0000	-2.0000	0.0000	-1.4142	-1.3927	0.2456
6	0.0000	0.0000	2.0000	0.0000	0.3473	1.9696
7	0.0000	0.0000	-2.0000	0.0000	-0.3473	-1.9696
8	1.0000	1.0000	1.0000	1.4142	0.1736	0.9848
9	1.0000	1.0000	-1.0000	1.4142	-0.1736	-0.9848
10	1.0000	-1.0000	1.0000	0.0000	-1.2191	1.2304
11	1.0000	-1.0000	-1.0000	0.0000	-1.5664	-0.7392
12	-1.0000	1.0000	1.0000	-0.0000	1.5664	0.7392
13	-1.0000	1.0000	-1.0000	-0.0000	1.2191	-1.2304
14	-1.0000	-1.0000	1.0000	-1.4142	0.1736	0.9848
15	-1.0000	-1.0000	-1.0000	-1.4142	-0.1736	-0.9848
16	2.0000	2.0000	0.0000	2.8284	0.0000	-0.0000
17	2.0000	-2.0000	0.0000	0.0000	-2.7855	0.4912
18	-2.0000	2.0000	0.0000	-0.0000	2.7855	-0.4912
19	-2.0000	-2.0000	0.0000	-2.8284	-0.0000	0.0000
20	0.0000	2.0000	2.0000	1.4142	1.7400	1.7240
21	0.0000	2.0000	-2.0000	1.4142	1.0454	-2.2152
22	0.0000	-2.0000	2.0000	-1.4142	-1.0454	2.2152
23	0.0000	-2.0000	-2.0000	-1.4142	-1.7400	-1.7240
24	2.0000	0.0000	2.0000	1.4142	-1.0454	2.2152
25	2.0000	0.0000	-2.0000	1.4142	-1.7400	-1.7240
26	-2.0000	0.0000	2.0000	-1.4142	1.7400	1.7240
27	-2.0000	0.0000	-2.0000	-1.4142	1.0454	-2.2152
28	2.0000	2.0000	2.0000	2.8284	0.3473	1.9696
29	2.0000	2.0000	-2.0000	2.8284	-0.3473	-1.9696
30	2.0000	-2.0000	2.0000	0.0000	-2.4382	2.4608
31	2.0000	-2.0000	-2.0000	0.0000	-3.1328	-1.4785
32	-2.0000	2.0000	2.0000	-0.0000	3.1328	1.4785
33	-2.0000	2.0000	-2.0000	-0.0000	2.4382	-2.4608
34	-2.0000	-2.0000	2.0000	-2.8284	0.3473	1.9696
35	-2.0000	-2.0000	-2.0000	-2.8284	-0.3473	-1.9696
36	3.0000	1.0000	1.0000	2.8284	-1.2191	1.2304
37	3.0000	-1.0000	1.0000	1.4142	-2.6118	1.4760
38	3.0000	1.0000	-1.0000	2.8284	-1.5664	-0.7392
39	3.0000	-1.0000	-1.0000	1.4142	-2.9591	-0.4937
40	-3.0000	1.0000	1.0000	-1.4142	2.9591	0.4937
41	-3.0000	-1.0000	1.0000	-2.8284	1.5664	0.7392
42	-3.0000	1.0000	-1.0000	-1.4142	2.6118	-1.4760

43	-3.0000	-1.0000	-1.0000	-2.8284	1.2191	-1.2304
44	1.0000	3.0000	1.0000	2.8284	1.5664	0.7392
45	-1.0000	3.0000	1.0000	1.4142	2.9591	0.4937
46	1.0000	3.0000	-1.0000	2.8284	1.2191	-1.2304
47	-1.0000	3.0000	-1.0000	1.4142	2.6118	-1.4760
48	1.0000	-3.0000	1.0000	-1.4142	-2.6118	1.4760
49	-1.0000	-3.0000	1.0000	-2.8284	-1.2191	1.2304
50	1.0000	-3.0000	-1.0000	-1.4142	-2.9591	-0.4937
51	-1.0000	-3.0000	-1.0000	-2.8284	-1.5664	-0.7392
52	1.0000	1.0000	3.0000	1.4142	0.5209	2.9544
53	-1.0000	1.0000	3.0000	-0.0000	1.9137	2.7088
54	1.0000	-1.0000	3.0000	0.0000	-0.8718	3.2000
55	-1.0000	-1.0000	3.0000	-1.4142	0.5209	2.9544
56	1.0000	1.0000	-3.0000	1.4142	-0.5209	-2.9544
57	-1.0000	1.0000	-3.0000	-0.0000	0.8718	-3.2000
58	1.0000	-1.0000	-3.0000	0.0000	-1.9137	-2.7088
59	-1.0000	-1.0000	-3.0000	-1.4142	-0.5209	-2.9544

	V				CE		
1	0.0000	1.0000	0.0000	1.0000	0.7071	0.6964	-0.1228
2	0.0000	-1.0000	0.0000	1.0000	-0.7071	-0.6964	0.1228
3	1.0000	0.0000	0.0000	1.0000	0.7071	-0.6964	0.1228
4	-1.0000	0.0000	0.0000	1.0000	-0.7071	0.6964	-0.1228

Z = 0.000

I	K	DF(I,K)	BIG	SMALL	NB	XX(NB)	NS	XX(NS)	XT(I)	YT(I)
1	1	1.000	2.959	-1.103	1	-1.500	9	2.500		
2	1	1.000	1.103	-2.959	1	-2.500	9	1.500		
3	1	1.000	1.103	-2.959	9	2.500	1	-1.500		
4	1	1.000	2.959	-1.103	9	1.500	1	-2.500		

RRAD(J) ARE

1.495	1.475	1.475	1.475	1.475	0.000	0.000	1.125	1.125	0.849
1.300	1.300	0.849	1.125	1.125	1.495	1.412	1.412	1.495	0.000
0.000	0.000	0.000	0.000	0.000	0.000	0.000	0.000	0.000	0.000
0.223	0.223	0.000	0.000	0.000	0.849	0.239	1.300	1.411	1.411
1.300	0.239	0.849	1.300	1.411	0.849	0.239	0.239	0.849	1.411
1.300	0.000	0.000	0.000	0.000	0.000	0.000	0.000	0.000	

APPENDIX B

APPENDIX B

A Program to Calculate $\Delta\rho/\rho$ in $\{100\}$ for AuX_2

The terminology in the program is obvious, e.g., μ = MU, ρ_{xx} = ROXX, $\langle v_z \rangle_A$ = VZA, $dp_z(A)$ = DPZA, $\langle \mu v_x \langle v_x' \rangle^{\mu} \rangle_B$ = MUXXB, etc. Note that the factor 2 in equations 41 is hidden in the statements following statement 32.

```
      PROGRAM FOURBZ
      TYPE REAL MUVXA, MUOA, MUVXB, MUOB, MUVXC, MUOC, MUVXD1, MUOD1,
     1 MUVXD2, MUOD2, MUXXA, MUXXB, MUXXC, MUXXD1, MUXXD2, MUVXE, MUOE,
     1 MUXXE, MUVXH, MUOH, MUXXH
C
      PRINT 15
   15 FORMAT(1H1)
      DO 40 N = 1,45
      A = N
      PHI = A*3.14159/180.0
      S = SIN(PHI)
      C = COS(PHI)
      T = S/C
C
C     OPEN ORBITS
      VZA = .5*(3.0*C/S -S/C)
      DP = -2.0
      MUVXA = -1.0/( 8.0*C**2)
      VXVZA = S/(8.0*C**2)
      VXVYA = -1.0/(8.0*C)
      MUOA = 1.0/S + 2.0/(3.0*C)
      DPZA = S/2.0
      VZB = .5*((-3.0*S)/C + C/S)
      MUVXB = -(1.0/(12.0*C))*(1.0/(2.0*C) + 1.0/S)
      VXVZB = -1.0/(8.0*S)
      VXVYB = VXVYA
      MUOB =(2.0/3.0)*(2.0/C + .5/S)
      DPZB = DPZA
      VZC = (-2.0*S)/C
      MUVXC = 8.0*MUVXA
      VXVZC = 4.0*VXVZA
      VXVYC = 4.0*VXVYA
      MUOC = 8.0/(3.0*C)
      DPZC12 = DPZA
      DPZC3 = .5*(C-S)
      VZD1 = VZB
      MUVXD1 = -(5.0/(12.0*C))*(5.0/(2.0*C) + 1.0/S)
      VXVZD1 = 5.0*VXVZB
      VXVYD1 = 5.0*VXVYA
      MUOD1 = (2.0/3.0)*(4.0/C + .5/S)
      DPZD1 = DPZA
      VZD2 = VZB
      MUVXD2 =-(1.0/2.0)*(1.0/S + 2.0/(3.0*C))*(1.0/(4.0*S) + 1.0/(2.0
     1*C))
      VXVZD2 = (-.25/S)*(C/(2.0*S) + 1.0)
      VXVYD2 = -.25*(.5/S + 1.0/C)
      MUOD2 = ( 1.0/3.0)*(5.0/C + 2.0/S)
      DPZD2 = C/2.0 - S
      MUXXA = -1.0/(72.0*C**3)
      MUXXB = -1.0/(96.0*C**2)*(1.0/(3.0*C) + 1.0/S)
      MUXXC = -7.0/(18.0*C**3)
      MUXXD1 = -25.0/(96.0*C**2)*(5.0/(3.0*C) + 1.0/S)
      D2L = 1.0/(4.0*S) + 1.0/(2.0*C)
      MUXXD2 = -D2L**2*(2.0/3.0)*(D2L/3.0 + 1.0/(4.0*S))
      XMUXA = -MUXXA
      XMUXB = -MUXXB
```

```
      XMUXC = -MUXXC
      XMUXD1 = -MUXXD1
      XMUXD2 = -MUXXD2
C     CLOSED ORBITS
      VZE = 0.0
      MUVXE = -1.0/(3.0*C**2)
      VXVZE = S/(4.0*C**2)
      VXVYE = -1.0/(4.0*C)
      MUOE = 4.0/(3.0*C)
      DPZE = 0.5*(C - S)
      MUXXE = - 5.0/(72.0*C**3)
      XMUXE = - MUXXE
      VZH = 0.0
      MUVXH = 9.0*MUVXE
      VXVZH = -9.0*VXVZE
      VXVYH = - 9.0*VXVYE
      MUOH = 3.0*MUOE
      DPZH = 0.5*(C-3.0*S)
      MUXXH = 27.0*MUXXE
      XMUXH = - MUXXH
C
      IF (T .LT. .333) GO TO 20
      IF ( T .LT. .5 .AND. T .GT. .333) GO TO 21
      IF ( T .GT. .5)  GO TO 22
C
C     OPEN ORBITS
   20 YY = DP**2*( DPZA/MUOA + DPZB/MUOB + DPZC12/MUOC + DPZD1/MUOD1)
      ZZ = VZA**2*DPZA/MUOA + VZB**2*DPZB/MUOB + VZC**2*DPZC12/MUOC  +
     1VZD1**2*DPZD1/MUOD1
      YZ = DP*(VZA*DPZA/MUOA + VZB*DPZB/MUOB + VZC*DPZC12/MUOC +
     1VZD1*DPZD1/MUOD1)
      XY =-(DP*MUVXA/MUOA - VXVYA)*DPZA - (DP*MUVXB/MUOB -VXVYB)*DPZB  -
     1(DP*MUVXC/MUOC - VXVYC)*DPZC12 - (DP*MUVXD1/MUOD1 - VXVYD1)*DPZD1
      XZ =-(VZA*MUVXA/MUOA-VXVZA)*DPZA - (VZB*MUVXB/MUOB-VXVZB)*DPZB -
     1(VZC*MUVXC/MUOC-VXVZC)*DPZC12 - (VZD1*MUVXD1/MUOD1-VXVZD1)*DPZD1
      XX = (-MUVXA**2/MUOA - MUXXA + XMUXA )*DPZA
     1+ ( -MUVXB**2/MUOB - MUXXB + XMUXB)*DPZB
     1+ (-MUVXC**2/MUOC - MUXXC + XMUXC)*DPZC12
     1+ ( -MUVXD1**2/MUOD1 - MUXXD1 + XMUXD1 )*DPZD1
C     CLOSED ORBITS
      YYC = 0.0
      ZZC = (VZE**2/MUOE)*DPZE + (VZH**2/MUOH)*DPZH + .39 + .25
      YZC = 0.0
      XYC = VXVYE*DPZE + VXVYH*DPZH + .39 - .25
      XZC = -(VZE*MUVXE*DPZE)/MUOE  + VXVZE*DPZE
     1 -(VZH*MUVXH*DPZH)/MUOH + VXVZH*DPZH
      XXC = (-MUVXE**2/MUOE - MUXXE + XMUXE)*DPZE + .39 + .25
     1 +(-MUVXH**2/MUOH - MUXXH + XMUXH)*DPZH
      GO TO 29
C
C     OPEN ORBITS
   21 YY = DP**2*( DPZA/MUOA + DPZB/MUOB + DPZC12/MUOC + DPZD2/MUOD2)
      ZZ = VZA**2*DPZA/MUOA + VZB**2*DPZB/MUOB + VZC**2*DPZC12/MUOC  +
     1VZD2**2*DPZD2/MUOD2
      YZ = DP*(VZA*DPZA/MUOA + VZB*DPZB/MUOB + VZC*DPZC12/MUOC +
     1VZD2*DPZD2/MUOD2)
```

```
      XY =-(DP*MUVXA/MUOA - VXVYA)*DPZA - (DP*MUVXB/MUOB -VXVYB)*DPZB  -
     1(DP*MUVXC/MUOC - VXVYC)*DPZC12 - (DP*MUVXD2/MUOD2 - VXVYD2)*DPZD2
      XZ =-(VZA*MUVXA/MUOA-VXVZA)*DPZA - (VZB*MUVXB/MUOB-VXVZB)*DPZB -
     1(VZC*MUVXC/MUOC=VXVZC)*DPZC12 - (VZD2*MUVXD2/MUOD2-VXVZD2)*DPZD2
      XX = (-MUVXA**2/MUOA - MUXXA + XMUXA )*DPZA
     1+ ( -MUVXB**2/MUOB - MUXXB + XMUXB)*DPZB
     1+ (-MUVXC**2/MUOC - MUXXC + XMUXC)*DPZC12
     1+ ( -MUVXD2**2/MUOD2 - MUXXD2 + XMUXD2 )*DPZD2
C     CLOSED ORBITS
      YYC = 0.0
      ZZC = (VZE**2/MUOE)*DPZE + .39 + .25
      YZC = 0.0
      XYC = VXVYE*DPZE + .39 - .25
      XZC = -(VZE*MUVXE*DPZE)/MUOE  + VXVZE*DPZE
      XXC = (-MUVXE**2/MUOE - MUXXE + XMUXE)*DPZE + .39 + .25
      GO TO 29
C
C     OPEN ORBITS
   22 YY = DP**2*( DPZA/MUOA + DPZB/MUOB + DPZC3/MUOC)
      ZZ = VZA**2*DPZA/MUOA + VZB**2*DPZB/MUOB + VZC**2*DPZC3/MUOC
      YZ = DP*(VZA*DPZA/MUOA + VZB*DPZB/MUOB + VZC*DPZC3/MUOC)
      XY =-(DP*MUVXA/MUOA - VXVYA)*DPZA - (DP*MUVXB/MUOB -VXVYB)*DPZB  -
     1(DP*MUVXC/MUOC - VXVYC)*DPZC3
      XZ =-(VZA*MUVXA/MUOA-VXVZA)*DPZA - (VZB*MUVXB/MUOB-VXVZB)*DPZB -
     1(VZC*MUVXC/MUOC=VXVZC)*DPZC3
      XX = (-MUVXA**2/MUOA - MUXXA + XMUXA )*DPZA
     1+ ( -MUVXB**2/MUOB - MUXXB + XMUXB)*DPZB
     1+ (-MUVXC**2/MUOC - MUXXC + XMUXC)*DPZC3
C     CLOSED ORBITS
      YYC = 0.0
      ZZC = (VZE**2/MUOE)*DPZE + .39 + .25
      YZC = 0.0
      XYC = VXVYE*DPZE + .39 - .25
      XZC = -(VZE*MUVXE*DPZE)/MUOE  + VXVZE*DPZE
      XXC = (-MUVXE**2/MUOE - MUXXE + XMUXE)*DPZE + .39 + .25
      GO TO 29
C
   29 PRINT 30, N, YY, ZZ, YZ, XY, XZ, XX
   30 FORMAT(//, I10, 6F10.4)
      PRINT 31, YYC, ZZC, YZC, XYC,  XZC, XXC
   31 FORMAT(/11X, 6F10.4)
      YY = YY + YYC
      ZZ = ZZ + ZZC
      YZ = YZ + YZC
      XY = XY + XYC
      XZ = XZ + XZC
      XX = XX + XXC
      PRINT 32, YY, ZZ, YZ, XY, XZ, XX
   32 FORMAT(/11X, 6F10.4)
      YYZZ = 4.0*YY*ZZ
      ZYYZ = -YZ*YZ*4.0
      YYZZXX = YYZZ*XX*2.0
      ZYYZXX = ZYYZ*XX*2.0
      YZXYZX =-YZ*XY*XZ*8.0
      ZYXZYX = YZXYZX
      YYZXXZ = -YY*XZ*XZ*8.0
```

```
      ZZXYYX = -ZZ*XY*XY*8.0
C
      PRINT 38, YYZZ, ZYYZ, YYZZXX, ZYYZXX, YZXYZX, ZYXZYX, YYZXXZ,
     1ZZXYYX
   38 FORMAT(/11X, 8F10.4)
C
      ROXX = (YYZZ - ZYYZ) / (YYZZXX - ZYYZXX + YZXYZX + ZYXZYX -
     1YYZXXZ - ZZXYYX)
      PRINT 39, ROXX
   39 FORMAT(/11X, F10.4)
C
   40 CONTINUE
C
      END
```